Multiferroic Transitions and Low-Energy Excitations of Quantum Spin Systems

Shih-Wen Huang

Advisor: Professor Di-Jing Huang

August 16, 2010

Contents

6 Conclusion and Future work 134

List of Figures

Chapter 1

Introduction

Low-dimensional quantum spin systems display interesting ground state properties. Such novel phenomena arise from the interplay among charge, spin, orbital among lattice degrees of freedom. The dimensionality of those systems also play an important role for physical properties. In particular, fluctuations typically increase with the decrease of dimensionality and preclude phase ordering such that ordered phases existing in three dimensions may not occur in a lower dimensionality. Since the discovery of high-critical temperature superconductivity in cuprates, where the two-dimensional Cu-O plane plays an important role in the conductivity, the search of related transition metal oxides opened up a fascinating field of vanadates, manganites, nickelats, and etc. Many of them have been surprising by their unexpected physical properties; for example certain vanadates undergoes a metal-insulator transition with a change of electric conductivity by several orders of magnitude. Other cases include the high-T_c cuprate supercondoctors, which resist the prediction of BCS theory for the highest superconducting transition temperature

[1], the colorsal magnetoresistance manganese oxides [2] and Multifferoics [3, 4].

However the origin of many phenomena are still controversial and to understand the origin of many properties of TMOs becomes an important problem in solid state physics. The difficulty comes from lacking a complete theory without any approximations. The existence of several competing tendencies, causing these strongly correlated systems to show a rich phase diagram and nonlinear responses. Electron correlations arising from the many body effects are crucial in understanding the physical properties of these materials. The electron of a solid can be described by three attributes: charge (e^-), spin $(S = \pm\frac{1}{2})$ and orbital which is coupled to the lattice degrees of freedom. The orbital may be understood as the shape of the electron in question. The cooperation/competition among these degrees of freedom typically lead to giant responses to small external stimulations typically through the interplay between magnetism and electrical conductance [5]. This interplay has been a long-term research topic in condensed matter physics. The magnetoelectric effect, which represents the induced electric polarization and magnetization by applying a magnetic and electric field, respectively, is expected to have potential applications for the modern technology. In this thesis we focus on low-dimensional multiferroics that display cross-correlations between magnetic and electric properties. Studying the magneoelectric and multiferroic properties of frustrated (or low-dimensional) system is interesting, because the competition between the classical and quantum effect gives rise to fan-
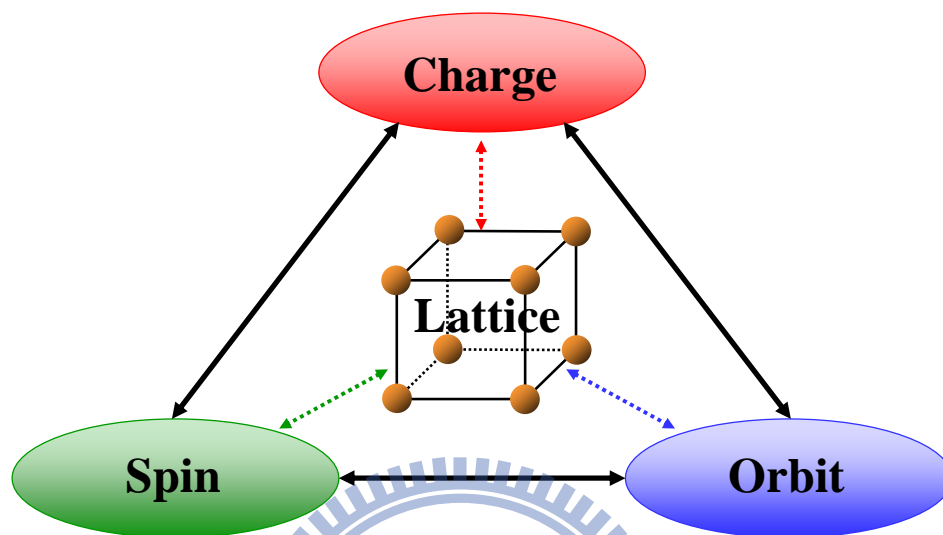
Figure 1.1: Schematic plot showing the interplay between charge, spin, orbital and lattice degrees of freedom in $3d$ transition metal oxides.

tastic phase transitions.

Outline of this thesis

This thesis contains six chapters. After a brief introduction of the rich variety of low-dimensional systems and transition metal compounds. We present introductional discussions on low-dimensional magneoelectric multiferroics.

Chapter 3, addresses our experimental techniques and related theories, e.g. interaction between x-ray and materials. In particular, the experimental setups, design, construction and commissioning will be described in details.

Following the description of the instrument, we will summarize our results on two samples. In Chapter 4, the electronic structures and magnetic

structures of quasi-one-dimensional quantum spin system $LiCu_2O_2$ are investigated by using soft x-ray techniques, namely soft x-ray absorption spectroscopy, resonant soft x-ray magnetic scattering and resonant inelastic soft x-ray scattering.

In Chapter 5, low-energy excitations in the quasi one-dimensional antiferromagnetism of CuO will be addressed. Additionally, the magnetic phase transitions are studied by temperature-dependent resonant soft x-ray magnetic scattering. Finally, we present the conclusion and an outlook of research related this thesis in Chapter 6.
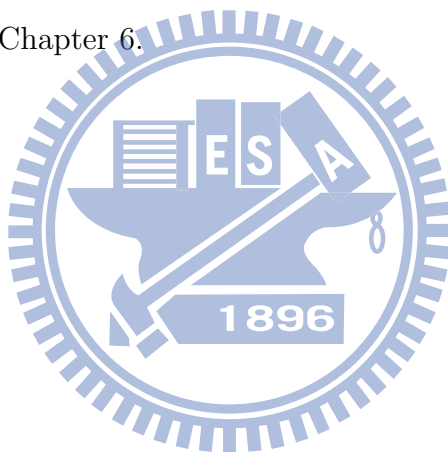
Reference

[1] J. G. Bednorz and K. A. Muller, Z. Phys. **64**, 189 (1986).

[2] S. Jin, T. H. Tiefel, M. McDormack, R. A. Fastnacht, R. Ramesh, and L. H. Chen, Sceince **264**, 413 (1994).

[3] T. Kimura, T. Goto, H.Shintani, K.Ishizaka, T. Arima, and Y. Tokura, Nature (London) **426**, 55 (2003).

[4] N. Hur, S. Park, P. A. Sharma, J.S. Ahn, S. Guha, and S.-W. Cheong, Nature (London) **429**, 392 (2004).

[5] Yoshinori Tokura, Physics Today, 50 July (2003).

Chapter 2

Low-Dimensional Systems and Magnetoelectric Multiferroicity

In this chapter we will introduce some origins of localized moments in magnets and the possible coupling between them. Then some concepts of low-dimensional quantum spin system followed by magnetoelectric and multiferroic materials are discussed as the reference to the systems covered in this thesis. In particular, we discuss some phenomenological theories, which could depict the induced of electric polarization in magnetic states.

2.1   Magnetic Ordering

In classical magnets long-range order is typically observed below the characteristic temperature T_c, where the thermal fluctuation is small enough. The simplest model of magnetic system is in terms of semi-classical descriptions in which quantum fluctuation is negligible.

The magnetic moment of an ion typically comes from an unfilled electronic shell [1]. In atomic physics the magnetic ground state is governed

6

by the Hund's rule, in which the ground state is to maximize the total spin $\vec{S}$, and total angular momentum $\vec{L}$, so that we can minimizes the Coulomb repulsion between electrons. The spin-obit coupling can be expressed as $\vec{J} = \vec{L} + \vec{S}$. However, the situation usually changes in real magnetic materials, due to the electric field creased by the surrounding ions. The ground state might differ from that given by the Hund's rules. Furthermore, in in some cases of $3d$ transition mental ions the orbital angular momentum might be quenched by the environments and the ground state become an orbital singlet.

In real materials, spins interact each other via the exchange interaction, depending on the structure and the composition of the crystal. Exchange interaction leads to long-range order and dispersion of the excitations in a spin system. There are two categories of couplings, weak coupling due to the magnetic dipolar interaction and strong coupling arising from interactions such as direct exchange, superexcahgne, double exchange and etc.

Direct exchange results from a direct overlap of neighboring magnetic orbitals. In general, the direct exchange between a pair of electrons is small compared with the electric interactions. Superexchange refers to the exchange interaction between magnetic ions through a non-magnetic ion. It describes the interaction between magnetic ions which are not nearest neighbors, and the interaction highly depends on geometry of magnetic and non-magnetic ions. Figure 2.1 illustrated the antiferromagnetic superexchange interaction in a linear M-O-M group. Goodenough [2] rules outline whether

the interaction between ions is likely to be antiferromagnetic or ferromagnetic. Double exchange occurs between mixed valency states and comes out electrons hopping between magnetic ions.
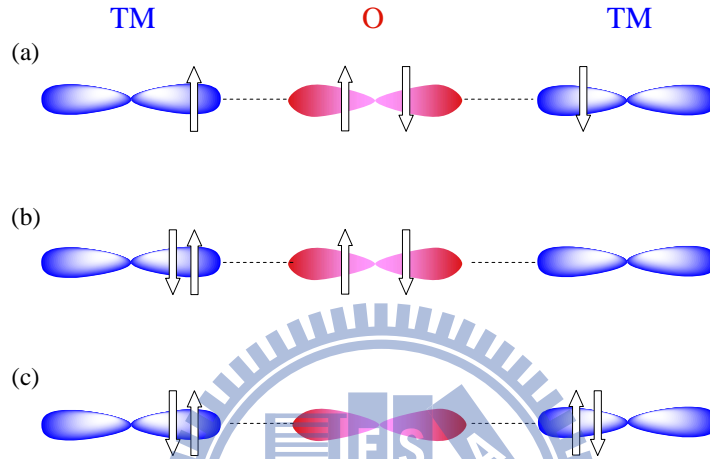
Figure 2.1: Illustrations of antiferromagnetic superexchange interaction in the linear TM-O-TM group. (a), (b), and (c) show the configurations of ground states and two excited states.

2.2 Low-Dimensional Quantum Spin System

The ground-state physical properties of low-dimensional frustrated spin system have attracted a lot of attention in decades. A rich phase diagram and novel magnetic properties, which originate from the interplay of geometrical frustration and quantum fluctuations in low dimensions, have been predicted theoretically and lots of interesting phenomena have been observed experimentally. However, there are no consensus theoretical and descriptions on the physical properties of such low dimension systems.

For quantum magnetism [3], the effects of quantum fluctuation must be

considered as well as the thermal fluctuation. A small quantum number, low dimensionality and frustration all enhance the quantum fluctuation which is a consequence of the ground-state quantum uncertainty. The challenge of quantum phase transitions in spin systems comes from the understanding of the transition between novel quantum and fractional spin excitations. A classical phase transition is driven by thermal fluctuations, and can be varied by changing the temperature of the system. A quantum phase transition is phase transition at zero temperature which strongly effected by the quantum fluctuation. The quantum fluctuations can be increased by slightly varying a control parameter in the Hamiltonian of the system, for example an applied field or the chemical concentration such that a new ground state can be reached. A quantum critical point is a point which the transition occurs at zero temperature. Although the observation of the phase transition of a system is not technically achievable at $T = 0$, it is possible to reach a temperature where quantum fluctuations are dominant.

Before presenting the detail results let us introduced some theories for low dimension magnet system. In 1931 Bethe proved that on long-range order exist in the one-dimensional $S = \frac{1}{2}$ quantum Heisenberg antiferromagnet (HAF) event at T = 0 [4]. Van Hove proved that there are no phase transition in a one-dimensional classical gas with hard-core and finite-range interactions in 1950 [5] and in 1964 Griffiths [6] proved that the Ising model is ferromagnetic in a system of dimension D > 1. Later in 1966/67 Mermin [7] and Wagner demonstrated that in an isotropic spin$-\frac{1}{2}$ Heisenberg model

which the effective exchange interaction are isotropic and of finite-range localized spins cannot have long-range order (LRO) in a system of dimension D <3 at any finite temperature because thermal fluctuation . In other words, there is no long range ordering exist in 2D at finite temperatures if the order parameter is continues. In a low-dimensional system, the long range magnetic ordering can survive at zero temperature only when quantum fluctuation are not too strong.

A quasi-one-dimensional system of spin-$\frac{1}{2}$ chain with interplay of geometric frustration and quantum fluctuation is interesting and important because of the competition between the nearest-neighbor and next nearest-neighbor interactions i.e., J_1 and J_2, respectively. In the classical regime, such a competition results in magnetic ground state of long-range incommensurate spiral spin with a propagation vectors $\cos^{-1}(J_1/4J_2)$, if $|J_1/J_2| < 1/4$ [8]. For quantum systems, quantum fluctuations can destroy the long-range order and give rise to gapped spin-liquid phase with commensurate spin correlations [9, 10, 11, 12, 13], and other exotic states depending upon $|J_1/J_2|$ [14]. In addition, 3D interactions in real quasi-1D materials tend to suppress quantum spin fluctuations and restore semiclassical behavior.

2.3 Frustration

In addition to low-dimensionality, frustration can also enhance quantum fluctuations. The basic concept of frustration can be simply introduced by the geometry frustration. In a spin system, geometry frustration is a phenom-

enon that arises when the antiferromagnetic bonds between a collection of spin degree of freedom that can not be optimized simultaneously. Consider an example illustrated in Fig. 2.2 (a) three classical spins are arrange in an equilateral triangle. If the bonds are all antiferromagnetic and equally strong, any pair of spins would individually minimize the energy in an antiferromagnetic configuration. However, the interaction energy of the remaining third particle can not be minimal simultaneously. The total energy will minimize by a different configuration; such a configuration is called "frustrated". Such concept is easily generalized to large or non-uniform systems. For instance, a square lattice of spins with nearest-neighbor coupling is not frustrated and the classical Nèel states satisfy all the couplings in the system. Frustration is introduced by an antiferromagnetic next-nearest-neighbor interaction, as shown in Fig 2.2 (b). Frustration may also occur in one-dimensional systems. In some cases the competitions between nearest-neighbor and next-nearest-neighbor spin give arise to the magnetic spiral ground state. In general in frustrated system it is not possible to satisfy all given constrains simultaneously, and the ground state (classical or quantum mechanical) is the best possible compromise. The effect of adding frustration to a low dimensional systems typically lowers the transition temperature of a long-range order and even removes the transition in same case.
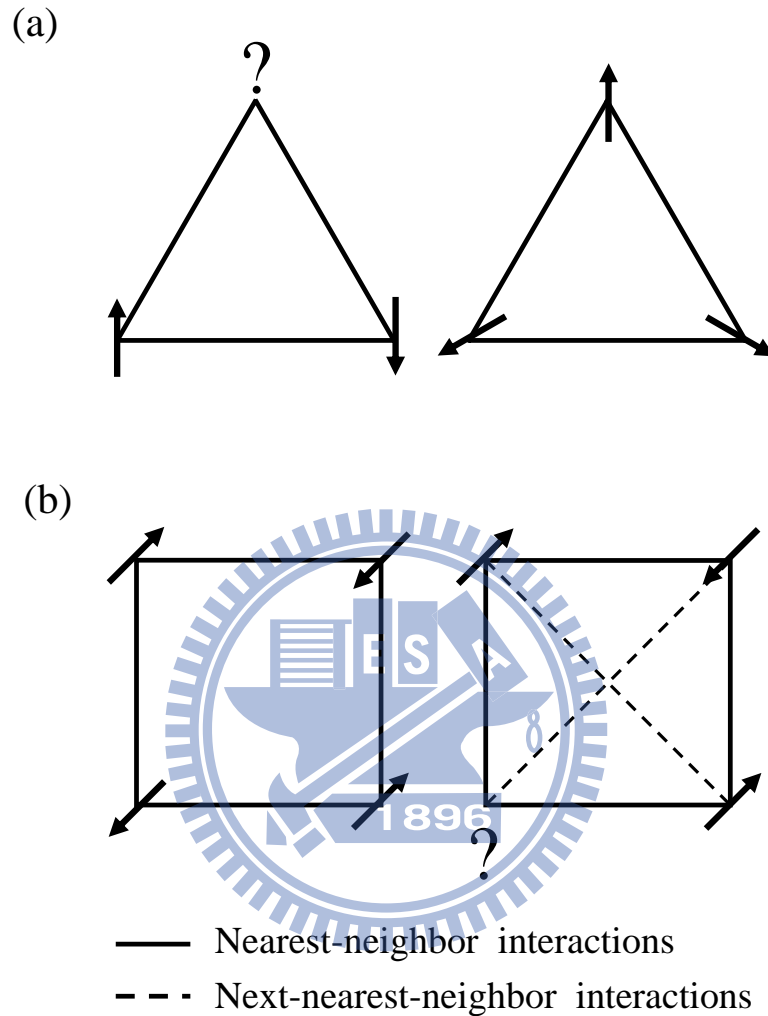
Figure 2.2: (a) Illustration of frustrations in a triangular lattice. Three spins, interacting pairwise and antiferromagnetically. An antiparallel configuration would minimize the energy of each bond, but can not be fullfiled for all three spins simultaneously. The total energy will be minimized with a different configuration— in the present case a spiral where any two spins from an angle of 120°. (b) A two dimensional square lattice with an AFM coupling. The couplings on such a lattice are frustrated when there is an antiferromagnetic next-nearest-neighbor interaction.

2.4   Magneto-electric Coupling

Electronic and magnetic materials form two important parts of modern technologies which demands the trend of a multifunction devices. According to

the original definition given by Schmid [15], multiferroics are materials that combine two or more of the primary forms of ferroic oreder, i.e. ferroelasticity, ferromagnetism, and ferrotoroidicity. Nowadays, most of the recent research has focused on materials in which ferroelectric and magnetism coexist are known as "magnetoelectric multiferroics". These materials have potential for the construction of novel spintronic devices such as tunnelling magnetoresistance (TMR) sensors, spin valves which is tunable by an electric field and so on [16]. However, in the application steps, the magnetoelectric coupling must be large and work at room temperature.

The coupling between magnetic and (ferro)electric order has long been considered as the magnetoelectric effect. The magnetoelectric (ME) effect was first postulated by the Pierre Curie in the nineteenth century [17]. A large magnetoelectric effect means the induction of magnetization by an electric field or change the electric polarization by a magnetic field. The existence or absence of the linear magnetoelectric effect can be recognized from the magnetic point group symmetry. Additionally, it is traditionally well described by the Landau theory. In the Landau expression, the free energy F describes the magnetoelectric effect of non-ferroic materials, in terms of an applied magnetic field $\vec{H}$ of which the ith component is denoted as $\vec{H}_i$, and an applied electric field $\vec{E}$ of which the ith component is denoted $\vec{E}_i$ as follows.

$$\vec{F}(\vec{E},\vec{H}) \;\; = \;\; F_0 + \frac{1}{2}\varepsilon_0\varepsilon_{ij}\vec{E}_i\vec{E}_j - \frac{1}{2}\chi_0\chi_{ij}\vec{H}_i\vec{H}_j - \alpha_{ij}\vec{E}_i\vec{H}_j -$$

$$\frac{1}{2}-\beta_{ij}\vec{E}_i\vec{H}_j\vec{H}_k - \frac{1}{2}\gamma_{ijk}\vec{H}_{ij}\vec{E}_i\vec{E}_k + ... \ . \tag{2.1}$$

Here, ε_0 and χ_0 are the permittivity and permeability of free space, ε_{ij} and χ_{ij} are the relative permittivity and permeability, α_{ij} is the linear magneto-electric tensor, and β_{ijk} and γ_{ijk} are higher-order magnetoelectric coefficient. The second term on the right hand side describes the contribution of an electric field. The third term is the magnetic equivalent part of the second term. The forth term describe the linear magnetoelectric coupling through α_{ij}. The derivative of free energy with respect to $\vec{E}_i$ or $\vec{H}_i$ gives the polarization, $\vec{P}_i$ or magnetization $\vec{M}_i$

$$\vec{P}_i = -\frac{\partial \vec{F}}{\partial \vec{E}_i} = \frac{1}{2}\varepsilon_0\varepsilon_{ij}\vec{E}_j + \alpha_{ij}\vec{H}_j + \frac{1}{2}\beta_{ijk}\vec{H}_j\vec{H}_k + ...$$

$$\vec{M}_i = -\frac{\partial \vec{F}}{\partial \vec{H}_i} = \frac{1}{2}\chi_0\chi_{ij}\vec{H}_j + \alpha_{ij}\vec{E}_i + \frac{1}{2}\gamma_{ijk}\vec{E}_i\vec{E}_j + ... \ . \tag{2.2}$$

It is worth noting that linear ME materials not always to be a multiferroic. For instance Cr_2O_3 is a magnetotlectric but not ferroelectric.Vice versa, not all multiferroics are necessarily magnetoelectrics, $YMnO_3$ is a multiferoic but no ME effect because the symmetry.

There is an interesting relation between magnetoelectric coupling and magnetic frustrations, which result from either competition between spin interactions or geometric constraints and lead to highly degenerated states. The results of frustration depend upon the types of materials. For instance, quantum spin $\frac{1}{2}$ systems may arise a spin liquid [18], whereas a spin ice has multiple degenerate disordered ground states [19]. On the other hand, if

spins are classical and reasonably isotropic, the competition will result in the inhomogeneous spin ordering that break inversion symmetry and time reversal symmetry. In addition, the large magnetic susceptibilities and the field-induced phase transition are commonly found in the frustrated magnets. For example, $TbMn_2O_5$ is a multiferroic materials, which also show a colossal magnetoelectric effect. And $HoMn_2O_5$ undergoes an incommensurate to commensurate magnetic phase transition, accompanied by the ferroelectric transitions. Most ferroelectricity(FE) often occurs in by transition metal (TM) oxides with pervoskite structure, in which transition ions have empty d shells. For a prototypical perovskite-structure ferroelectrics, the spontaneous polarization is due to collective shift of cations and anions inside the crystal and bulk electric polarization is induced. Such off-centering disorder can be stabilized by a covalent bonding (electronic pairing) between the oxygen $2p$ and the empty d shell of transition metals. In contrast, magnetism usually requires a transition metal with partially filled d shells [20, 21].

The other case for the FE is not due to TM ions but driven by the A-site ions, for example the Bi^{3+} in $BiTiO_3$ and Pb^{2+} in $PbTiO_3$ [20, 21]. In those materials the lone s electron pairs can lower their energy by hybridizing with empty p orbital. As FE is driven by this mechanism and the B-site cations are occupied by the magnetic ions, such as $BiFeO_3$ and $BiMnO_3$, ferroelectricity and magnetism can coexist in this system. However, the main driving force of the ferroelectricity of these materials and magnetism are associated with different ions; the coupling strength between them is usually weak. For

instance, $BiFeO_3$ shows a ferroelectric transition at a critical temperature $T_C \sim 1100$ K but the antiferromagnetic transition at $T_N \sim 643$ K. Although magnetization and electric polarization coexist at room temperature, the ferroelectric ordering temperature is much higher than that for magnetic ordering T_N. The origins of these orders have no relation to each other, leading to only weak coupling between magnetism and ferroelectricity. The ferroelectrics discussed above the polar state are driven by the structure deformation or the electron pairing are called "proper" ferroelectrics.

In the symmetry point of view, ferroelectrics and electric diploe moments change sign under the inversion operation $\mathbf{r} \rightarrow$ -$\mathbf{r}$, but remain invariant on the time reversal $\mathbf{t} \rightarrow$ -$\mathbf{t}$. On the contrary, it is opposite for magnetization $\vec{M}$ and magnetic field $\vec{H}$. Magnetic dipole moments are unaffected by the spatial reversal but reverses its sign by the time reversal. We can find out that the symmetry for ferroelectricity and magnetism makes these two order states mutually exclusive.

2.5 Multiferroics

It is difficult to discover new intrinsic multiferroic materials because the mechanisms of driving ferroelectricity and ferromagnetism are generally incompatible. Recently, various multiferroic materials have been discovered in materials of which the polar state is only a part of a complex lattice distortion or is induced by some other ordering [22, 23] those classes of ferrolectric called "improper ferroelectrcity". In those compounds the magnitude of

electric polarization and the temperature coexist ferroelectric and magnetic ordering are often small, but they exhibit a large ME coupling or sensitive to the external magnetic field. To our best knowledge the known improper ferroelectrics can be divided into three categories: geometric ferroelectrcs, electronic ferroelectrics and magnetic ferrolectrics [24].

In the geometric ferroelectrics, the driving force of ferroelectricity involves not only cooperative off-center shifts of transition metal ions but also a complex lattice distortion. For instance, the hexagonal $RMnO_3$ (R = rare earth) of which the ferroelectricity is caused by the rotation of rigid Mm-O polyhedra and bucking of the R-O plane. The ideal of electronic ferroelectrics can be generally correlated to the charge ordering (CO) [25, 26, 27]. Here we will introduce three types of charge ordering and then discus how the ferroelectricity is induced magnetism. One type of charge order pattern refers to the site-centered charge ordering (SCO) was illustrated in Fig. 2.3 (a). For example, half-doped $La_{0.5}Ca_{0.5}MnO_3$ is widely believed to have checkerboard type charge ordering and shows the site-centered charge ordering. Another type of charge-ordering is bond-centered charge ordering (BCO) which is often found in a dimer system or low-dimensional compounds. Such a lattice dimerization can be driven by the Peierls distortion. In this case the bonds are not equivalent i.e. strong and weak bonds alteratively. The first experimental observation of BCO is $Pr_{1-x}Ca_xMnO_3$ with x=0.4. [28]. It has been proposed that, in the low-temperature phase of this system two MnO_6 octahedral form pairs and elongate in the same direction compose a Mn-

Mn dimer. One extra electron sharing by the pair of neighboring Mn ions moving back and forth between them, with the double exchange mechanism. This dimer is called as a "Zener polaron". The proposed bond-centered CO structure of this case is depicted in the Fig. 2.3 (b). If one chooses charge order structure or the bond order structure as the mirror planes for SCO and BCO respectively, this process does not break inversion symmetry so that the resulting state can not be ferroelectric.
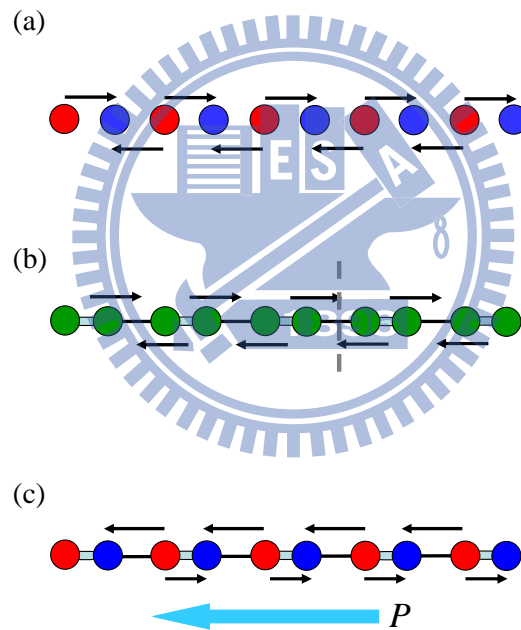
Figure 2.3: Three types of charge ordering. (a) Site-centered charge ordering (SCO) with red balls and blue balls denoted as different valence electrons. (b) Bond-centered charge ordering (BCO) with a gray dash line representing the mirror plane. (c) A linear combination of SCO and BCO state. The light blue arrow indicates a ferroelectric moment.

The situation however changes dramatically, if one combines both type of charge ordering in one system. Figure 2.3 (c) displays the circumstance

of coexisting the site- and bond-center CO. Obviously, this system isn't centrosymmetric and each pair of the cation and anion develop a net dipole moment, and thus the whole system becomes ferroelectrivity. In some materials, bonds are inequivalent because of the crystallographic structure, and below a certain temperature a spontaneous CO occurs and drives the inequivalence of the sites. Similarly, the material which have mixed valence, after the structure dimerization will induce FE. For example, Efremov et al., predicted that a certain divalent doped perovskites $R_{1-x}Ca_xMnO_3$ exhibit intermediate states with the coexistence of site-center charge ordering (SCO) and band-center charge ordering (BCO), leading to a new phenomenon – ferroelectricity [25]. Ferroelectricity induced by charge ordering has been also observed in a bilayer structure $LuFe_2O_4$. The average valence of Fe is 2.5+; below 350 K charge ordering creates Fe^{2+} and Fe^{3+} alternatively lie on the triangular lattice of the bilayer structure with ratios of 1:2 and 2:1. Charge transfer between layers give rises to the net polarization [29, 30]. Another example in this class includes the combination of charge ordering and the Ising chain magnet of the up-up-down-down ($\uparrow\uparrow\downarrow\downarrow$) spin structure. Ferroelectricity is induced by the exchange striction due to the competition between nearest-neighbor (NN) and next-nearest-neighbor (NNN) via the antiferromagnetic superexchange interaction. The broken of inversion symmetry is caused by the favor of a shorter interatomic distance between cation with parallel spins and longer distance between anion with anti-parallel spins. The polarization induced in the chain is schematically illustrated in the Fig. 2.4.
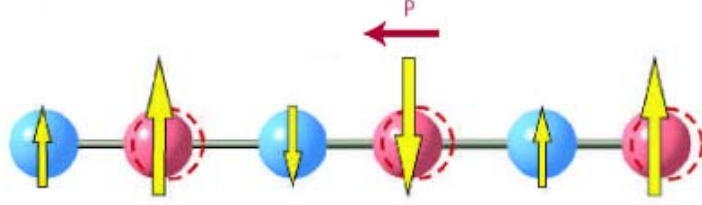
Figure 2.4: Polarization induced by coexisting site-centered charge and up-up-down-down spin orders in a chain with the nearest-neighbor ferromagnetic and next-nearest neighbor antiferromagnetic coupling. Cations are shifted away from the centrosymmetric position by exchange striction [29].

In 2003 Kimura *et al.*, discovered the induced ferroelectricity in TbMnO$_3$ by a spin-spiral structure on the Mn site [22]. In this new multiferroic compound, a large magnetoelectric effect has been observed at the onset of a metamagnetic transition, showing a magnetoelectric coupling. Recently theoretical studies successfully explain the mechanism of such induced ferroelectricity. The mechanism of magnetically induced ferroelectricity in spin-spiral structures have been studied using microscopic [31] and phenomenological approaches [32]. The phenomenological approach to magnetically induced ferroelectricity includes the symmetry of electrical and magnetic dipole moments. Based on the Ginzburg-Landau approach [33], the free energy F of a mutiferroic can be written

$$F = \frac{P^2}{2\chi_0} - \vec{E}_{\text{in}} \cdot \vec{P}. \tag{2.3}$$

$\vec{E}_{\text{in}}$ is an internal field which arises from the electron spin $\vec{S}$, and the cou-

pling between $\vec{P}$ and $\vec{S}_{\vec{q}}$ must be an odd order because the broken inversion symmetry, where $\vec{S}_{\vec{q}}$ being the magnetization at modulation vector $\vec{q}$. To minimize the free energy, we get $\vec{P} = \chi_0 \vec{E}_{\text{in}}$. From the symmetry point of view, under the time reversal transformation the magnetization changes sign $\mathbf{M} \to \mathbf{-M}$ but the electric polarization remains unchanged. Thus the lowest coupling is the coupling of $\vec{E}_{\text{in}}$ with $\vec{P}$. Furthermore, because $\vec{S}_{\vec{q}}$ changes sign under time reversal $\vec{E}_{\text{in}}$ must be quadratic in magnetization and contains at least two components in $\vec{S}_{\vec{q}}$. As a result, there are two possible combinations for $\vec{E}_{\text{in}}$: $\hat{u} \times (\vec{S}_{\vec{q}} \times \vec{S}_{-\vec{q}})$ or $(\vec{S}_{\vec{q}} \cdot \vec{S}_{-\vec{q}})\vec{q}$, where $\hat{u}$ is $\hat{a}, \hat{b}, \hat{c}$ or their linear combinations. Since $\vec{S}_{\vec{q}} \cdot \vec{S}_{-\vec{q}} = |\vec{S}_{\vec{q}}|^2$ is finite for any magnetic phase occurring below the Néel temperature T_N, which disagrees with the experimental results. Therefore we conclude that $\vec{E}_{\text{in}} = \sum_q i\gamma_{\vec{q}}\hat{u} \times (\vec{S}_{\vec{q}} \times \vec{S}_{-\vec{q}})$, $\vec{q}$ is the magnetic modulation unit vector $\gamma_{\vec{q}}$ is some unknown function to be determined by the microscopic models and $\vec{S}_{\vec{q}}$ is the fourier transform of magnetic structure, respectively. $\vec{S}_{\vec{q}} = \sum_n \vec{S}_n e^{i\vec{q}\cdot\hat{r}_n}$, with $\vec{S}_n$ and $\hat{r}_n$ being spin moments and position vectors respectively. According to the symmetry the induced polarization is determined by $\vec{S}_{\vec{q}} \times \vec{S}_{-\vec{q}}$. Furthermore, under the inversion symmetry operation $\hat{r} \to -\hat{r}$, the electric polarization $\vec{P}$ changes its sign, while the sign of $\vec{M}$ dose not.

If the magnetization has gradient terms then the trilinear coupling term $\vec{P}\vec{M}\partial\vec{M}$ is also allowed. This term can also induce polarization. Let us

consider the simplest case of a cubic system which has a free energy [32]

$$F = \frac{P^2}{2\chi_0} - \gamma \vec{P}[\vec{M}(\nabla \cdot \vec{M}) - (\vec{M} \cdot \nabla)\vec{M}]. \tag{2.4}$$

The same process as before, the induced polarization can than easily be found by differentiating F with respect to $\vec{P}$. One obtains:

$$\vec{P} = \gamma \chi_0 [(\vec{M} \cdot \nabla)\vec{M} - \vec{M}(\nabla \cdot \vec{M})]. \tag{2.5}$$

The spin-spiral structure can be described by

$$\vec{M} = M_1 \hat{e}_1 cos\vec{Q} \cdot x + M_2 \hat{e}_2 sin\vec{Q} \cdot x. \tag{2.6}$$

Here, $\hat{e}_1$ and $\hat{e}_2$ are the unit vectors that form an orthogonal basis and $\vec{Q}$ is the wave vector of the spiral. The spin rotation axis is $\hat{e}_3 = \hat{e}_1 \times \hat{e}_2$. Using Eq. (2.5) , the average induced polarization is orthogonal to both $\hat{e}_3$ and $\vec{Q}$

$$\vec{P} = \gamma \chi_0 M_1 M_2 (\hat{e}_3 \times \vec{Q}) \tag{2.7}$$

The magnetically induced polarization depends on the values of M_1 and M_2. If one of M_1 or M_2 is zero, the situation corresponds to a collinear. sinusoidal state, where the spins cannot induce polarization. Only when both M_1 and M_2 are non-zero, a non-collinear spiral state is formed that can induce polarization as the spin rotation axis is perpendicular to the wave vector [29, 32]. The most common system that $\vec{M}$ various as a function of space is spin frustrated system. These kind of magnetic materials contain several competitions through exchange interaction which causes spin frustration in the ground state. For example, in a one-dimensional Heisenberg

chain with erromagnetic nearest-neighbor exchange J_1 and antiferromagnetic next-nearest-neighbor exchange J_2, the ground configuration corresponds to a magnetic spiral state if $|\frac{J_1}{J_2}| < \frac{1}{4}$, the spiral spin density wave which breaks inversion symmetry and induces polarization.

In the microscopic mechanism, two scenarios can explain the magnetism induced ferroelectricity. One is the symmetric spin interaction $(\vec{S}_n \cdot \vec{S}_{n+1})$ which has been discussed in the charge-ordering induced ferroelectric's section. The other one is originally from superexchange interaction with a relativistic correction and its strength is proportional to the spin-orbit coupling. The so called the antisymmetric Dzyaloshinskii-Moriya (DM) interaction is one example [34].

Now we discuss the Dzyaloshinskii-Moriya interaction. In 1958, Igor' Ekhiel'evich Dzyaloshinskii attempted to explain the weak ferromagnetism in antiferromagnetic crystals, such as α-Fe_2O_3 [35]. He proposed that when there is no inversion symmetry between two magnetic ions in the crystals, there is a term governing the spin interaction that favors antiferromagneic spin arrangement with canted configurations. These canted spins lead to weak ferromagnetism in the antiferromagnetic crystals. In 1960 Tǒru Moriya [36] extended Dzyaloshinskii's phenomenology and developed a microscopic theory of this antisymmetric interaction with a use of superexchange formula proposed by P. W. Anderson in 1959 [37]. Mariya showed that the DM interaction is linearly proportional to the spin-orbit coupling. The DM interaction favors non-collinear spin ordering. In other words, the Dzyaloshinskii-Mariya

interaction resembles the form of antisymmetric superexchange interaction that appears in addition to the symmetric Heisenberg exchange $(\vec{S}_i \cdot \vec{S}_j)$ due to relativistic spin-orbit coupling. The DM interaction can be expressed as

$$\vec{D}_{n,n+1} \cdot \vec{S}_n \times \vec{S}_{n+1}, \tag{2.8}$$

where $\vec{D}_{n,n+1}$ is the Dzyaloshinskii vector and proportion to the $\vec{x} \times \hat{r}_{n,n+1}$, where $\hat{r}_{n,n+1}$ is the unit vector along the line connecting the magnetic ions n and $n + 1$; $\vec{x}$ is the shift of the oxygen ion (see Fig. 2.5). Thus the energy of DM interaction increase with $|\vec{x}|$ and is proportional to the spin-orbit coupling. Generally speaking, the DM interaction favors non-collinear spin ordering. which gives rise to weak ferromagnetism in antiferromagnetic layers of La_2CuO_4 and also transforms the collinear Nèel state in ferroelectric $BiFeO_3$ into a magnetic spiral.
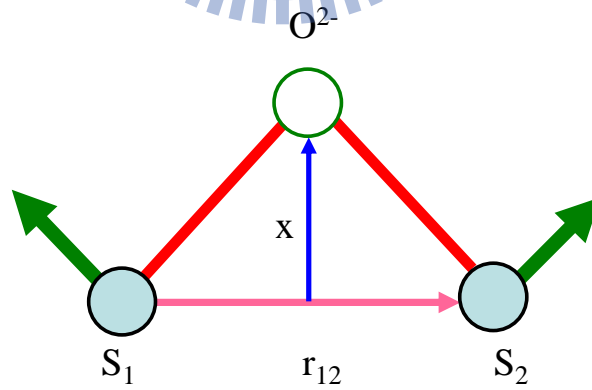
Figure 2.5: Effect of the Dsyaloshinskii-Moriya interaction.

Ferroelectricity induced by spiral magnetic ordering is the inverse ef-

fect of the DM interaction. To minimize the free energy, the interaction of canted spin can induced a displacement of oxygen ions located between transition-metal ions. For a spiral structure, if the vector product of any two neighboring magnetic moments $\vec{S}_n$ and $\vec{S}_{n+1}$ points to the same direction, the displacement of the oxygen ion is always in the same direction and perpendicular to the spin chain form by the positive magnetic ions. Through the overlap of the electronic wave function (the spin-exchange interaction) and the spin-orbit interaction, such system might yield electric polarization. The direction of polarization can be expressed with equation

$$\vec{P} = a \sum_n \hat{e}_{n,n+1} \times (\vec{S}_n \times \vec{S}_{n+1}), \qquad (2.9)$$

here $e_{n,n+1}$ is the unit vector connecting the neighboring magnetic moments at nth and $(n+1)$-th sites. As the exchange between two spins is reversed, the sign of the asymmetric DM interaction is also reversed $[(\vec{S}_n \times \vec{S}_{n+1} = -(\vec{S}_{n+1} \times \vec{S}_n)]$. Thus the induced electric polarization can be switched by the reversal of spin spiral model. This mechanism can also be expressed in terms of the spin-current which was proposed by Katsura *et* al., The spin current $\vec{j}_{n,n+1} \propto \vec{S}_n \times \vec{S}_{n+1}$, represents the precession of spin $\vec{S}_n$ in an exchange field created by spin $\vec{S}_{n+1}$. The induced electric diploe is then given by $\vec{P}_{n,n+1} \propto \vec{r}_{n,n+1} \times \vec{j}_{n,n+1}$. In the category of spiral-spin multiferroics, the spontaneous electric polarization can be controlled by an external magnetic field.

Then let us introduce spin structure which break inversion symmetry

(a)

M_{weak}

O^{-2} Cu^{2+}

(b)

P $e_3 \times Q$

O^{-2} Cu^{+2}

$\otimes \longrightarrow Q$
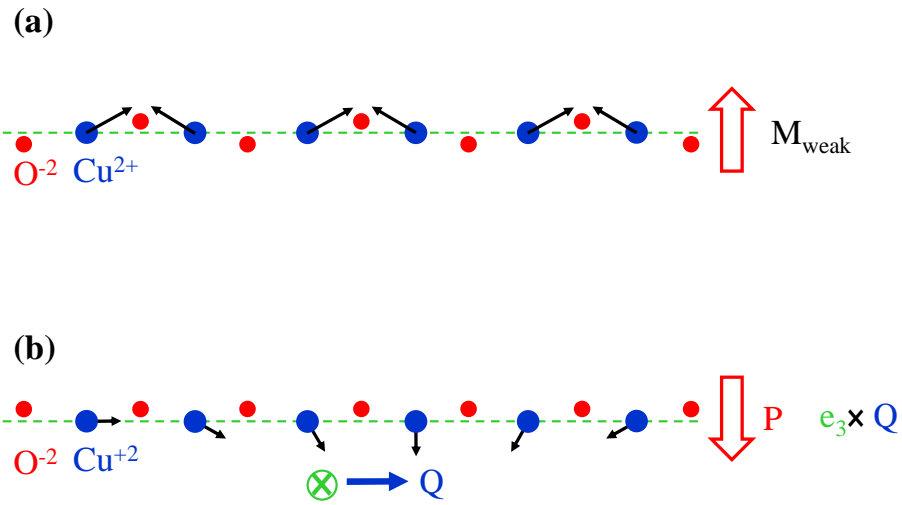
Figure 2.6: (a) The weak ferromagnetism in copper oxide layers of La_2CuO_4 arising from the Dzyaloshinskii-Moriya interaction. (b) The weak ferroelectricity resulting from the inver- Dzyaloshinskii-Moriya interaction where inhomogeneous magnetic order pushes the oxygen ions out of the plane.

and have potential cause a spontaneous polarization (ferroelectric) $\vec{P}$. This is valid both for collinear and noncollinear magnetic structures, when they are combined with a special lattice geometry. Figure 2.8 (a) depicts the collinear and 2.8 (b-e) several kinds of noncollinear spiral in one-dimensional arrays. For a collinear type of magnetostriction-induced ferroelectricity, the magnetic order is commensurate with the lattice structure.

There are several types of noncollinear spiral magnetic ordering. In a screw spiral structure, the axis of spin rotation is parallel to the propagation vector and there are two domains of handedness. One is left-handed the other is right-handed as shown in Fig. 2.8. These two structures can converted into each other by applying inversion operator, and usually do not coincide to each other. In other words, inversion symmetry is broken in screw spiral

(a)

Left-handed

$\longrightarrow$ q

(b)

Right-handed
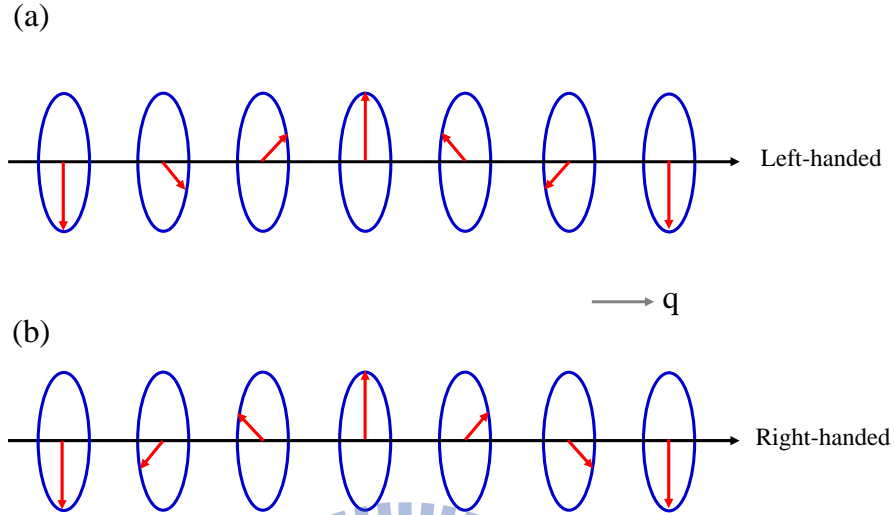
Figure 2.7: Two domains of a screw spiral structure.

magnets; however, time reversal jointed with half-period translation along the propagation vector is a symmetry operator of screw spiral. Because only inversion symmetry broken is not enough to make the system becomes polar, a screw structure system will not gives rise to the first order magnetoelectric effect ($\vec{P}_i = \sum_i \alpha_{ij} \vec{H}_i$) in the absence of external magnetic field.

Spins of a transverse-spiral with the rotation axis perpendicular to the propagation vector will result a cycloidal spiral structure. In a cycloidal spin order, according to the inverse DM interaction, the spontaneous polarization can be controlled by applying an external magnetic field. $TbMnO_3$ is a good example of this case, where ferroelectric ordering exists only in the cycloidal spiral phase. Spontaneous polarization emerges along the c axis, and is orthogonal to both the spin rotation (a axis) axis and the propagation
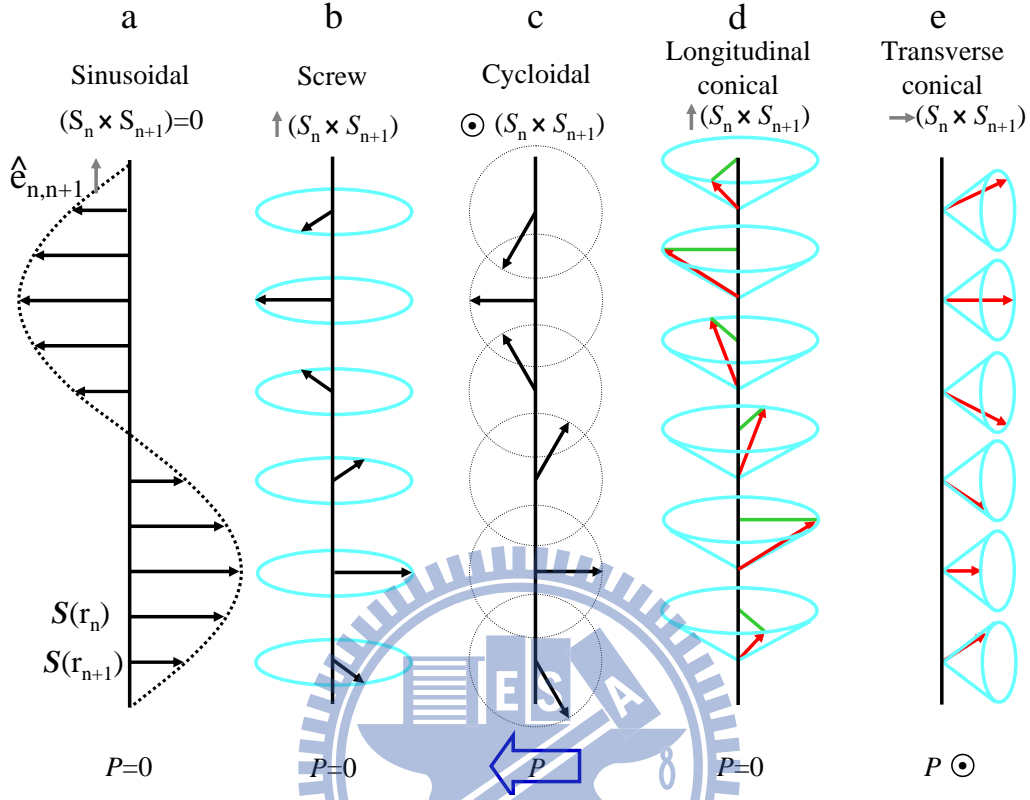
Figure 2.8: Schematic illustrations of different 1D magnetic structures. (a) Sinusoidal, (b) screw, (c) cycloidal, (e) longitudinal-conical, and (f) transverse-conical magnetic structure, where $\hat{e}_{n,n+1}$ indicates the unit vector connecting the neighboring magnetic moment. The vector of spin chirality and the magnitude of electric polarization calculated from the inverse DM interaction are also shown for their respective structure.

vector (b axis). By applying a weak magnetic field to the screw or cycloidal spiral structure the magnetic structure become conical. According to the inverse DM interaction, the transverse-conical system can give rise to the macroscopic polarization along the direction parallel to the cycloidal plane or perpendicular to the q-vector. Based on the inverse DM interaction, the longitudinal conical spin structure cannot produce the microscope electric polarization. If the applied external magnetic field is along the slanted direction of the screw axis (q-vector), the canted-conical spin state can give rise

to $\vec{P}$ perpendicular to both magnetic $\vec{q}$-vector and the cone axis.

Another mechanism is the ferroelectricity driven by so-called the E-type magnetic ordering, supported by *ab initial* calculations on a orthorhombic magnet such as $HoMnO_3$. This mechanism is rather similar to the ferroelectric due to charger ordering. In this compound, the oxygens are shifted away the center of TM-TM bonds, due to the $GdFeO_3$ type distortion, and the spin configuration is up-up-down-down along the [110] and [101] directions. In this spin configuration, the NN ferromagnetic interaction tends to move cations apart from each other; in contrast the NNN antiferromagnetic interaction tends to move Mn cations closer to one another. This movement breaks inversion symmetry which results in a net electrical polarization. The polarization induced by this mechanism is predicted to be much larger than that of any other improper ferroelectrics with spiral phases which have been studied so far. However, polarization measurements have been only performed on polycrystal samples of $HoMnO_3$, and the value is smaller by two or three orders of magnitudes than estimate *ab initio* calculations.

We have discussed several types of mechanism for multiferroic materials. However, it is hard to classify different types of multiferroics. One can divide multiferroics into two major categories. In type-I multiferroics, ferroelectricity (FE) is driven by hybridization and covalency or other purely structure effects. In other words, the two properties are due to different active "subsystem" of a material. In type-II multiferroics, ferroelectric is driven by some other electronic mechanism, e.g. "correlation" effects. Usually ferroelec-

tricity occurs at the same temperature scale of magnetic ordering or charge ordering; it can be regarded as a secondary effect of some other orderings.
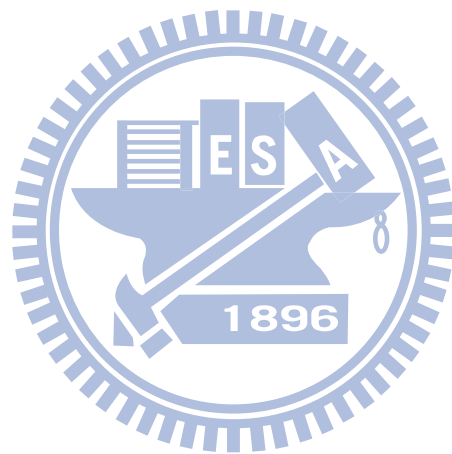
Reference

[1] P. W. Anderson, *Magnetism* vol. 1, Academic Press, New York (1963).

[2] B. J. Goodenough, *Magnetism and the Chemical Bond.* Interscience-Wiley, New York (1963).

[3] S. Sachdev, *Quantum Phase Transitions*, Cambride University Press (1999).

[4] H. A. Bethe, Z. Phys. **71**, 205 (1931).

[5] L. Van Hove, physica **16**, 137 (1950).

[6] R. B. Griffiths, Phys. Rev. **136**, A437 (1964).

[7] N. D. Mermin and H. Wagner, Phys. Rev. Lett. **17**, 1133 (1966).

[8] R. Bursill, G. A. Gehring, D. J. J. Farnell, J. B. Parkioson, T. Xiang, and Chen Zeng, J. Phys. Condens. Matter, **7** 8605(1995).

[9] B. S. Shastry, B. Sutherland, Phys. Rev. Lett. **47**, 964 (1981).

[10] F. D. M. Haldane, Phys. Rev. **23**, 04925 (1982).

[11] K. Okamoto, K. Kimura, Phys. Lett. A **179**, 433 (1992).

[12] S. R. White, I. Affleck, Phys .Rev. B **54**, 9862 (1996).

[13] A. A. Aligia, C. D. Batista, F. H. L.Essler, Phys. Rev. B **62**, 3259 (2000).

[14] S. Zvyagin, G. Cao, Y. Xin, S. Macall, T. Caldwell,W. Moulton, L-C. Brunel, A. Angerhofer, J. E. Crow, Phys. Rev. B **66**, 064424 (2002).

[15] H. Schmid, Ferroelectrics **162**, 317 (1994).

[16] W. Eerenstein, N. D. Mathur, and J. F. Scott, Nature **442**, 759 (2006).

[17] P. Curie, J. Phys. **3**, (Sec. III). 393-415 (1984).

[18] P. W. Anderson, Science **235**, 1196 (1987).

[19] A. P. Ramirez, A. Hayashi, R. J. Cava, R. Siddharthan, and B. S. Shastry, Nature **399**, 333 (1999).

[20] N. A. Hill, J. Phys. Chem. B **104**, 6694 (2000).

[21] N. A. Hill and A. Filippetti, J. Magn. Magn. Mater. **242**, 976 (2002).

[22] T. Kimura, T. Goto, H.Shintani, K.Ishizaka, T. Arima, and Y. Tokura, Nature (London) **426**, 55 (2003).

[23] N. Hur, S. Park, P. A. Sharma, J.S. Ahn, S. Guha, and S.-W. Cheong, Nature (London) **429**, 392 (2004).

[24] D. I. Khomskii, J. Magn. Magn. Mater. **306**, 1 (2006).

[25] Dmitry V. Efremov, Jeroen van den Brink, and D. I. Khomskii, Nat. Meter. **3**, 853 (2004).

[26] J. van den Brink and D. I. Khomskii, J. Phys.: Condens. Matter **20**, 434217 (2008).

[27] S. Picozzi, K. Yamauchi, I. A. Sergienko, C. Swn, B. Sanyal, and E. Dagotto, J. Phys.: Condens. Matter **20**, 434217 (2008).

[28] A. Daoud-Aladine, J. Rodríguez-Carvajal, L.Pinsard-Gaudart, M. T. Fernàndez-Díaz and A. Revcolevschi, Phys. Rev Lett. **89**, 097205 (2002)

[29] S.-W. Cheong and M. Mostovoy, Nat. Mater. **6**, 23 (2007).

[30] N. Ikeda, H. Ohsumi, K. Ohwada, K. Ishii, T. Inami, K. Kakurai, Y. Murakami, K. Yoshii, S. Mori, Y. Horibe, and J. Kito, Nature **436**, 1136 (2005).

[31] H. Katsura, N. Nagaosa, and A. V. Balatsky, Phys. Rev. Lett. **95**, 57205 (2005).

[32] M. Mostovoy, Phys. Rev. Lett. **96**, 067601 (2006).

[33] L. D. Landau and E. M. Lifshitz, *Electrodynamics of continuous media*, Pergamon, Oxford (1960)

[34] I. A. Sergienko and E. Dagotto, Phys. Rev. B **73**, 094434 (2006).

[35] I. Dzyaloshinsky, J. Phys. Chem. Solids **4**, 241 (1958).

[36] T. Moriya, Phys. Rev. **120**, 91 (1960).

[37] P. W. Anderson, Phys. Rev. Lett. **3**, 325 (1959).
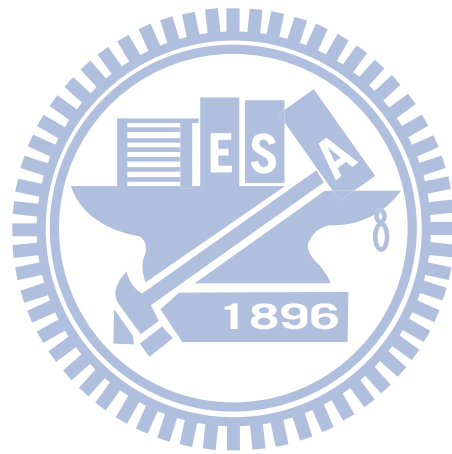
Chapter 3

X-ray Spectroscopic Techniques

Spectroscopies which are defined as the study of the interaction between light and matter are experimental techniques widely used to investigate the physical and chemical properties of materials.

3.1 Interaction between X-rays and Matters

The interaction Hamiltonian of a particle with charge q and mass m in an electrostatic potential V can be expressed as [1]

$$H_p = \frac{\mathbf{p}^2}{2m} + qV \tag{3.1}$$

In non-relativistic quantum mechanics if the particle interacts with the electromagnetic field, the interaction Hamiltonian can be written as [1]

$$H = \frac{1}{2m}[\mathbf{p} - q\mathbf{A}]^2 + qV - \frac{q\hbar}{2m}\mathbf{s} \cdot \mathbf{B} + H_R. \tag{3.2}$$

The first term is the kinetic energy of the particle in the presence of the electromagnetic field. The second term represents the external potential. The third term describe the interaction between electron spin of the particle and

magnetic filed. The last term is the Hamiltonian of quantized electromagnetic field; $\mathbf{A}$ is the vector potential the field [1]

$$\mathbf{A} = \sum_{\mathbf{k},\hat{\epsilon}} \sqrt{\frac{\hbar}{2\omega_{\mathbf{k}}\epsilon\nu}} [a_{\mathbf{k},\hat{\epsilon}} e^{-i\mathbf{k}\cdot\mathbf{r}}\hat{\epsilon} + a_{\mathbf{k},\hat{\epsilon}}^{\dagger} e^{i\mathbf{k}\cdot\mathbf{r}}\hat{\epsilon}^{*}] \tag{3.3}$$

where $a_{\mathbf{k},\hat{\epsilon}}$ and $a_{\mathbf{k},\hat{\epsilon}}^{\dagger}$ are annihilation and creation operators, which decrease and increase one photon, respectively. $\mathbf{k}$ and $\hat{\epsilon}$ are the wave vectors and polarization vectors. ω gives the photon frequency and ν is the normalization volume. In the atomic case, Eq. (3.42) will therefore sum over these electrons, plus a Coulomb term that describes the interaction between the electrons which will be included in H_P [2]. H_R in the excitation field can be expressed as

$$H_R = \sum_{\mathbf{k},\hat{\epsilon}} \hbar\omega_{\mathbf{k}}[a_{\mathbf{k},\hat{\epsilon}} a_{\mathbf{k},\hat{\epsilon}}^{\dagger} + \frac{1}{2}], \tag{3.4}$$

when the vector potential chosen to satisfy the Coulomb gauge ($\nabla \cdot \mathbf{A} = 0$). The Hamiltonian H of the system can be expressed

$$H = H_p + H_R + H_{int}, \tag{3.5}$$

where H_{int} is the interaction Hamiltonian.

$$H_{int} = -\frac{q}{m}\mathbf{p} \cdot \mathbf{A} + \frac{q^2}{2m}\mathbf{A^2} - \frac{q\hbar}{2m}\mathbf{s} \cdot \mathbf{B}. \tag{3.6}$$

If the ratio v/c is not completely negligible, where v is the speed of the particle and c is the speed of light, then an important term in the order of $(v/c)^2$ will arise. This term is called the spin-orbit term, which have two

components. The new Hamiltonian is

$$H = \frac{1}{2m}[\mathbf{p} - q\mathbf{A}]^2 + qV - \frac{e\hbar}{2m}\mathbf{s} \cdot \nabla \times \mathbf{A} - \frac{e\hbar}{2m^2}\mathbf{s} \cdot \mathbf{E} \times ([\mathbf{p} - q\mathbf{A}]) + H_R. \quad (3.7)$$

The spin-orbit term are responsible for magnetic scattering which we will discuss in section 3.3.1..

For simplicity let us restrict the discussion here to the case of a single electron and drop the magnetic terms. The leading contributions are

$$H_{int} = -\frac{e}{m}\mathbf{p} \cdot \mathbf{A} + \frac{e^2}{2m}\mathbf{A^2}. \quad (3.8)$$

We can treat H_{int} as a perturbation to the Hamiltonian $H_P + H_R$. From the standard perturbation theory, the solution of the total Hamiltonian H can be expressed in terms of the eigenfunctions $|\phi\rangle$ of the unperturbed Hamiltonian $H_0 = H_P + H_R$
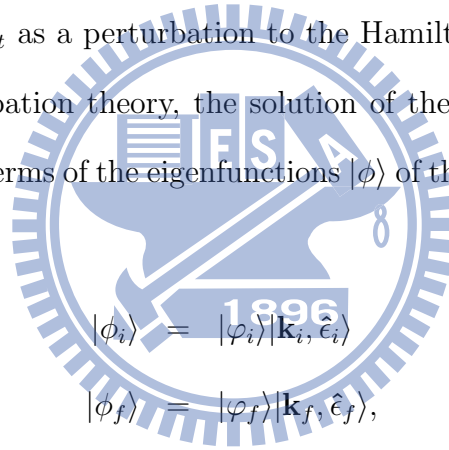
$$
\begin{aligned}
|\phi_i\rangle &= |\varphi_i\rangle|\mathbf{k}_i, \hat{\epsilon}_i\rangle \\
|\phi_f\rangle &= |\varphi_f\rangle|\mathbf{k}_f, \hat{\epsilon}_f\rangle,
\end{aligned} \quad (3.9)
$$

i and f indicate the initial and the final state, respectivly. The first term is the eigenstate of one particle Hamiltonian H_P and the second term is a photon state, eigenstate of H_R. The eigenvalues of unperturbed Hamiltonian H_0 can expressed as

$$H_0|\phi_i\rangle = E_i|\phi_i\rangle \quad \text{with} \quad E_i = \varepsilon_i + \hbar\omega_{\mathbf{k}_i}$$

$$H_0|\phi_f\rangle = E_f|\phi_f\rangle \quad \text{with} \quad E_f = \varepsilon_f + \hbar\omega_{\mathbf{k}_f}, \quad (3.10)$$

ε and $\hbar\omega_{\mathbf{k}}$ are the eigenvalues associated with $|\varphi_i\rangle$ and $|\mathbf{k}_i, \hat{\epsilon}_{\mathbf{k}}\rangle$ for the corresponding Hamiltonian. What we are interested in is the transition probability

per unit time form $|\phi_i\rangle$ state to $|\phi_f\rangle$ state under the effect of the perturbation

H_I. The expecting value is as following

$$W_{i \to f} = \frac{2\pi}{\hbar} |\langle \phi_f | T_I | \phi_i \rangle|^2 \rho_f, \qquad (3.11)$$

where ρ_f is the density of final state and T_I is the transition operator cor-

responding to the interaction Hamiltonian. The relation between T_I and H_I

are

$$T_I = H_I + H_I G(E_i) H_I. \qquad (3.12)$$

Here the $G(E_i)$ is the resolvent of total Hamiltonian H, which is defined by

$$G(E_i) = \lim_{\epsilon \to 0^+} \frac{1}{E_i - H + i\epsilon}. \qquad (3.13)$$

If $G(E_i)$ acts on any eigenstate $|\psi_n\rangle$ of H, one will have

$$G(E_i)|\psi_n\rangle = \frac{|\psi_n\rangle}{E_i - E_n}. \qquad (3.14)$$

Let we replace H_I by expression Eq. (3.8) to the second order in e/m

$$T_I^{(2)} = -\frac{e}{m}\mathbf{p} \cdot \mathbf{A} + (\frac{e}{m})^2[\frac{m}{2}\mathbf{A} \cdot \mathbf{A} + \mathbf{p} \cdot \mathbf{A} G(E_i)\mathbf{p} \cdot \mathbf{A}] + O(\frac{e}{m})^3. \quad (3.15)$$

X-ray spectroscopic techniques are divided into two categories [2, 3]; one

is linear to the $\mathbf{A}$ and can described by an one-step process, i.e., photoemis-

sion spectroscopy (PES) [4] and x-ray absorption spectroscopy (XAS) [5, 6].

The other is from a $\mathbf{A} \cdot \mathbf{A}$ term, responsible for x-ray scattering. Example

of two-step spectroscopies are Auger electron emission, x-ray emission spec-

troscopy and x-ray scattering. The first order process also contributes to the

scattering of x-rays with matter in the second order perturbation.

3.2   X-ray Absorption and Emission

3.2.1   Photoemission Spectroscopy

The one-step or first order optical process referring that first order perturbation theory of the electron-photon interaction is a suitable approach to describe photoemission. From the expression Eq. (3.3) of the quantized vector potential $\mathbf{A}$, the transition operators of photoemission can be expressed as [2]

$$T_{I,ab} = (\frac{e}{m}) \sum_{\mathbf{k},\hat{\epsilon}} \sqrt{\frac{\hbar}{2\omega_{\mathbf{k}}\epsilon\nu}} [(\hat{\epsilon} \cdot \mathbf{p}) a_{\mathbf{k},\hat{\epsilon}} e^{i\mathbf{k}\cdot\mathbf{r}}]. \tag{3.16}$$

Figure 3.1 (a) illustrates a photoemission process; due to energy conservation, the energy of final state $|f\rangle$ will be lower than that of the initial state. Photoemission spectroscopy [4] which measures the kinetic energy distribution of emitted photoelectrons is widely used to probe occupied electron density of states. Depending on the incident photons, it can be divided into x-ray photoelectron spectroscopy (XPS) or ultraviolet photoelectron spectroscopy (UPS). The detected kinetic energy $E_{kinatic}$ of the emitted electron can be analyzed by the following formula:

$$E_{kinatect} = \hbar\omega - E_{Binding} - \phi, \tag{3.17}$$

where $E_{binding}$ is the binding energy of electron, $\hbar\omega$ is the energy of the incident photon, and ϕ is the work function of a solid. With a ultraviolet incident photon, one can get the information about the distribution of the occupied valence states, such as chemical information. XPS is a core level spectroscopy reveals the elemental information as well as the chemical information.

(a)

(b)
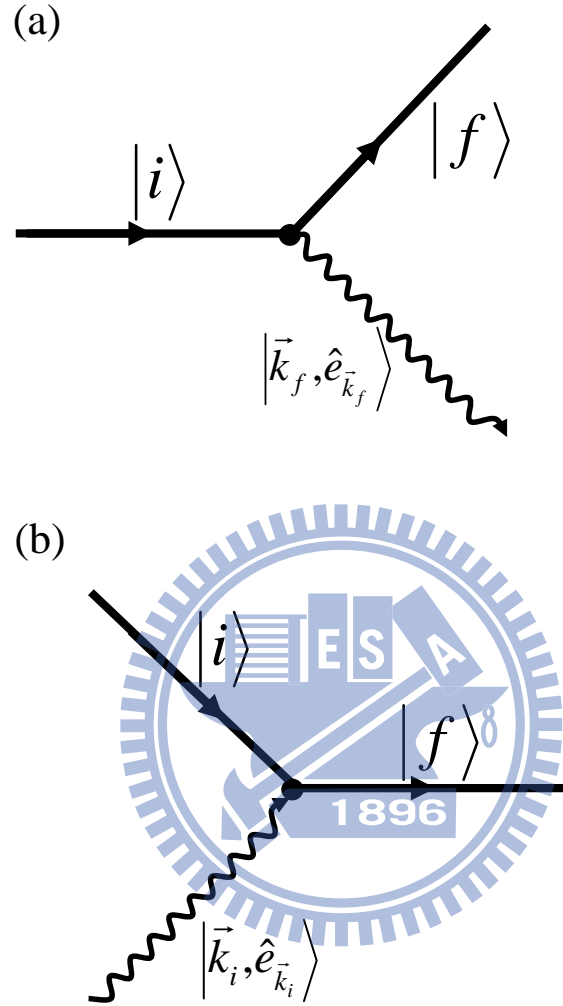
Figure 3.1: Feynman diagrams representing of two first-order processes of the interaction of x-rays with an electronic state. (a) A photoemission process. (b) An absorption process.

3.2.2 X-ray Absorption

The second example of first-order process is absorption as shown in Fig. 3.1.

Again, the transition operators of absorption can be expressed as [2]

$$T_I, em = (\frac{e}{m}) \sum_{\mathbf{k}, \hat{\epsilon}} \sqrt{\frac{\hbar}{2\omega_{\mathbf{k}} \epsilon \nu}} [(\hat{\epsilon}^* \cdot \mathbf{p}) a^{\dagger}_{\mathbf{k}, \hat{\epsilon}} e^{i\mathbf{k} \cdot \mathbf{r}}]. \tag{3.18}$$

X-ray absorption spectroscopy (XAS) [5, 6] is another example of one-step process; if the incoming photon has an energy which can promote a core electron to an empty unoccupied state, then the atom may absorb the incoming x-ray photon. The probability of such kind of transition is the x-ray absorption cross section. XAS gives the information of unoccupied density of states of the material. The decay process has two channels: Auger (nonradiative) decay and x-ray fluorescence emission (radiative) decay. In the soft x-ray region for lighter elements, the Auger decay is usually dominating by a factor 100 over the fluorescence decay. The cascade of electrons from an Auger decay can be collected by measuring the drain current or by electron multiplier. The intensity of the secondary electrons/emitted photons as a function of incident photon will reflect the absorption cross section of the system. X-ray absorption measurements can be conducted by using either the electron-yield or the fluorescence yield. The former is much surface sensitive (about 100 Å penetration depth); the latter is more bulk sensitive (about 1000 $\sim$ 2000 Å). The XAS process is governed by the dipole selection rules, in which the changes in the angular momentum quantum-numbers are Δ L= $\pm$ 1, the orbital momentum Δ m = $\pm$ 1, 0 while the spin is not changed.

3.3 X-ray Scattering

In the following we will discuss about the second-order term in the expression of Eq. (3.15) which involves two photons, one created and one absorbed [2, 3, 7, 8] As mentioned above, after a core hole being created, the whole
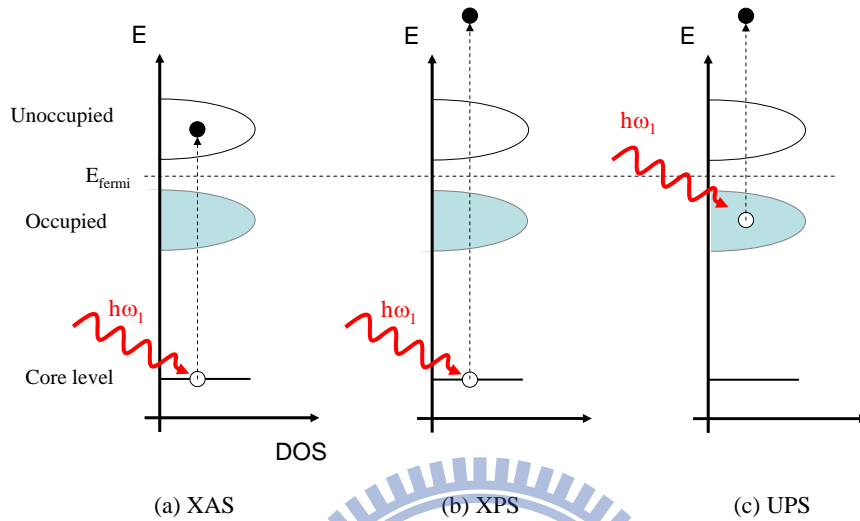
Figure 3.2: Schematic illustrations of x-ray spectroscopy of the first-order optical process in an insulator. (a) X-ray absorption spectroscopy (XAS). (b) X-ray photoelectron spectroscopy (XPS). (c) Ultraviolet photoelectron spectroscopy (UPS).

system will rapidly decays by two channels on a femtosecond time scale. In the second decay channel, x-rays are emitted as a valence electron fills in the core vacancy, denoted as x-ray emission spectraoscopy (XES) [9]. XES measures the intensity distribution of x-rays emitted from the sample. Owing to a large attenuation length of photons, this method is bulk sensitive.

When the excitation energy is well above the ionization (absorption) threshold the x-ray decay process can be described independently from the excitation process; this process is also denoted as normal x-ray emission spectroscopy (NXES) [9, 10]. NXES can be understood as spontaneous emission of photons that obey the diploe transition rules between two electronic states.

The intermediate state of NXES is the same as the final state of XPS. NXES probes the projected partial occupied density of states (PDOS). If the incom-
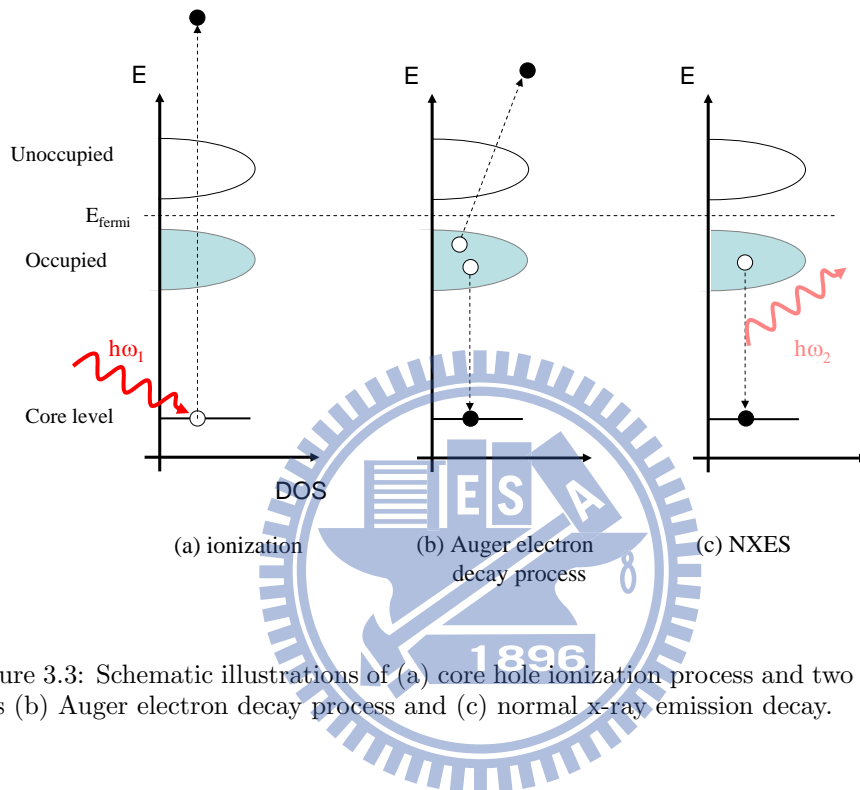
Figure 3.3: Schematic illustrations of (a) core hole ionization process and two decay channels (b) Auger electron decay process and (c) normal x-ray emission decay.

ing photon energy is tuned at the absorption edge, the x-ray decay process called resonant x-ray emission spectroscopy (RXES) [9, 10]. The intermediate state of RXES corresponds to the final state of XAS. Unlike XPS, RXES is a charge neutral techniques, i.e., the numbers of electrons in the ground state and in the final state are identical. Terminologically speaking RXES is sometimes called resonant inelastic X-ray scattering (RIXS) and NXES is sometimes called nonresonant inelastic x-ray scattering (NIXS). The emission feature can be then understood in a "energy loss features" which associated with the energy difference between initial and final states. RXES/RIXS pro-

vide information of correlation effects in the electronic structure and dynamic properties.
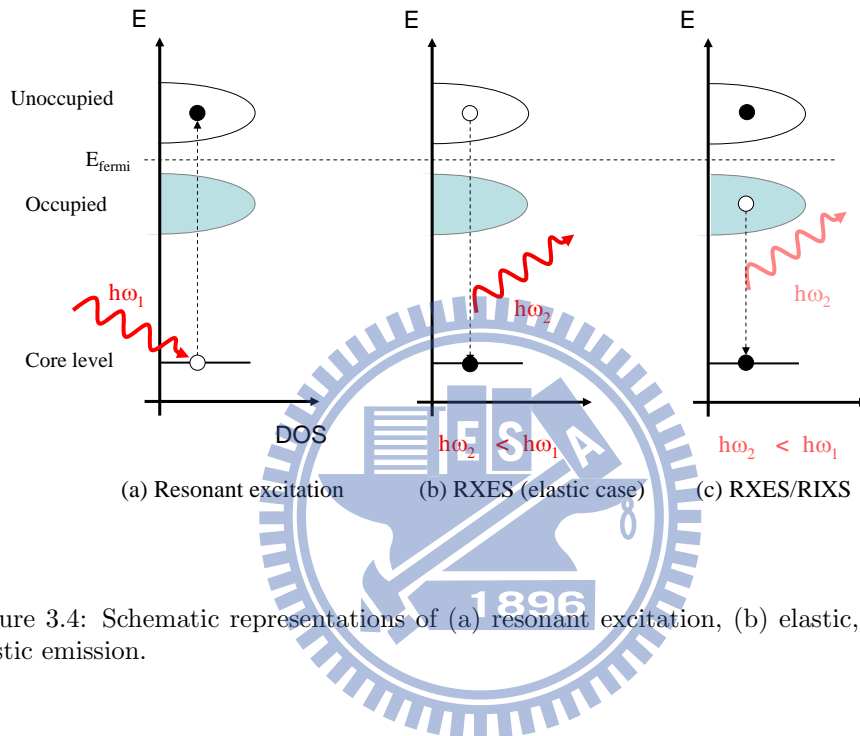
Figure 3.4: Schematic representations of (a) resonant excitation, (b) elastic, and (c) inelastic emission.

In the scattering process, there are three possibilities for such a time-dependent process [2]. The first one is the incoming photon is absorbed at the same time as the outgoing photon is created. The Feynman diagram of this process is illustrated in Fig 3.5 (a). The second possibility so called the direct term; after the incoming photon being absorbed, the outgoing photon is created, as represented in Fig 3.5 (b). In this case, a virtual electron is excited in the time between the two process. The last one is the exchange process shown in Fig. 3.5 (c). In this process the system creates one photon before absorbing the incoming photon. The main difference between (b) and

(c) is the nature of intermediate state $|n\rangle$. For case (b), the intermediate state has one virtual electron and one photon. In contrast, in case (c) it has not only one virtual electron but also two photons.

<div style="text-align:center">(a)   (b)   (c)</div>
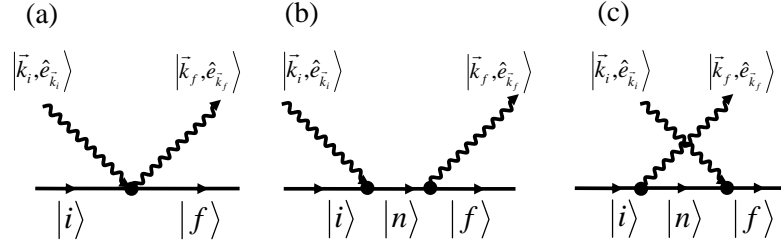
Figure 3.5: Schematic illustrations of Feynman diagrams of three possible scattering process.

Let us call $|\phi_n\rangle$ the intermediate state. Recalling that

$$
\begin{aligned}
G(E_i)|\phi_n\rangle &= \lim_{\epsilon \to 0^+}(E_i - H_p - H_R + i\epsilon)^{-1} \times |\phi_n\rangle|\mathbf{k}_n, \hat{\epsilon}_{\mathbf{k}_n}\rangle \\
&= \lim_{\epsilon \to 0^+}\frac{|\phi_n\rangle|\mathbf{k}_n, \hat{\epsilon}_{\mathbf{k}_n}\rangle}{E_i - \varepsilon_n + \hbar\omega_{\mathbf{k}_n} + i\epsilon}
\end{aligned}
\tag{3.19}
$$

In case (b) and (c) the denominator becomes

$$
\varepsilon_i - \varepsilon_n + \hbar\omega_{\mathbf{k}_i} + i\epsilon \quad \text{for zero photon, and}
$$

$$
\varepsilon_i - \varepsilon_n - \hbar\omega_{\mathbf{k}_f} + i\epsilon \qquad \text{for } \omega_{\mathbf{k}_i} \text{ and } \omega_{\mathbf{k}_f}.
\tag{3.20}
$$

The non-relativistic cross-section of the scattering in which both the initial and the final state contain one photon is

$$
\begin{aligned}
\frac{d\sigma}{d\Omega} &= r_o^2 \frac{\omega_{\mathbf{k_f}}}{\omega_{\mathbf{k_i}}}\delta(\varepsilon_f - \varepsilon_i - \omega)|\hat{\epsilon}_{\mathbf{k}f}^* \cdot \hat{\epsilon}_{\mathbf{k}i}\langle\varphi_f\sum_{i,f}|\hat{e}^{-\vec{q}\cdot\mathbf{r}}|\varphi_i\rangle \\
&+ \frac{1}{m}[\sum_n \frac{\langle\varphi_f|\hat{\epsilon}_{\mathbf{k}f}^* \cdot \mathbf{p}e^{-i\mathbf{k}_f\cdot\mathbf{r}}|\varphi_n\rangle\langle\varphi_n|\hat{\epsilon}_{\mathbf{k}_i} \cdot \mathbf{p}e^{-i\mathbf{k}_i\cdot\mathbf{r}}|\varphi_i\rangle}{\varepsilon_i - \varepsilon_n + \hbar\omega_{\mathbf{k}_i} + i\epsilon} \\
&+ \frac{\langle\varphi_f|\hat{\epsilon}_{\mathbf{k}_i} \cdot \mathbf{p}e^{-i\mathbf{k}_i\cdot\mathbf{r}}|\varphi_n\rangle\langle\varphi_n|\hat{\epsilon}_{\mathbf{k}_f}^* \cdot \mathbf{p}e^{-i\mathbf{k}_f\cdot\mathbf{r}}|\varphi_i\rangle}{\varepsilon_i - \varepsilon_n + \hbar\omega_{\mathbf{k}_f} + i\epsilon}]|^2,
\end{aligned}
\tag{3.21}
$$

where $d\Omega$ is the solid angle of $\mathbf{k}_f$, and r_0 is the classical radius of electron, i.e., $\frac{e^2}{4\pi\varepsilon_0 mc^2}$. The summation is taken over all states and over all electrons in the system, located at $\mathbf{r}$. The δ-function ensures the conservation of energy. This results is known as the Kramer-Heisenberg cross section [11, 12].

As $\hbar\omega_{\mathbf{k}_f} = \hbar\omega_{\mathbf{k}_i}$ is called elastic scattering while $\hbar\omega_{\mathbf{k_f}} \neq \hbar\omega_{\mathbf{k_i}}$ is called inelastic scattering, which leads to $|\varphi_f\rangle \neq |\varphi_i\rangle$ For elastic scattering case, if the incident energy is small than the ionization energy of atom $\hbar\omega_{\mathbf{k_i}} \ll \varepsilon_I$ is called Rayleigh scattering while high energy elastic scattering $(\hbar\omega_{\mathbf{k_i}} \gg \varepsilon_I)$ is called Thomson scattering. For inelastic scattering process, low energy inelastic scattering is called Raman scattering, which can be divided into two regions as $\hbar\omega_{\mathbf{k_f}} < \hbar\omega_{\mathbf{k_i}}$ is called Raman Stokes while the opposite case is called Raman anti-Stoke. The last case is the high energy inelastic scattering which is called Compton scattering.

The cross section consists of three terms. The first term on the right hand side of Eq. (3.21) describes non-resonant elastic and inelastic scattering, including x-ray Raman scattering which will be discussed in next section. In the Thomson case $(\hbar\omega_{\mathbf{k_i}} \gg \varepsilon_I)$, the second and third terms negligible because the denominator is large. In addition, the second term can become singularity as the incoming photon energy is equal to $(\varepsilon_n - \varepsilon_i)$, i.e., under a resonant condition. Actually, it does not completely become singular when the intermediate state $|\varphi_n\rangle$ is short-lived; in other words it has a finite and small life time with will contribute to the denominators in Eq. (3.21). When the incoming beam goes through the absorption edge the contribution of

second term will enhance; such a process is called resonance (or anomalous) scattering. Resonance Scattering reflects the fluorescence(characteristic) radiation and other resonant inelastic scattering phenomena. The direct term (second term) in the Kramers-Heisenber cross-section is often called the resonant term while the exchange term (third term) which cannot be singular is then called the non resonant term.

3.3.1   Resonant X-ray Magnetic scattering

Let us recall Eq. (3.7)

$$H = \frac{1}{2m}[\mathbf{p} - e\mathbf{A}]^2 + eV - \frac{e\hbar}{2m}\mathbf{s}\cdot\nabla\times\mathbf{A} - \frac{e\hbar}{2m^2}\mathbf{s}\cdot\mathbf{E}\times([\mathbf{p} - e\mathbf{A}]) + H_R$$

and rewrite it as

$$H = H_0 + H_R + H_{int} \tag{3.22}$$

where

$$H_0 = \frac{\mathbf{p}^2}{2m} + qV - \frac{e\hbar}{2m^2}s\cdot[\nabla\phi\times\mathbf{p}] \tag{3.23}$$

$$E = -\nabla\phi - \frac{\partial\mathbf{A}}{\partial t}, \tag{3.24}$$

H_0 is the Hamiltonian of the electron without an external interaction. ϕ is the Coulomb potential. Since the spin-orbit term is already $(v/c)^2$, we will omit linear terms in $\mathbf{A}$ and keep only the quadratic ones and those independent of $\mathbf{A}$, so that

$$\frac{e\hbar}{2m^2}\mathbf{s}\cdot\mathbf{E}\times([\mathbf{p} - e\mathbf{A}]) + H_R$$

$$\rightarrow \frac{e\hbar}{2m^2}(\mathbf{s}\cdot(-\nabla\phi\times\mathbf{p} + \mathbf{s}e[\frac{\partial A}{\partial t}\times A]). \tag{3.25}$$

And the interaction Hamiltonian $\mathbf{H}_{int}$ now becomes [2, 3]

$$
\begin{aligned}
H_{int} &= H_1 + H_2 + H_3 + H_4 \\
H_1 &= \frac{e^2}{2m}\mathbf{A^2} \\
H_2 &= \frac{e}{m}\mathbf{A}\cdot\mathbf{p} \\
H_3 &= \frac{e\hbar}{m}\mathbf{s}\cdot[\nabla\times\mathbf{A}] \\
H_4 &= \frac{e^2\hbar}{2m^2}\mathbf{s}\cdot[\frac{\partial\mathbf{A}}{\partial t}\times\mathbf{A}].
\end{aligned}
\tag{3.26}
$$

Here we consider only the scattering, which is involved with quadratic term of $\mathbf{A}$. Therefore the lowest-order contribution processes will come from applying the second-order perturbation to H_2 and H_3, which involves a linear term of $\mathbf{A}$, and by applying first-order perturbation to H_1 and H_4, which involves quadratic term of $\mathbf{A}$.

Let us consider the case that the electron is initially in a state $|i\rangle$ which is an eigenstate of H_0 with energy E_i, and that there is an incoming photon with a wave vector $\mathbf{k}$, polarization $\hat{\epsilon}$ in a state $|\mathbf{k},\hat{\epsilon}_{\mathbf{k}}\rangle$ of energy $\hbar\omega_{\mathbf{k}}$. The interaction will induce a transition into a new eigenstate $|f\rangle$, which is also the eigenstate of H_0 with energy E_i, and the outgoing photon is scatted into a state $|\mathbf{k}',\hat{\epsilon}_{\mathbf{k}'}\rangle$ with energy $\hbar\omega_{\mathbf{k}'}$ The transition probability per unit time is given by the "Fermi Golden rule" via a second-order perturbation

$$
W_{if} = \frac{2\pi}{\hbar}|\langle F|H_1 + H_4|I\rangle + \sum_n \frac{\langle F|H_2 + H_3|n\rangle\langle n|H_2 + H_3|I\rangle}{E_i + \hbar\omega_{\mathbf{k}} - E_n}|^2
$$
$$
\delta[(E_i + \hbar\omega_{\mathbf{k}}) - (E_f + \hbar\omega_{\mathbf{k}'})]. \tag{3.27}
$$

Using Eq. (3.3), we have

$$\frac{\partial \mathbf{A}}{\partial t} = \sum_{\mathbf{k}\hat{\epsilon}} \sqrt{\frac{\hbar}{2\omega_{\mathbf{k}}\epsilon\nu}} i\omega_{\mathbf{k}}[a_{\mathbf{k},\hat{\epsilon}}e^{-i\mathbf{k}\cdot\mathbf{r}}\hat{\epsilon}_{\mathbf{k}} + \mathbf{a}^{\dagger}_{\mathbf{k},\hat{\epsilon}}e^{i\mathbf{k}\cdot\mathbf{r}}\hat{\epsilon}^{*}_{\mathbf{k}}]. \qquad (3.28)$$

If we only consider the low-lying excitations of solids. The matrix element from the first order perturbation is given by:

$$\langle i; \mathbf{k}\lambda|H_1 + H_4|f; \mathbf{k}'\lambda'\rangle$$

$$= \frac{e^2}{2m}\langle i; \mathbf{k}\lambda|\mathbf{A}^2 - \frac{\hbar}{m}\mathbf{s}\cdot[\frac{\partial\mathbf{A}}{\partial t}\times\mathbf{A}]|f; \mathbf{k}'\lambda'\rangle$$

$$= \frac{e^2}{2m}\frac{\hbar}{2\omega_{\mathbf{k}}\epsilon\nu}\langle i|e^{i\vec{q}\cdot\mathbf{r}}|f\rangle(\hat{\epsilon}_{\mathbf{k}'}\cdot\hat{\epsilon}_{\mathbf{k}}) - i\frac{\hbar\omega}{m}\langle i|e^{i\vec{q}\cdot r}\mathbf{s}|f\rangle\cdot(\hat{\epsilon}_{\mathbf{k}'}\times\hat{\epsilon}_{\mathbf{k}}) \quad (3.29)$$

where $\mathbf{q} = \mathbf{k} - \mathbf{k}'$. The first term gives the classical Thomson scattering for Bragg diffraction when $|b\rangle = |a\rangle$ is accounted for. The matrix in a second-order perturbation is.

$$M_2 = \sum_n \frac{\langle F|H_2 + H_3|n\rangle\langle|H_2 + H_3|I\rangle}{(E_0 + \hbar\omega) - (E_n + \frac{i\Gamma_n}{2})}$$
$$+ \frac{\langle F|H_2 + H_3|n\rangle\langle|H_2 + H_3|I\rangle}{(E_0 + \hbar\omega) - (E_n + \hbar\omega + \hbar\omega)} \qquad (3.30)$$

The first term represents that the incoming photon is absorbed, while the second one corresponds to the case a photon is emitted. Note that $\frac{i\Gamma_n}{2}$ is also present in the second term but since the real part never vanishes, so it could be ignored. The matrix

$$M_2 = \sum_n (\frac{e}{m})^2 \frac{\hbar}{2\varepsilon\nu}\frac{1}{\sqrt{\omega_{\mathbf{k}}\omega_{\mathbf{k}'}}}\{$$
$$\frac{\langle F|[(\mathbf{p}\cdot\hat{\epsilon}_{\mathbf{k}'}) - i\hbar\mathbf{s}\cdot(\mathbf{k}'\times\hat{\epsilon}'_{\mathbf{k}})]e^{i\mathbf{k}'\cdot\mathbf{r}}|n\rangle\langle n|[(\mathbf{p}\cdot\hat{\epsilon}_{\mathbf{k}}) + i\hbar\mathbf{s}\cdot(\mathbf{k}\times\hat{\epsilon}_{\mathbf{k}})]e^{i\mathbf{k}\cdot\mathbf{r}}|I\rangle}{(E_0 + \hbar\omega) - (E_n + \frac{i\Gamma_n}{2})}$$

$$+\frac{\langle F|[(\mathbf{p}\cdot\hat{\epsilon}_{\mathbf{k}})-i\hbar\mathbf{s}\cdot(\mathbf{k}\times\hat{\epsilon}_{\mathbf{k}})]e^{i\mathbf{k}\cdot\mathbf{r}}|n\rangle\langle n|[(\mathbf{p}\cdot\hat{\epsilon}_{\mathbf{k}'})-i\hbar\mathbf{s}\cdot(\mathbf{k}'\times\hat{\epsilon}_{\mathbf{k}'})]e^{-i\mathbf{k}'\cdot\mathbf{r}}|I\rangle}{(E_0+\hbar\omega)-(E_n+\hbar\omega+\hbar\omega)}\}$$

$$(3.31)$$

Let us now consider the case of resonant scattering, where $\hbar\omega\sim E_l=E_0$. The scattering amplitude will then be dominated by the first part of Eq. (3.26). The spin-dependent term become

$$\frac{\langle F|(\mathbf{k}'\times\hat{\epsilon}_{\mathbf{k}'})\cdot\mathbf{s}e^{-i\mathbf{k}'\cdot\mathbf{r}}|n\rangle\langle n|(\mathbf{k}\times\hat{\epsilon}_{\mathbf{k}})\mathbf{s}\cdot]e^{i\mathbf{k}\cdot\mathbf{r}}|I\rangle}{(E_0+\hbar\omega)-(E_n+\frac{i\Gamma_n}{2})}$$

$$(3.32)$$

This is the differential cross section for magnetic x-ray scattering. The magnetic scattering term are smaller by a factor of $\frac{\hbar\omega}{m}$ in amplitude than the charge term. Resonant exchange scattering was first observed in Ho by Gibbs et al, [13] and Hannon et al., [8] (1988) derived the general dependence of the resonant scattering amplitude. For the polarization vectors of incident and scattered x-rays being $\hat{\epsilon}$ and $\hat{\epsilon}'$, the resonant scattering amplitude of x-ray with wavelength λ is

$$\begin{aligned}f_{\text{res}} &= (\hat{\epsilon}\cdot\hat{\epsilon}')[-r_eZ+\frac{3\lambda}{8\pi}[F_{1,1}-F_{1,-1}]]+i\frac{3\lambda}{8\pi}(\hat{\epsilon}'^*\times\hat{\epsilon})\cdot\hat{\mathbf{m}}[F_{1,1}-F_{1,-1}]\\&+(\hat{\epsilon}'\cdot\hat{m})(\hat{\epsilon}\cdot\hat{m})\times\frac{3\lambda}{8\pi}[2F_{1,0}-F_{1,1}-F_{1,1}],\end{aligned}$$

$$(3.33)$$

where $F_{1,1}$ and $F_{1,-1}$ are the scattering amplitudes associated with the changes of magnetic quantum number $\Delta m=1$ and $\Delta m=-1$ [8]; $\hat{m}$ is the quantization axis of magnetization. The first term is the charge scattering. Like x-ray magnetic circular dichroism in absorption, the imbalance between the scat-

tering amplitudes associated with the change of magnetic quantum number Δm yields the spin sensitivity in x-ray magnetic scattering [14, 15, 16, 17, 18].

Complementary to neutron scattering, resonant soft x-ray magnetic scattering is an effective experimental method to probe the magnetic order of transition metals with a good momentum resolution. With photon energy tuned around the L-edge ($2p \rightarrow 3d$) absorption of transition metal, resonant soft x-ray scattering takes place through a dipole allowed transition, and a core-level electron Ψ_{2p} is virtually promoted to an intermediate state Ψ_{3d} above the Fermi level. The resonance effect enhances the scattering cross section dramatically and gives rise to a direct probe of the ordering of $3d$ states in transition metals.

3.3.2 Resonant Inelastic Soft-X-ray Scattering (RIXS)

The interaction between light and matter gives the information of the electronic and magnetic structure of solids. With the increasing brilliance of x-ray source and optics in third-generation synchrotrons, inelastic x-ray scattering has become a powerful and rapidly develop technique for studying the low-energy excitations of advanced materials [9, 10, 19, 20]. Resonant inelastic x-ray scattering (RIXS) is a unique tool which provides spin, charge and orbital information both in momentum and energy scale; it is element specific. RIXS is an photon-in photon-out spectroscopy; during the measurement the energy is tuned to the absorption edge of the particular element of interest, so that the inelastic scattering intensity of certain electronic ex-

citation is resonantly enhanced. After the core hole is created the excited
state will decay rapidly on the femtosecond time scale by emitting an Auger
electron or an x-ray photon, the later one so-called the x-ray emission. If
the energy of the incoming photon and out-going photon are the same, this
is elastic scattering. If the energy of out going photon is slightly lower than
the incoming photon then it is the inelastic x-ray scattering. The energy
difference between in-coming photon and out-going photon is the transferred
energy or the energy loss. Such an element specificity is valuable in studying
complex materials such as the cuprate compounds. It measures not only
the energy of these excitations, but can also identify which atomic sites are
involved in the excitation. Measurements of the electronic structure with q
resolution can also achieved by using other techniques such as photoemission.
However, for the insulators such kind of ionizing measurement is problem-
atic due to sample charging, RIXS is a photon-in photon-out process can
be applied to insulators. Unlike optical transition in the infra-red or visible
light, which used to study the charge excitations,the momentum transfer are
restricted nearly to zero due to the transfer.

The potential of L_3 RIXS was suggested some years ago. However up to
now, the information has been buried in low-resolution spectra, and the avail-
able data could not be effectively used to put stringent constraints on the the-
oretical parameter. The situation is changing because of the advancements in
synchrotron radiation and spectrometer techniques. Recent improvments call
for new investigations of correlated systems including benchmark cases such

as simple oxides of $3d$ transition-metals (TMs). $3d$-transition-metal (TM) compounds, such as cuparate, are regarded as strongly correlated materials. In these systems, electron-electron interactions are strong and 3d electrons usually are localized. Atomic-like discrete excitations must be considered. Therefore the electronic structure of those materials is often described on the terms of low-energy dd (d to d) and charge-transfer (CT) excitations. The whole scattering process follows the energy conservation low, and one can obtain information about the ground state of the system via intermediate excitation of core electron. This process obeys the following formula:

$$h\nu_1 = h\nu_2 - E_{exc,} \tag{3.34}$$

where $h\nu_1$ and $h\nu_2$ are the energy of the outgoing and incoming photons, respectively. E_{ecx} is the excitation energy of the final state (as shown in Fig. 3.6). Interestingly, the energy of the intermediate state does not occur in the above equations. As a result, the spectral broadening is not related to the lifetime of the intermediate state. The overall resolution of the spectra is only limited to the experimental setup, i.e. the excitation source (width of hν_1) and the spectrometer resolution. Figure 3.6 visualizes the the RIXS process by an energy level diagram. Because two virtual diploe transitions are involved in the RIXS process, the final state has the same parity as the initial state. As a consequence, the so called crystal-field excitations between d orbitals of different symmetries are allowed.

The dependence of excitation could be related to the presence of crys-
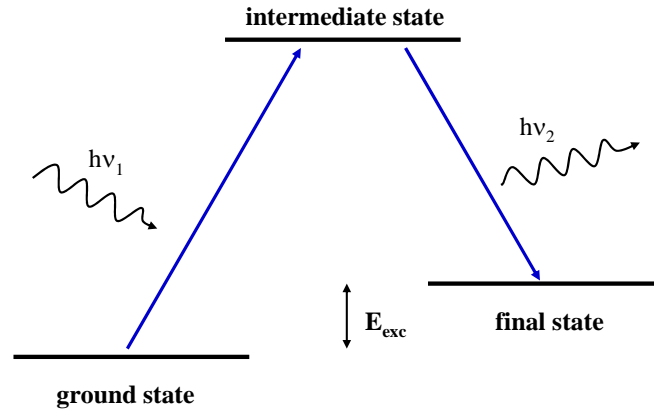
Figure 3.6: Schematic illustration of the RIXS process in an atomic-like environment.

tallographic structure which is closely connected to electronic structure in the system. When the momentum is conserved in the resonant inelastic scattering process, the fluorescence spectra can be interpreted within the RIXS formalism. The scattering process can be viewed as a vertical optical transition between valence and the conduction band. A specific excitation energy selects a conduction band at a particular point in the Brillouin Zone (BZ). Emission will occur from those critical points on the valence band, that have the same momentum as the selected conduction

band. The momentum conservation process can be written as

$$k_v + q_{in} = k_c + q_{out} + \mathbf{G} \tag{3.35}$$

where k_v is the momentum of the electron in the valence band and k_c is the momentum of the electron in the conduction band. The momenta of the incoming and outgoing photons are q_{in} and q_{out} , and $\mathbf{G}$ is a reciprocal lattice vector.

As mentioned above, if the energy of incident photon is far from the absorption edge, the direct term and exchange term of Eq. (3.18) can be neglected and the Kramer-Heisenber formula simplifies to

$$
\begin{aligned}
\frac{d^2\sigma}{d\Omega d\omega_{\mathbf{k}_f}} &= r_o^2 \frac{\omega_{\mathbf{k}_f}}{\omega_{\mathbf{k}_i}} (\hat{\epsilon}_{\mathbf{k}_i} \cdot \hat{\epsilon}_{\mathbf{k}_f}) \sum_{i,f} |\langle \varphi_f | \hat{e}^{-\mathbf{q}\cdot\mathbf{r}} | \varphi_i \rangle|^2 \cdot \delta(\varepsilon_f - \varepsilon_i - \omega) \\
&= (\frac{d\sigma}{d\Omega})_{Th} S(\mathbf{q}, \omega),
\end{aligned}
\tag{3.36}
$$

where the Thomson cross section

$$
(\frac{d\sigma}{d\Omega})_{Th} = r_o^2 \frac{\omega_{q_f}}{\omega_{\mathbf{k}_i}} (\hat{\epsilon}_{\mathbf{k}i} \cdot \hat{\epsilon}_{\mathbf{k}f})^2,
\tag{3.37}
$$

this term describe the electron-phonon coupling and the strength depends only on the scattering geometry of the incident photon polarization and outgoing photon polarization. The other term is the dynamic structure factor,

$$
S(\mathbf{q}, \omega) = \sum_{i,f} |\langle \varphi_f | \hat{e}^{-\mathbf{q}\cdot\mathbf{r}} | \varphi_i \rangle|^2 \delta(\varepsilon_f - \varepsilon_i - \omega).
\tag{3.38}
$$

The information of the dynamic structure factors derived by van Hove is [21]

$$
S(\mathbf{q}, \omega) = \frac{1}{2\pi} \int \int dt \, d\mathbf{r} e^{i\mathbf{q}\cdot\mathbf{r}} - \omega t \int d\mathbf{r}' \langle \rho(\mathbf{r}', 0) \rho(\mathbf{r}' + \mathbf{r}, t) \rangle,
\tag{3.39}
$$

where $\rho(\mathbf{r}, t)$ is the microscopic particle density operator with the particle at position $\mathbf{r}$ and at time t and the brackets represent the expectation value taking over the ground state. This formula reveals that the dynamic structure factor connecting the dynamics and spatial distributions of density fluctuations of a electron system through a Fourier transformation of the electron

density-density correlation function. The coherent part can be divided into two parts, inelastic and elastic scattering. The inelastic scattering is due to the dynamic correlation of the particles at two different positions at different time, and the elastic scattering is due to the static correlations of the particles at two different positions in the limits where $t \to \infty$.

Thus by studying the dynamic structure factor in $(\mathbf{q}, \omega)$ space the dynamics and the spatial distribution of the density fluctuation in a system can be approached. The spatial and time scales on which the density correlations are studied are determined by the magnitude of the momentum transfer $\mathbf{q}$ and the energy transfer ω. When the $\frac{1}{q}$ is considerable large than the relevant length scale of the system, for example long-range density correlations, i.e., collective excitation, contribute to the $S(\mathbf{q}, \omega)$. On the other hand, with large momentum transfer value, the short range correlation are emphasized.

Another interesting XRS related experiments is resonant inner shell excitation, which connects the XRS cross section to the x-ray absorption cross section. As the transferred energy ω in Eq. (3.34) is replaced by the energy ω_i of the incident photon and the momentum transfer $\mathbf{q}$ with the polarization vector ϵ_i, the dynamic structure factor will become proportional to the x-ray absorption cross section.

3.4   Instrumentation

3.4.1   Resonant Soft X-ray Magnetic Scattering

Figure 3.7 shows a photograph of a two-circle UHV diffractometer equipped with a liquid He cryostat. The typical vacuum pressure is on the order of 10^{-9} Torr without bakeout. Two temperature sensors were installed; one is on the cold finger and the other is on the sample holder. With a semi-cylindrical shield installed, the best temperature is 6 K at sample position. The diffractometer chamber is a cylindrical vessl with an internal diameter 609 mm.
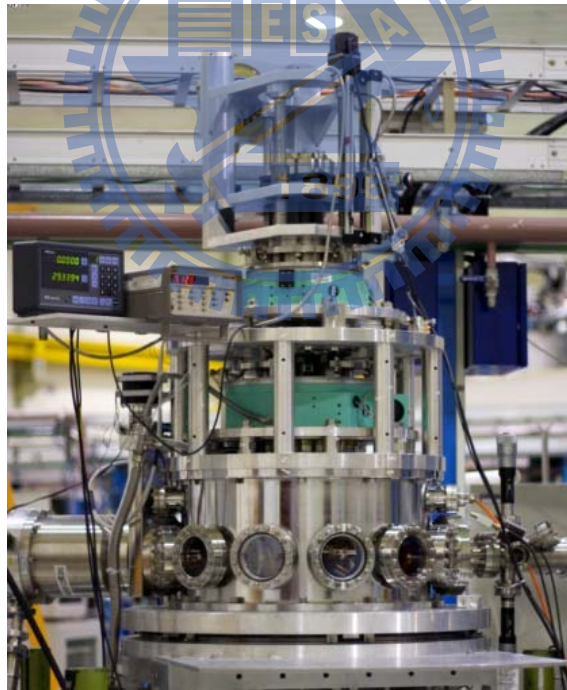
Figure 3.7: Photograph of a two-circle UHV soft X-ray diffractometer.

Two rotation goniometers for independent rotations of the sample (θ)

and the detector (2θ) are concentrically mounted on the cylinder axis of
the vacuum chamber, allowing us to perform scans of momentum transfer q
along the surface normal ($q_\perp$) and in an another orthogonal direction ($q_\parallel$)
in the scattering plane. Scattered light was detected by either a photodiode
or a homemade channeltron detector depending upon the intensity. The
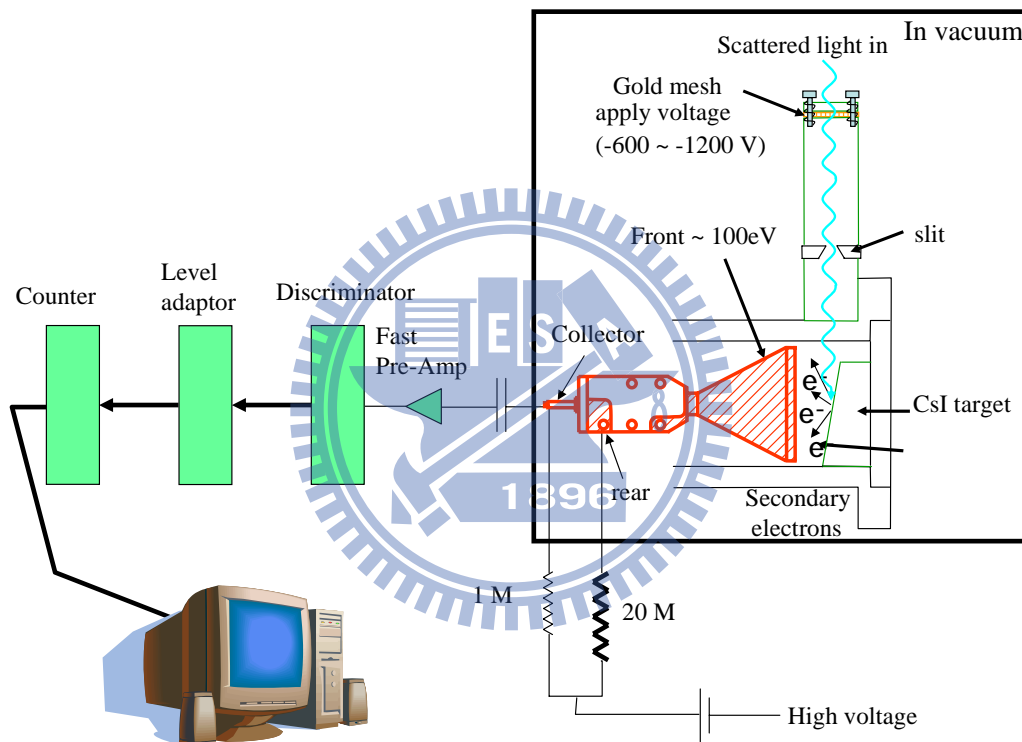
Figure 3.8: Illustrations of the florescence detector and the block diagram of data acquisition. .

channeltron detector is composed of a slit, a mesh, a CsI photon-to-electron
convertor and a channeltron electron multiplier. A slit with 1.5 mm width is
located in front of the electrode is used to set the momentum resolution. A
negative voltage of -600 $\sim$ -1200 V, depending on the incident photon energy,

was applied on the mesh to expel the emitted electron from the sample. The scattered light passing through the slit will hit the CsI target and generate large numbers of secondary electrons. By applying a bias of 100 V on the front of the channeltron, secondary electrons will collected by the channeltron. The channeltron itself operates on plateau voltage to minimize the fluctuation of gain. The output signal was detected by a pulse-counting mode. The pules signals were first amplified by a preamplifier. Then a discriminator converte a analog pulse into a digital signal and by adjusting the discriminator threshold we can separate the electronic noises and real signals. After the discriminator the signal is stretched by a level adaptor then the signals are finally counted by a counter.

For photons of 630 eV, the instrumental resolution of $q_\parallel$ and $q_\perp$, defineed as the half-widths at half maximum (HWHM), are estimated to be of 0.001 and 0.0003 Å^{-1}, respectively.

3.4.2 Resonant Inelastic Soft X-ray Scattering—Traditional Designed

The signal of RIXS is usually weak, a high-intensity, high resolution soft x-ray source and a very efficient monochromator and spectrometer are needed [22]. In order to meet these two stringent requirements of RIXS experiments in the soft x-ray region the NSRRC has designed and constructed a new soft x-ray inelastic beamline based on the principle of energy compensation for grating dispertion [23]. This soft x-ray RIXS beamline system has signal-
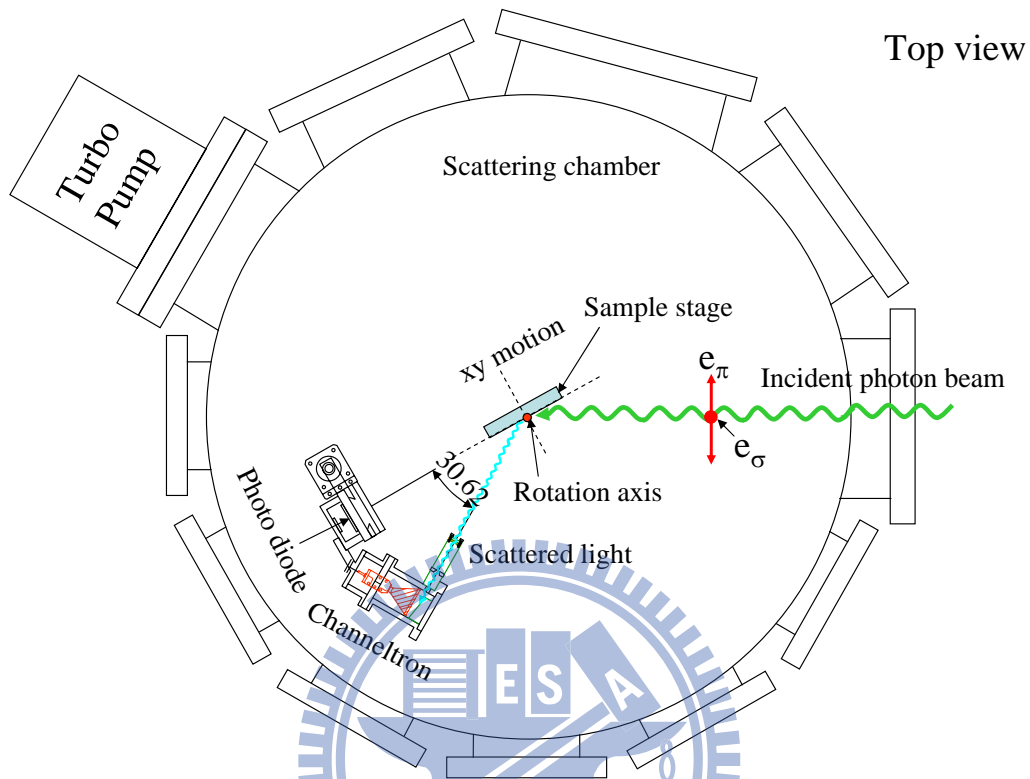
Figure 3.9: Top view of the scattering geometry.

collection efficiency higher than that of conventional design by two orders of magnitude, while reaching a resolving power of 30,000 in the energy loss spectra.

Undulator Source

The photon source of the 05 beamline is the EPU56 undulator installed in a straight section of Taiwan light source (TLS). This is a Apple-II type elliptically polarized undulator with a magnet period of 5.6 cm. There are four arrays can be shifted in the longitudinal direction; however, we used two diagonal arrays fixed and the other two freely movable to create the linear

polarization on vertical/horization plane and the right/left elliptical, circular polarization light. If the two fixed arrays are free, it can also produce the linear polarization with the polarization vector varies from 0° to 180°.

General setup for Resonant Inelastic Scattering

Generally speaking a setup of a traditional inelastic scattering experiment includes two parts, a monochromator used to provide single-wavelength photon and a spectrometer for selecting the energy of scatted photons. Those two instruments equally contribute the final energy resolution. Monochromatization
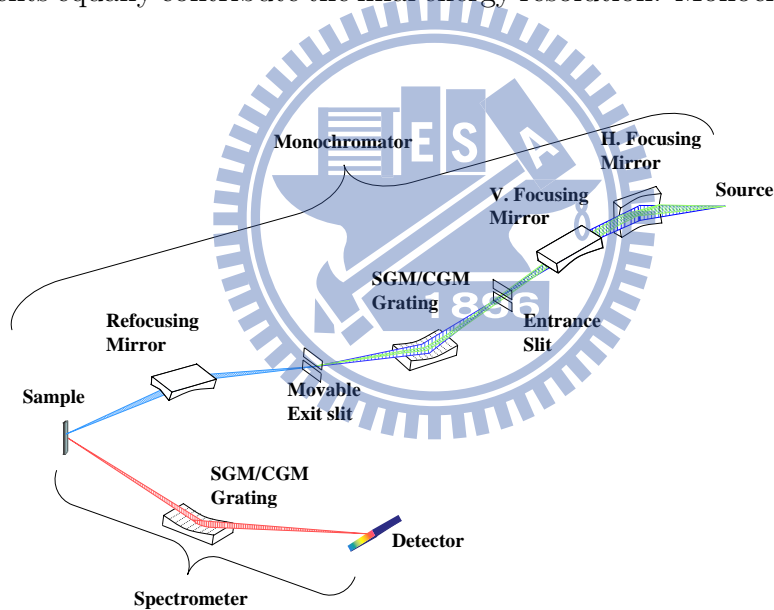
Figure 3.10: The layout of a conventional soft x-ray inelastic scattering beamline. SGM and CGM stand for spherical and cylindrical grating monochromator, respectively.

of a soft X-ray photon is usually obtained by a grating. The monochromators mainly used in soft x-ray region are: (i) spherical grating monochromator, (ii) plane grating monochromator, and (iii) toroidal grating monochroma-

tor. With a spherical grating monochromator which is called the Dragon

type monochomator as an example [24], a soft x-ray beamline consists of a

series of high precision optical elements, including horizontal focussing mir-

ror (HFM), vertical focussins mirror (VFM), entrance slit, grating, moveable

exit slits and refocussing mirror. The beamline conducts monochromative

and focus the radiation on the sample. The HFM collects and focuses the

horizontal part of light from the synchrotron onto the center point of the

exit slit. The VFM focuses the vertical part of the synchrotron light onto

the fixed entrance slit. At the grating the light is diffracted according to the

grating equation.

$$n\lambda = d(sin\alpha - sin\beta), \qquad (3.40)$$

where $n = \pm 1, \pm 2, \pm 3, ...,$ d is the grating constant which stands for the

distance between two grooves, and α and β are the angle of incident and

diffracted light, respectively. Light of different wavelengthes will diffract to

different angles, and being focused onto the vertical position of exit slit. The

moveable exit slit will select the desire photon out. Finally, a re-focussing

mirror directs and focuses the light to the experimental end station. The

major optical abberations of a Dragon type monochromator are astigmatic

coma aberration, defocus aberration and coma abberation. Abberations will

reduce the resolving power of the monochromator. An independent focusing

system in the horizontal and vertical directions, *i.e.,* the Dragon type design,

could eliminate the astigmatic coma aberration. Due to the fixed curvature of

grating, different photon energy will have different focal lengths, a moveable

exit slit could eliminate the defocus aberration. And an non-spherical grating can compensate the coma abberation.

In principle the energy of incident light is determined by a grating. The energy resolving power of a system is a ability of how finely it is able to distinguish between photons of different energies. Except for aberrations, the opening of entrance slit and exit slit, the surface roughness of optical elements and so on all reduce the resolution. By inserting appropriate optical elements between entrance and exit slit, one could exclude some aberrations. However, optical elements are not always in a perfect shape which will smear out the expected energy resolution. Furthermore, each optical element will reduce 20% to 60% flux depending on the incident photon energy. Thus the setup of an ideal monochromator is having only one optical element, grating, between the entrance and exit slit.

The purpose of a spectrometer is to analyze the energy emitted by the sample. A spectrometer provides a way to collect the emitted photon, to count them and to select their energy. Theocratically speaking, it contains an entrance slit after the sample, a grating, an exist slit just in front of the photon detector and a photon detector. Usually, the cross section of inelastic scattering is extremely low. If the beam spot refocussed by the re-focussing mirror illuminate on the sample is only several μm, an slitless of spectrometer can operate. As we know through the grating photons of different energies will reflect and disperse into different directions. A spatial resolution detector, for example charge couple device (CCD) detector can

consider as the virtual exit slit of spectrometer.

3.4.3 A Novel Design for Resonant Soft X-ray Inelastic Scattering

The requirement of a soft x-ray spectrometor with good performance is twofold: resolving power and efficiency. In order to enhance the efficiency of an inelastic scattering experiment, we are developing a novel soft x-ray RIXS beamline constricted based on the principle of energy compensation for grating dispersion.

AGM-AGS beamline

The AGM-AGS beamline is located at the downstream of 4-meter long elliptical polarized undulator (EPU) at National Synchrotron Radiation Center Hsinchu Taiwan. A horizontal focus mirror (HFM) focuses x-rays on the sample position in the horizontal direction, and a vertical focus mirror (VFM) focuses the beam on the entrance slit in the vertical direction. An active grating is mounted at 3.5 m away from the entrance slit, and a monochramatic single wavelength beam is focused onto the sample position which is 2.5 m after the grating. For thw spectrometer, a position sensitive photon detector and an active grating are located at positions corresponding to the entrance slit and the active grating of monochromater, respectively.

Principle of Energy Compensation

The optical concept of AGM-AGS is based on the principle of energy compensation [25]. By using the two identical aspherical variable-line-space ac-
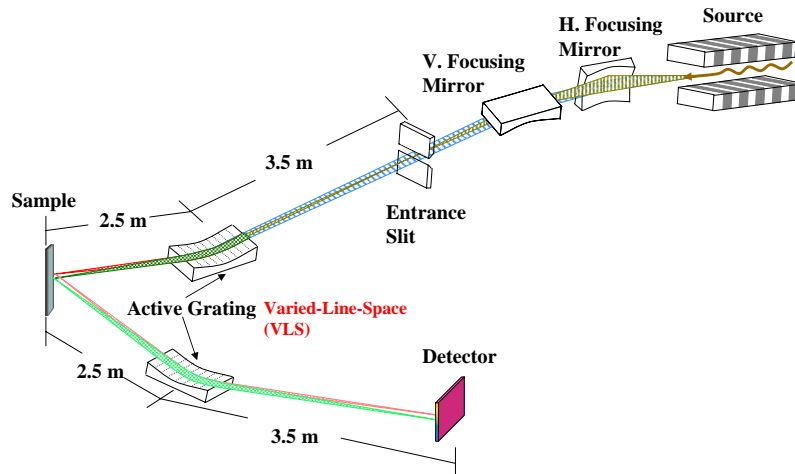
Figure 3.11: A layout of the AGM-AGS beamline.

tive gratings and applying the energy compensation principle, F. S. Fung *et al.*,found [23] that the efficiency of the AGM-AGS is two orders of magnitude high than that of conventional design while a very high spectral resolution is maintained. After the incident photon passing through the entrance slit, grating will disperse the incident light with different energies to different angles. From the concept of energy compensation one could conclude that, inelastic scattered light with same energy loss, will be focused on the same position of a position sensitive detector.

Consequently, the signal collection efficiency of AGM-AGS is greatly increased as compared with conventional designs that do not apply the energy compensation principle. The energy resolution of an AGM-AGS setup depends on both the opening of the entrance slit and the pixel size of the area
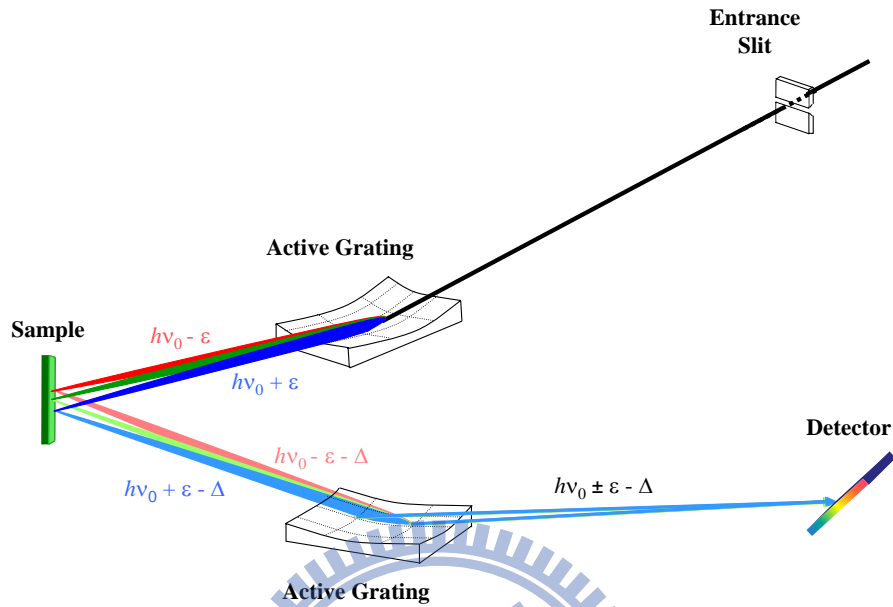
Figure 3.12: Illustration of the principle of energy compensation.

detector, but independent on the energy variation ε. Under the condition of maximal resolution, the illuminated beam size in the vertical direction of a conventional monotromator is about several μm; with the energy compensation principle, it can become several hundred μm without losing the energy resolution. The collection efficiency is hence increased by two orders of magnitude .

In addition, an AGM beamline can completely eliminate the refocus and coma aberrations which limit the spectral resolution of a conventional SGM design.

Active Grating

A grating which can disperse, focus and eliminate aberrations is the key optical element of our new soft x-ray spectrometer. The radius of the active grating can be changed from 75 m to 155 m for photon energy 400 eV to 1400 eV to achieve a good resolving power [26, 27]. The surface profile of the grating is described by the following equation:

$$\xi(\omega) = c_2 \xi^2 + c_3 \xi^3 \tag{3.41}$$

ξ and ω are the surface coordinates. According to the optical path function and Fermat's principle c_2 is the radius of curvature of the grating and c_3 has significant impact of coma aberration.

Since the surface profile of the active grating is a third order polynomial, two control parameters are required to achieve a surface profile of a third-order polynomial. Two important criteria to be taken into consideration for the bending mechanism of a grating. First, the center point should be stationary under different curvature. Second, the size of the bender, particulary the height can not exceed the chamber size. A "⊓"-like shape substrate is used as the base foundation [28, 29]. Two actuators are used to push the side legs to achieve a concave grating surface. The dimensions of the bender are $320 \times 40 \times 47.5$ mm^3; the length of ⊓ shaped base is 230 mm and the thickness is 10 mm. The thickness of the side legs is 17.5 mm A 5 mm Si based grating is glued on the top of the plate with a 40 mm effective ruling length and a minimum radius of curvature of 50 m.
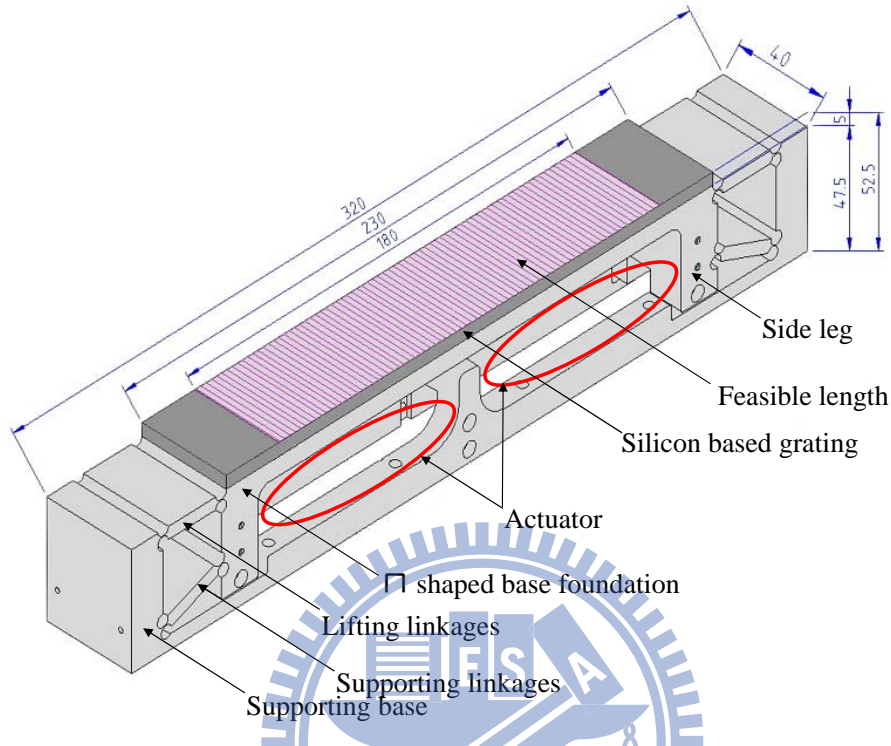
Figure 3.13: Design of the the active grating taken from [27].

In order to make the incident photon beam focus on a nearly vertical plane rather than on a inclined curved surface a varied-line space (VLS) grating is adopted. The line density across the surface of a VLS grating is not constant but varies with the distance from the grating origin. The groove density n(ω) is typically described by a polynomial as:

$$n(\omega) = n_0 + n_1\omega + n_2\omega^2 + \cdots\cdots \qquad (3.42)$$

where n_0 is the groove density at the center of the grating origin. In our case, it is 1200 lines/mm and the coefficients n_i are the design parameters.

Charge Coupled Devices (CCD)

A position sensitive detector could increase the effieincy of a spectrometer. A charge coupled devices (CCD) is one of the best candidate for soft x-ray area detectors. A CCD can be consider have many the virtual exit slit of the spectrometer. Two back-illuminated CCD detectors made with Si wafer were adopted in our experiment. One is commercial Princeton PI-SX with 13.5 μm pixel size and 2048×2048 pixels. The lowest operating temperature is $-65°$ C. The other is customer design Andor iKon-M 934. The other sensor array is 1024×1024 pixel with 13 μm pixel size, and the working temperature could reach to -95°C. The image plane flushes with the flange, allowing us to mount the CCD at grazing incidence to increase spatial resolution. This CCD camera has two acquisition modes: accumulated mode and photon counting mode. By setting the upper and lower limit, the photon counting could filter out the background and electronic noises.

3.4.4   Commissioning Results of Novel Soft X-ray Inelastic Beamline

Figure 3.14 shows a scheme of the L_3 edge RIXS process. The ground state of transition-metal oxide is usually a linear combination of the normal ground state $(3d^n)$ and the charge transfer state $(3d^{n+1}\underline{L})$. The energy difference between the two "non-interacting" states is indicated by $\triangle$, and called charge transfer (CT) energy, where the $3d^{n+1}\underline{L}$ represent a hole in the oxygen $2p$ valence band, i.e., an electron in oxygen $2p$ is transferred to transition metal

$3d$ state through the $p - d$ hybridization, n is the real $3d$ occupation number and $\underline{L}$ indicate a hole on the neighboring oxygen. Because the O $2p$ states are having the delocalized characteristic, the $3d^{n+1}\underline{L}$ state has a finite bandwidth W. The scattering process can be represent as $3d^n \rightarrow 2p^5 3d^{n+1} \rightarrow 3d^{n*}$. $3d^{n*}$ stands for a final state where the number of the $3d$ electrons are the same as that of the ground state but having different occupation among the available ortials, i.e, dd excitations.
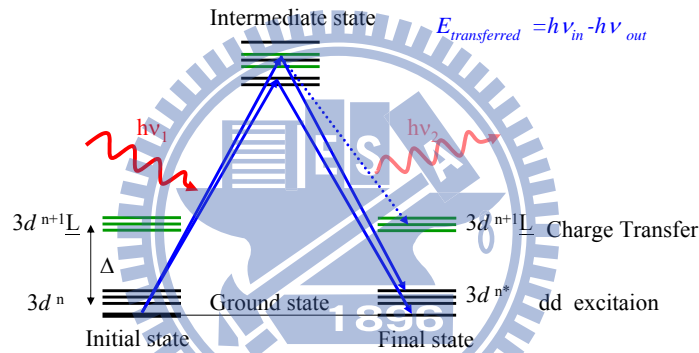
Figure 3.14: Electronic excitations probed by RIXS.

In order to characterize the spectral resolution and to demonstrate the performance of the beamline, photoionization measurements of gas molecules are commonly used to test the resolution of a monochromator. The energy resolution of the AGM-AGS beamline has been measured from neon gas. During the measurements, the pressure of the gas cell was kept at 1×10^{-2} mTorr and the potential difference between electrodes was 90 V. The recorded of the $1s$ spectra $\longrightarrow np$ Rydberg excitations of Ne gas are shown in Fig. 3.15. The total measured line width of the $1s \longrightarrow 3p$ transition at 872 eV was

307 meV, where the nature width of this transition is about 254 meV. Our instrument resolution is therefore better than 180 meV, and the resolving power over 4800.
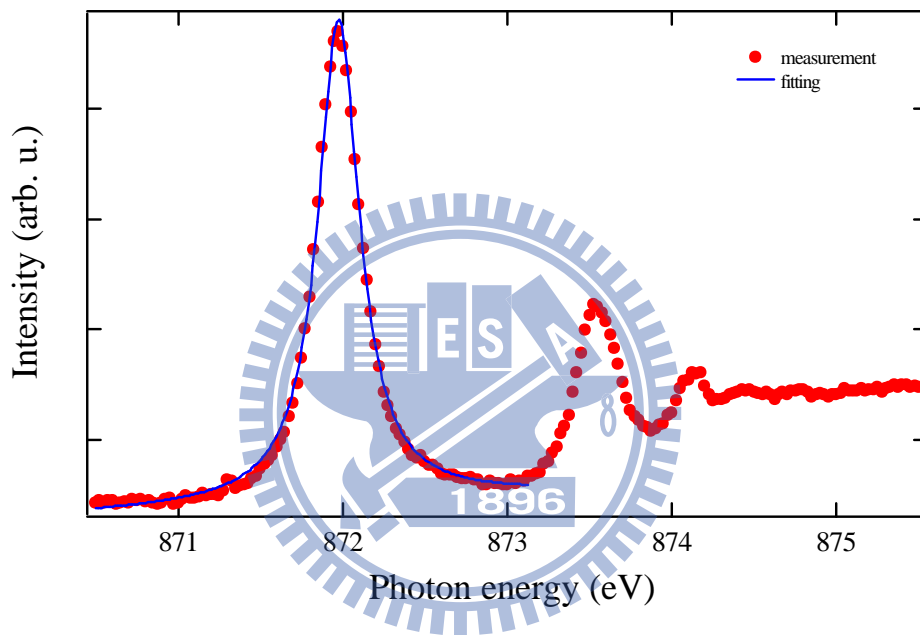
Figure 3.15: K-edge x-ray absorption spectrum of Ne.

The central question of the new design soft X-ray inelastic beamline is whether the energy compensation principle can works or not. We address this question by measuring a series of collective energy loss spectra of NiO. We first concentrate on the RIXS measurement of NiO L_3 edge. All data were collected with accumulation low noise mode. The combined energy resolution is 240 meV as measured by the full width at half maximum (FWHM) of the specular elastic peak. In this measurement, the scattered light is normal to

the CCD sensor, which has 13.5×13.5 μm pixel size 2048×2048 pixels.
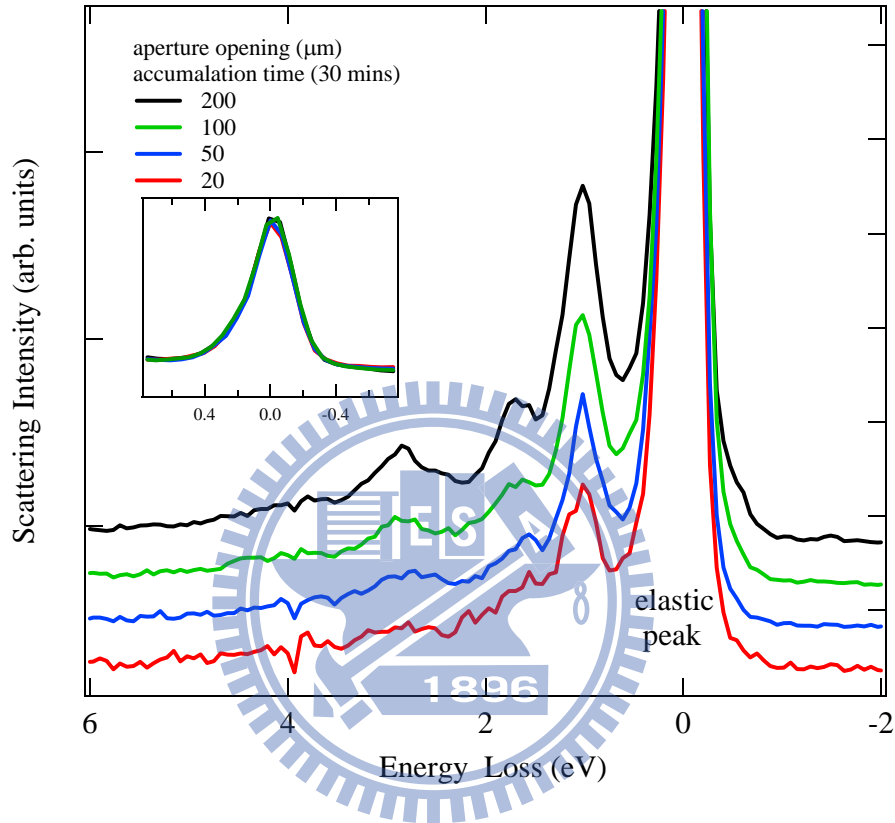
Figure 3.16: RIXS spectra of NiO with different aperture opening. The incident energy was set at Ni L_3-edge. The inset shows the normalized elastic peaks.

Our results are consist with previous published results [20, 30]. Furthermore, we confirmed that the new designed AGM-AGS RIXS beamline yields RIXS spectra as traditional RIXS beamline. To examine the principle of energy compensation, we measured the energy loss spectra with different openings of the aperture located in front of the sample, using an incident photon energy of 857 eV. The results are shown in Fig. 3.16. For the open-

ing of the aperture small than 200 μm the energy resolution is not smeared
out by the size of the aperture.
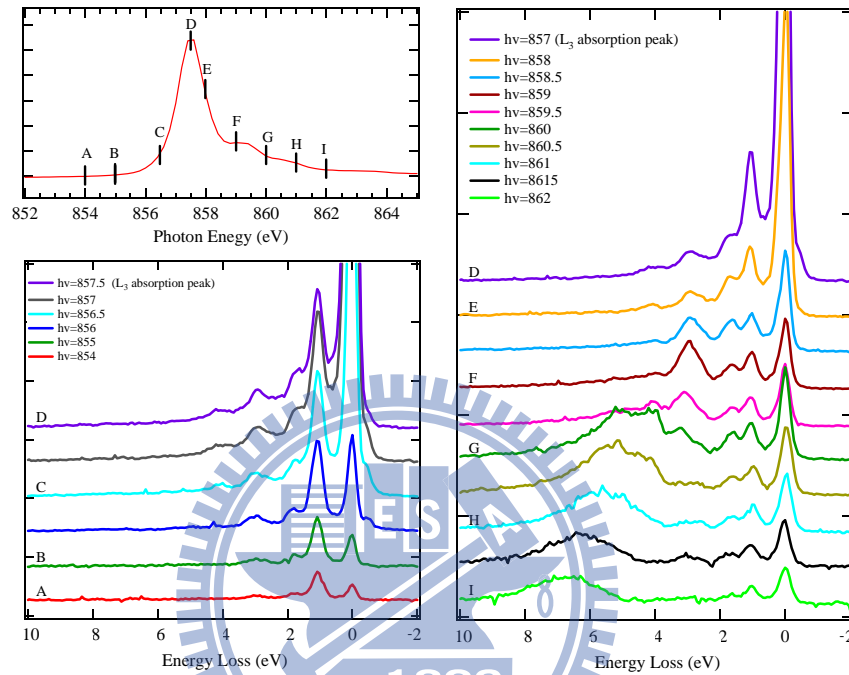
Figure 3.17: A series of energy-dependent RIXS spectrum of NiO and XAS spectra at Ni
L_3-edge.

A set of spectra taken across the Ni L_3 ($2p_{2/3} \to 3d$) edge are shown in
Fig. 3.17. Our results agree well with those measured by Ishii *et al.,* and
Ghiringhelli *et al.,*. When the photon energy is tuned to L_3+0.5eV (which
is labelled F), five structures can be observed : the elastic peak, a main
pronounced peak at 1.1 eV (in the energy-loss scale) with a shoulder around
1.8 eV, one peak at at 3.0 eV coming with a long tail between 4 - 7 eV. The
origin of those features has been observed and well described in [31].

3.4.5   Non-Resonant Inelastic Hard X-ray Scattering

The non-resonant inelastic x-ray scattering experiments are usually perform in the hard x-ray energy range with an different optical setup illustrated as in Fig. 3.18. The optical system consists of five elements, including a high heat-load Si(111) double crystal monochromator (DCM), a collimating mirror (CM), a high-resolution channel cut, a phase retarder, and a focusing mirror (FM). The DCM allows the continuous changing of the incident energy with the beam position at the same height [32]. The collimating mirror collimates the beam in order to increase the efficiency when the high-resolution channel cut is inserted into the beam. By inserting the channel cut which working at high-order reflection the energy resolution was further increased. The phase retarder generates different polarized light. The X-rays were focussed via the focusing mirror onto the sample position. The measurements were performed with the sample placed in a vacuum chamber and the path of scattered lights were under helium atmosphere. A spherically bent silicon crystal was usually used as the analyzer. The reflected x ray were collected by a silicon pin-diode. The detector, sample and analyzer crystals form a Rowland circle geometry which is shown in the lower panel of Fig. 3.18. The NIXS experiments were carried out using inverse energy scans, i.e. we scanned the incident beam while the analyzer energy was fixed at the near-backscattering energy of the Bragg reflection of the analyzer crystal.
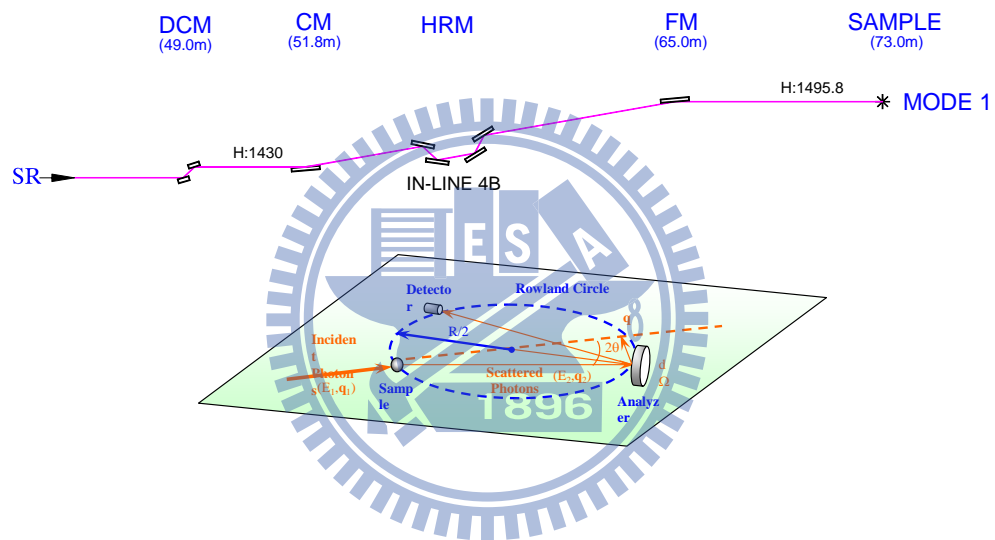
Figure 3.18: Upper panel: the optical configuration of BL12XU. Lower panel: a schematic of an inelastic x-ray scattering experiment.

Reference

[1] J. J. Sakura, *Advance Quantum Mechanics*, Addison-Wesley, London, UK, (1967), and references therein.

[2] Didier Sèbilleau, *X-ray and Electron Spectroscopies: An Introduction*, Lect. Note. Phys. **697**, 15-57 (2006).

[3] M. Blume, J. Appl. Phys. **57**, 3615 (1985), and references therein.

[4] S. Hüfner, *Photonelectron Spectroscopy*, Springer-Verlag, Berlin, Germany, (1996).

[5] F. de Groot, Chem. Rev. **101**, 1779 (2001).

[6] J. Stöhr, *NEXAFS spectroscopy*, Springer-Verlag, Berlin, Germany, (1992).

[7] M. Altarelli, *Resonant X-ray Svattering: A Theoretical Introduction*, Lect. Notes Phys. **697**. 201-242 (2006), and references therein.

[8] J. P. Hannon, G. T. Trammell, M. Blume, and D. Gibbs, Phys. Rev. Lett. **61**, 1245 (1988).

[9] A. Kotani and S. Shin, Review of Modern Phys. **73**, 203 (2001), and references therein.

[10] Luuk J. P. Ament, Michel van Veenendaal, Thomas P. Devereaux, John P. Hill, and Jeroen vam den Brink. (unpublished), and references therein.

[11] H. A. Kramers and W. Heisenberg, Z. Phys. **31**, 681 (1925)

[12] See for example W. Schülke in *Handbook on Synchrotron Radiaion*, Vol. 3, edtited by G. Brown and D. E. Moncton, North Holland, Amsterdam, (1991), and references therein.

[13] D. Gibbs, D. R. Harshman, E. D. Isaacs, D. B. McWhan, D. Mills and C. Vettier, Phys. Rev. Lett. **61**, 1241 (1988).

[14] S. B. Wilkins, P. D. Hatten, M. D. Roper, D. Prabhakaran, A. T. Boothroyd, Phys. Rev. Lett. **90**, 187201 (2003).

[15] N. Stojić, N. Binggeli, M. Altarelli, Phys. Rev. B **72**, 104108 (2005).

[16] S. B. Wilkins, N. Stojić,T. A. W. Beale, N. Binggeli,C. W. M. Castleton, P. Bencok, D. Prabhakaran,P. D. Hatten, and M. Altarelli, Phys. Rev. Lett. **71**, 245102 (2005).

[17] U. Staub, V. Scagnoli, A. M. Mulders, K. Katsumata, Z. Honda, H. Grimmer, M. Horisberger, and J. M. Tonnerre, Phys. Rev. B **71**, 214421 (2005).

[18] J. Okamoto, D. J. Huang, C.-Y. Mou, K. S. Chao, H.-J. Lin, S. Park, S-W. Cheong, and C. T. Chen, Phys. Rev. Lett. **98**, 157202 (2007).

[19] G. Ghirghelli, N. B. Brookes, E. Annese, H. Berfer, C. Dallera, M. Grioni, L. Perferri, A. Tagliaferri, and L. Braicovich, Phys. Rev. Lett. **92**, 117406 (2004).

[20] G. Ghiringhelli, M Matsubara, C. Dallera, F. Fracassi, R. Gusmeroli, A. Piazzalunga, A. Tagliaferri, N. B. Brookes, A. Kotani and L. Braicovich, J. Phys.: Condens. Matter **17**, 5397 (2005).

[21] L. Van Hove, phys. Rev. **95**, 249 (1954).

[22] J. Nordgren, J. Electron Spectrosc. Relat. Phenom. **110-111**, ix (2000), and references therein.

[23] H. S. Fung, C. T. Chen, L. J. Huang, C. H. Chang, S. C. Chung, D, J, Wang, T. C. Tseng and K. L. Tsang, Synchritrin Radiation Instrumentation **CP705**, 655 (2003).

[24] C. T. Chen, Nucl. Instrum. Methods Phys. Res. A **256**, 595 (1987).

[25] C. T. Chen *et* al., unpublished.

[26] T. C. Tseng, D. J. Wang, S. Y. Perng, C. T. Chen, C. K. Kuan, and S. H. Chang, MEDSI 02, APS, USA, 97 (2002).

[27] T. C. Tseng, D. J. Wang, S. Y. Perng, C. K. Kuan, J. R. Lin, S. H. Chang and C. T. Chen, J. Synchrotron. Rad. **10**, 450-454 (2003).

[28] T. C. Tseng, D. J. Wang, S. Y. Perng, and C. T. Chen, MEDSI 04, ESRF, France (2004).

[29] D. J. Wang, T. C. Tseng, S. Y. Perng, and C. T. Chen, NSRRC Active Report 2004.2005.

[30] H. Ishii, Y. Ishiwata, R. Eguchi, Y. Harada, M. Watanabe, A. Chainani, and S. Shin, J. Phys. Soc. Jpn. **70**, 1813 (2001).

[31] Hsiao-Yu Huang, Electronic Excitations of NiO and CoO Revealed by Resonant Inelastic Soft X-ray Scattering, Master thesis (2009).

[32] Y. Q. Cai, P. Chow, C. C. Chen, H. Ishii, K. L. Tsang, C. C. Kao, K. S. Liang, and C. T. Chen, AIP Conf. Proc. **705**, 340 (2004).
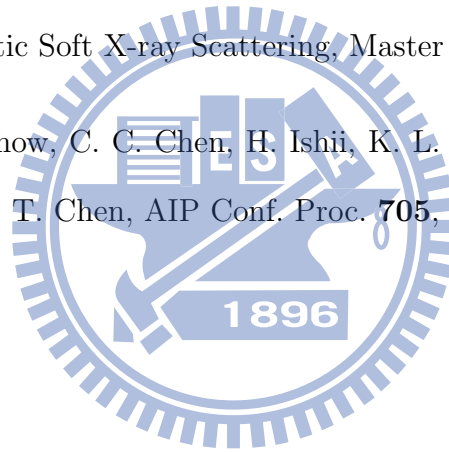
Chapter 4

Multiferroic Quantum Magnet of LiCu$_2$O$_2$

4.1 Introduction

LiCu$_2$O$_2$ has a layered orthorhombic crystal structure with the space group *Pnma*, and lattice parameters $a = 5.73$, $b = 2.86$, and $c = 12.4$ Å at room temperature. This material contains an equal number of monovalent and divalent copper ions in the crystal structure. The magnetic Cu^{2+} is located at the center of the square base of a fivefold-oxygen pyramid and forms edge-shared chains propagating along the b axis with the Cu-O-Cu bond angle of 94°; adjacent CuO$_2$ chains are connected by Li$^+$ ions forming 2D layers of Cu^{2+} which stack along the c direction with intervened layers of non-magnetic Cu$^+$ ions, as illustrated in Fig. 4.1 The distance between the magnetic nearest-neighbor Cu^{+2} ions along the double-chain is about 2.86 Å, and the distance between the next-nearest-neighbor Cu^{+2} ions is about 3.08 Å. Thus depending on the ratio of the nearest to the next-nearest-neighbor exchange coupling strength, one can consider LiCu$_2$O$_2$ as a frustrated spin

chain or an asymmetric zigzag spin ladder.
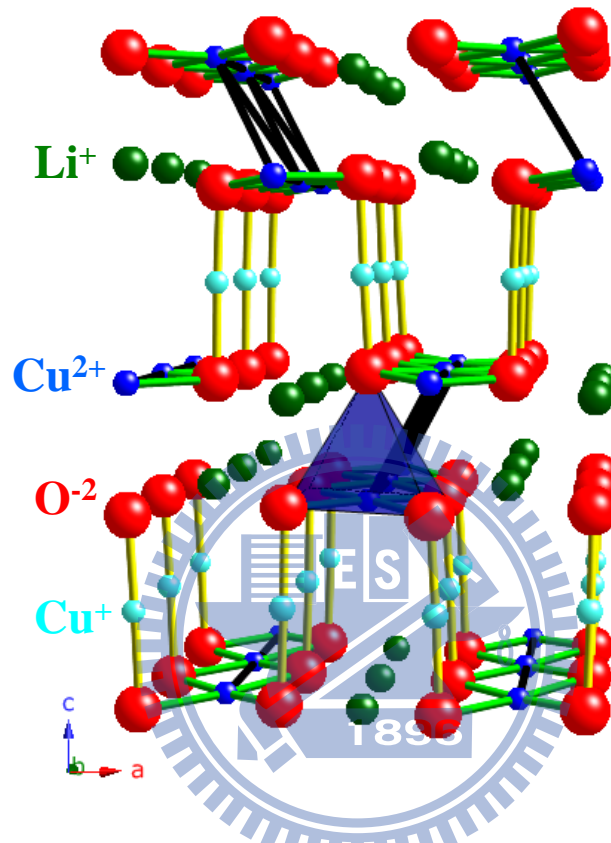
Figure 4.1: Crystal structure of $LiCu_2O_2$. The green, blue, cyan, and red balls denote Li^+, Cu^{2+}, Cu^+, and O^{2-} ions, respectively.

Several experiments evidenced that $LiCu_2O_2$ exhibits a strong competition between classical and quantum spin correlations. The edge-sharing cuprate is hence a unique and simple model system for testing theories of spin correlations in frustrated quantum magnets.

Measurements of Li nuclear magnetic resonance (NMR) revealed a clear signature of incommensurate static modulation of magnetic order below 24 K [2]. Measurement of Neutron scattering further indicated that the spin struc-
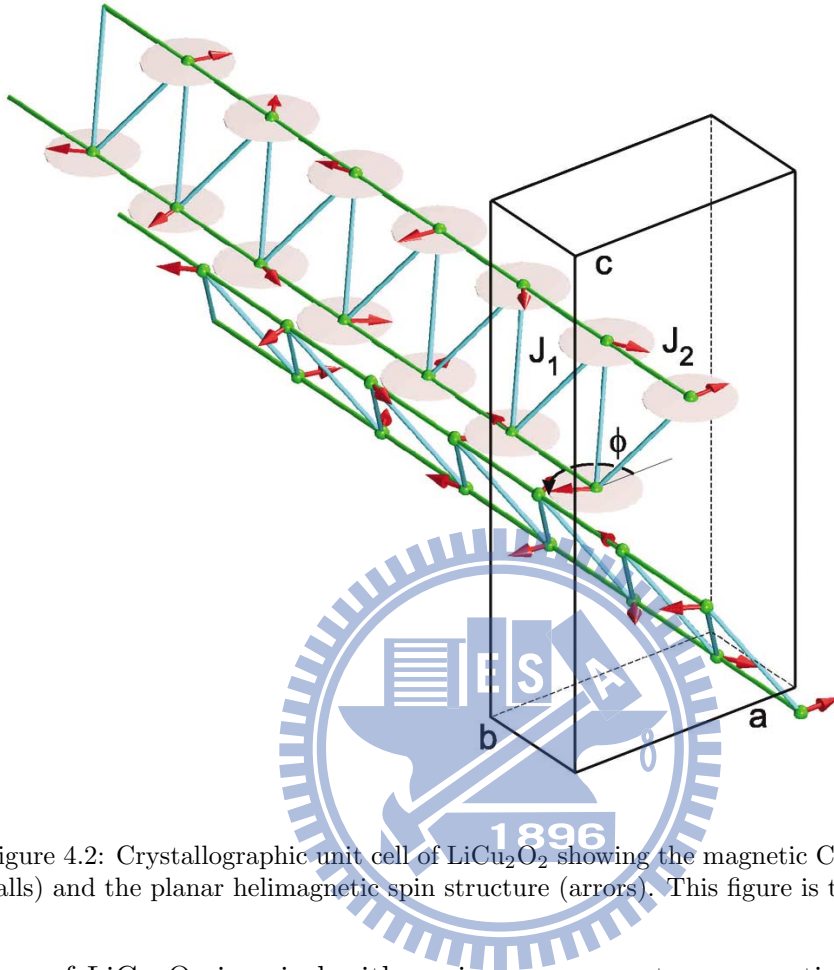
Figure 4.2: Crystallographic unit cell of $LiCu_2O_2$ showing the magnetic Cu^{2+} sites (green balls) and the planar helimagnetic spin structure (arrors). This figure is taken from [1].

ture of $LiCu_2O_2$ is spiral with an incommensurate propagation vector $\vec{q} = (1/2, \zeta, 0)$ $\zeta \sim 0.174$ at 10 K. The incommensurability parameter shows a variation as the temperature approaches T_c from low temperautre. The magnetic peak become indistinguishable from the background at $T \sim 22$ K and the moment of Cu^{2+} were found to lie in the ab plane [1]. In contrast to these signature of classical spin correlations, measurement of electron spin resonance (ESR) [3] implied that $LiCu_2O_2$ holds the characteristics of a spin liquid with an energy gap of 6 meV in the magnetic excitation spectrum. Recent ESR results also concluded that the spin moments being in the ab plane
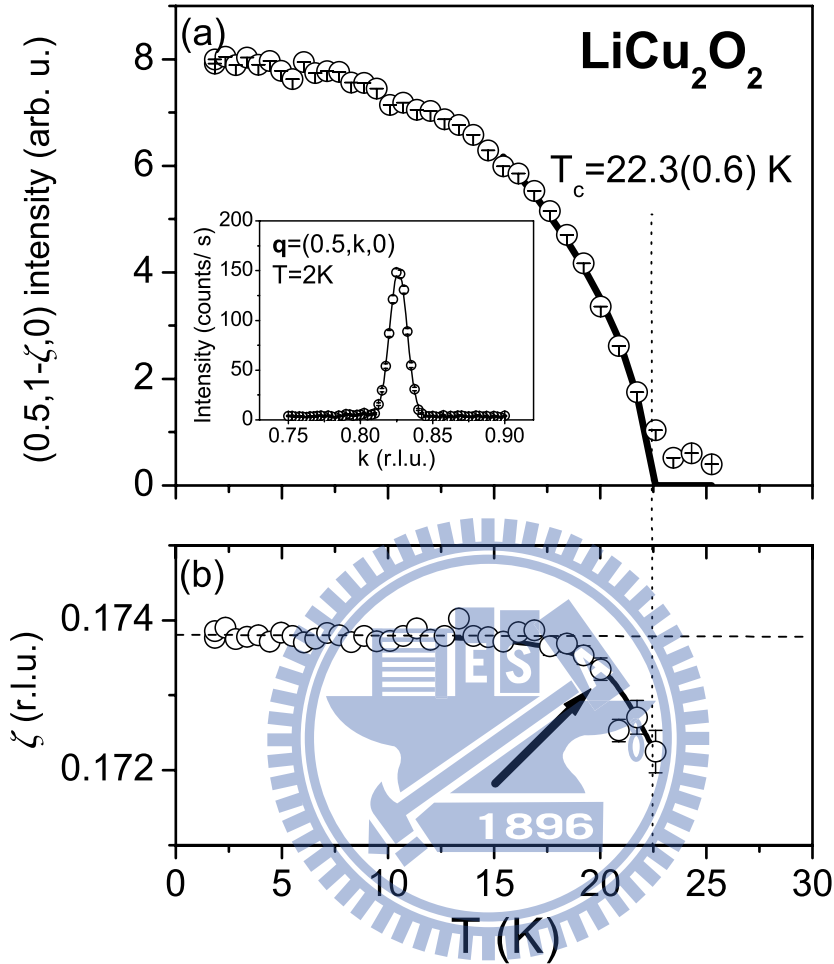
Figure 4.3: (a) Temperature dependence of the neutron scattering peak intensity of LiCu$_2$O$_2$ reported by Masuda et al.,. Inset: k scan across this reflection measured at T=2 K. (b) Measured incommensurability parameter ζ plotted as a function of temperature. These figures are reproduced from [1].

but with a larger energy gap (1.4 meV) [4]. Furthermore, measurements of polarized neutron implied the existence of large quantum fluctuation [5]. Several measurements, for example, and specific heat [1] magnetic suscepti-bility [5] and so on revealed two anomalies or a precursor transition, implying the existence two magnetic phases at low temperature.
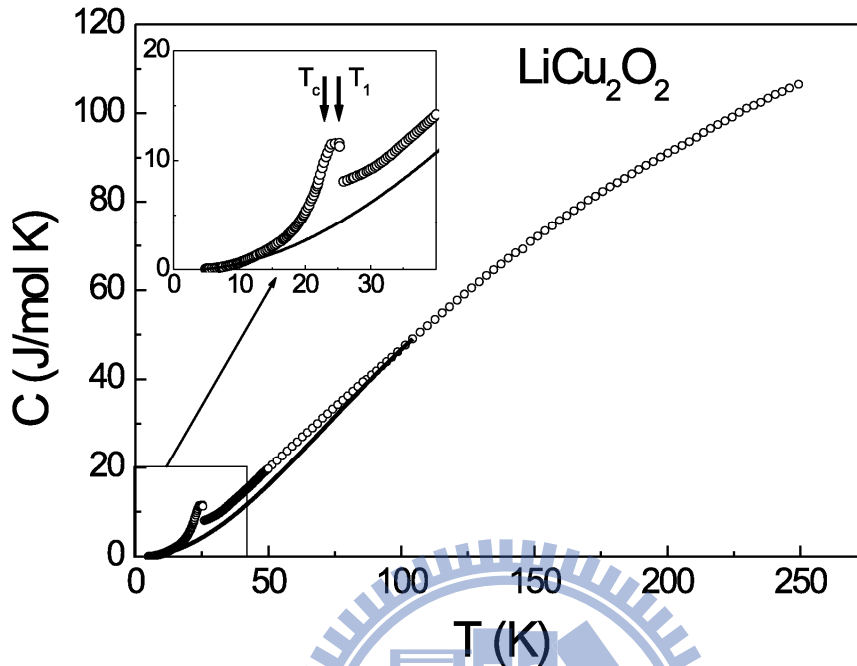
Figure 4.4: Temperature dependence of specific heat in $LiCu_2O_2$ (open symbols) reported by Masuda et al.,. The phase transition occurs $T_c \approx 22$ K with a possible precursor at $T_1 \approx 24$ K. This figure is taken from [1].

In addition to its novel magnetic properties, $LiCu_2O_2$ was discovered to be a member of multiferroics in which magnetism and ferroelectricity coexist and ferroelctric polarization can be flipped by applied external magnetic fields [5, 6]. Such multiferroicity of a quantum-spin system is understood in terms of the spin-current model [7, 8] or the inverse Dzyakishinskii-Moriya interaction [9], which have been discussed in Chapter 2.

As mentioned above, neutron results indicated that the spin-chain structure of $LiCu_2O_2$ is spiral [1]. From the spin-current model polarization $\mathbf{P}$ is induced by two neighboring spins $\mathbf{S}_i$ and $\mathbf{S}_j$ on the chain and is determined by $\mathbf{S}_i \times \mathbf{S}_j$. On the basis of the density function theory, calculations using the
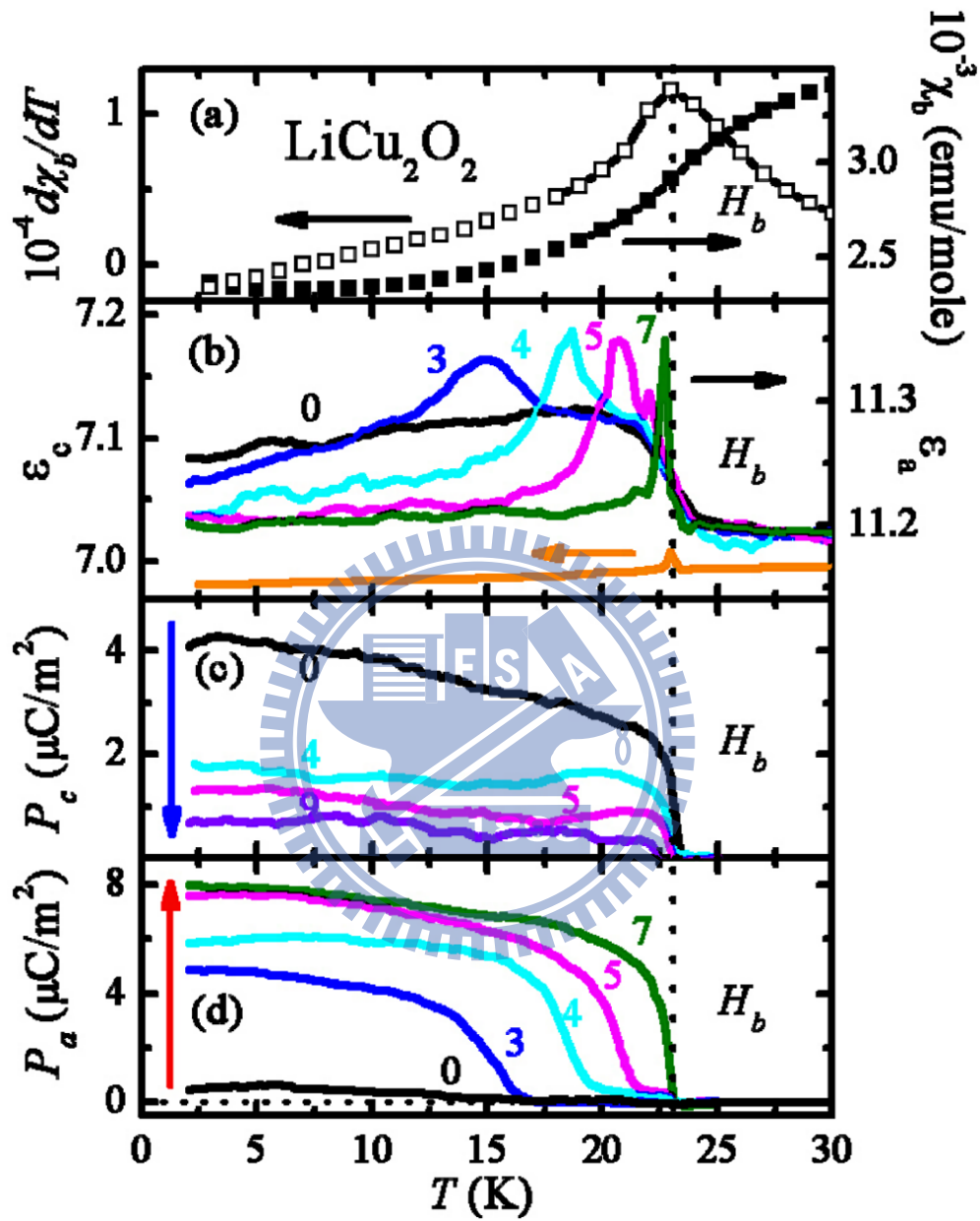
Figure 4.5: (a) Magnetic susceptibility (χ) and $d\chi/dT$ in $H_b = 2$ kOe vs temperature. (b) Dielectric constants (ε) along the a and c axes. H_b dependence of ε_a is also shown. (c) Temperature dependence of P_c and H_b. (d) Temperature dependence of P_a in H_b. This figure is taken from [6].

Berry phase method support that the spiral spins with spin-orbit coupling can induce $\mathbf{P}$ [10]. In contrast, Moskvin *et al.* argued that, in the scenario of spin current, the induced polarization due to two consecutive CuO_4 plaquettes along the chain gets cancelled exactly [11]. Based on the parity-breaking exchange interaction, they further proposed the c-axis coupling of spins are essential for the observed multiferrocity [12].
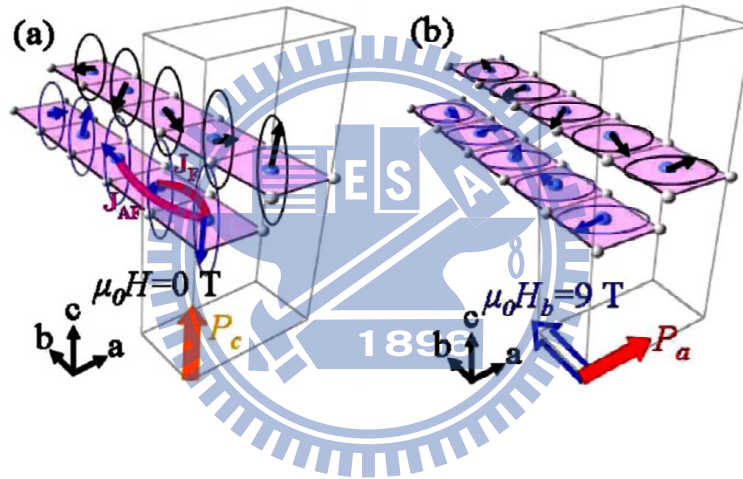
Figure 4.6: (a) Proposed spiral spin structure in zero filed. (b) Proposed spiral spin structure in H=9T. This figure is taken from [6].

Experimentally, however, conflicting results were reported regarding the magnetic structure and its relation to the observed $\mathbf{P}$ in $LiCu_2O_2$ [1, 5, 6]. For instance whether the spiral spins lie in the ab [1] or bc [6] plane remains controversial, A spontaneous electric polarization along the c axis requires spiral spins lying in the bc plane. Recent measurements of polarized neutron scattering confirmed the existence of transverse spiral (cycloidal) spin components in the bc plane and also implied the existence of large quantum

fluctuation [5]. Incidentally, there is evidence of double magnetic transition and two anomalies of magnetic susceptibility near 22 K and 24 K [1, 5, 6], but P is only observed below 22K [5]. These results imply that magnetic phase involved and their relation to the electric polarization are more complicated than those adopted in the theoretical modelling and quantum fluctuation is as well as important in $LiCu_2O_2$.

Until now, there is no consistent picture between theoretical and experimental or between different experiments. Due to its low dimensionality and spin $\frac{1}{2}$ nature, quantum fluctuations must have a profound effect on mutifferoicity [8, 13]. Therefore, there is an important issue on how the induced electric polarization by magnetism can survive out of quantum fluctuations. To address the effect of quantum fluctuation $\mathbf{P}$, it is crucial to characterize the magnetic ground state of $LiCu_2O_2$. Since any real experiment probing magnetic order is performed at a finite temperature. To reveal the zero-temperature phase, one can measure an extension of the spin-spin correlation beyond the Néel temperature (T_N). For example, the zero-temperature order of a two-dimensional (2D) quantum Heisenberg antiferromagnet spin $\frac{1}{2}$ ofextends to a finite-temperature regime known as the renormalized classical regime [14, 15], for which the fluctuations are thermal and the physical quantities behave classically with parameters being renormalized. In such a case, the spin-correlation length ξ is inversely proportional to the probability of rotating spins in the neighbors; ξ conforms to an exponential growth in inverse temperature.
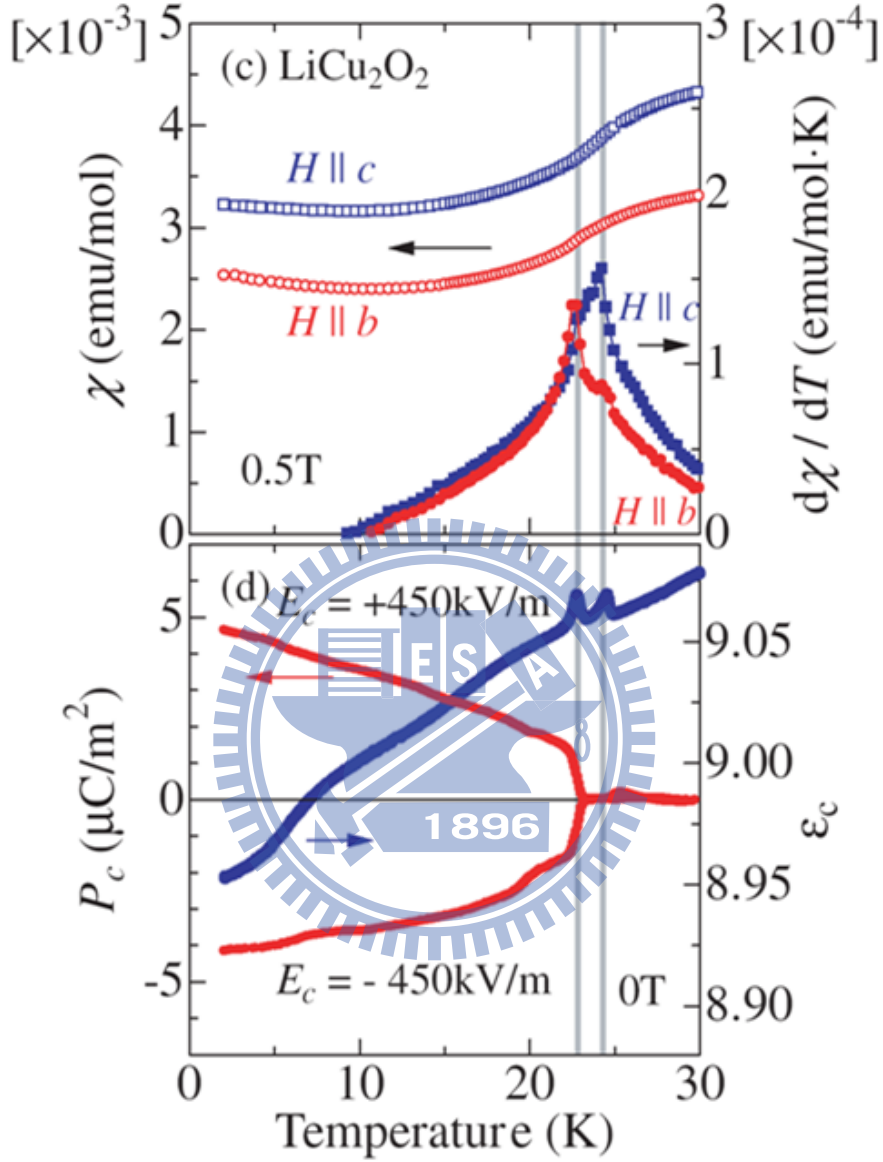
Figure 4.7: Temperature dependence of magnetic susceptibility, electric polarization and dielectric constant. For $H//c$, temperature derivative of magnetic susceptibility $(d\chi/dT)$ shows two anomalies at $T_{N1} \sim 24.5$ K and $T_{N2} \sim 23$ K and the spontaneous electric polarization parallel to the c-axis only observes below T_{N2}. These figures are taken from [5].

In this Chapter, we are going to investigate the electronic structure and magnetic ground state of quasi-1D antiferromagnetic order on $LiCu_2O_2$

by using soft X-ray techniques, including soft x-ray absorption spectroscopy, and resonant soft x-ray scattering.

4.2 Soft X-ray Absorption

We first measured soft x-ray absorption spectroscopy (XAS) on $LiCu_2O_2$ to study its orbital character of the electronic state. XAS provides information about the symmetry of the unoccupied electronic states. The absorption cross section of x-ray depends on the direction of the **E** vector with respect to the cystallographic orientations and the orbital orientation of unoccupied electronic states of transition-metal $3d$ and oxygen $2p$. XAS with linearly polarized x-ray yields a characterization of the orbital orientation of the unoccupied states [16, 17].

Single crystals of $LiCu_2O_2$ were grown with the floating zone method, and characterized with x-ray diffraction at room temperature. The polarization-dependent XAS experiment were performed at the Dragon beamline of NSRRC. The XAS measurement on crystal which was freshly cleaved in vacuum with a pressure lower than 5×10^{-10} torr at 80 K. Spectra were recorded through collecting the sample drain current with photon energy resolution 0.4 eV.The degree of the linear polarization of the incoming light was 99 %. The crystal was mounted with the c axis perpendicular to the incident electric field vector **E**. By changing the angle between the incident beam and the surface normal we recorded spectra with $\mathbf{E} \perp c$ varied to $\mathbf{E} \parallel c$.

Polarization-dependent Cu $L-$edge spectra are shown in Fig. 4.8. In

L-edge the dominant photon-excited transitions are $2p \rightarrow 3d$. Figure 4.8 displays a systematically evolution of XAS with the incident electric field vector **E** changing from parallel to nearly perpendicular to the c axis. Two main peaks marked as A_1 and A_2 can be observed in the energy range of 931-939 eV which correspond to the L_3-edge absorption. The ground state of the Cu^{2+} is a hybridization of $3d^9$ and $3d^{10}\underline{L}$, where $\underline{L}$ represent a hole in the O $2p$ valence band, i.e., the $2p$ ligaind hole.The sharp peak labeled as A_1 centered at photon energy 932.6 eV arises from the $2p^63d^9 \rightarrow 2p^53d^{10}$ transition of Cu^{2+}, such as that of Cu^{2+} in CuO [18, 19, 20]. The effective screening by the core-hole potential in the XAS final state gives rise to observed sharp resonance of A_1. On the contrary, A_2 stands out in the XAS geometry colsed to **E**$\parallel c$ axis at an energy almost identical to that of Cu^+ in Cu_2O which exhibits a combination of $3d^{10}$, $3d^94s^1$, and $3d^{10}4s^1\underline{L}$ in the ground state [20, 21, 22]. Such a broad feature of A_2 originates form a d^9-like ground state. A weak feature appears at 939.2 eV denoted as A_3, arises form the $3d^{10}\underline{L}$ configuration in the ground state, which has the in-plane bonding state [23, 24].

When the absorption geometry changes from **E** $\perp c$ nearly **E**$//c$, the intensity of A_1 decreases, whereas the A_2 peak is enhanced dramatically, and the A_3 peak gradually decreases. These results imply that the unoccupied $3d$ state of Cu^{2+} has an in-plane orbital polarization. In other words, the evolution of A_1 reflecs the in-plane character of the unoccupied $3d_{xy}$ orbital of Cu^{2+} in the CuO_4 plaquettes running along the b axis. The feature of
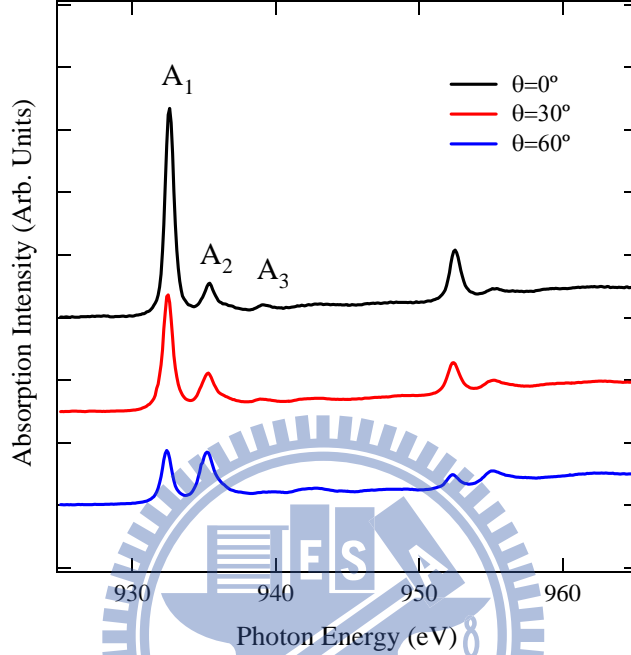
Figure 4.8: The polarization-dependent XAS spectra of Cu L-edge from $LiCu_2O_2$. θ indicates the angle between the surface normal and the incident beam.

A_2 indicates the Cu^+ hole has a dominant z character of the d^9-like ground state. However, A_2 remains non-vanish in the normal incidence ($\mathbf{E} \perp c$) suggests a XAS final state of $2p^53d^{10}4s^1$. These spectra therefore reveal that the observed peak A_2 consist of two transitions which reach the XAS final state of Cu^+. First, there occurs a transition of $2p^63d^94s^1 \rightarrow 2p^53d^{10}4s^1$ involved with a $3d_{3z^2-r^2}$ hole in the ground state. The other is the $2p^63d^{10} \rightarrow 2p^53d^{10}4s^1$ transition in which the XAS intensity is independent of the orientation of $\mathbf{E}$ because of the isotropic nature of the $4s$ state. The existence of $3d$ holes with z characteristic on the Cu^+ site may play an important role

for the interlayer magnetic coupling.
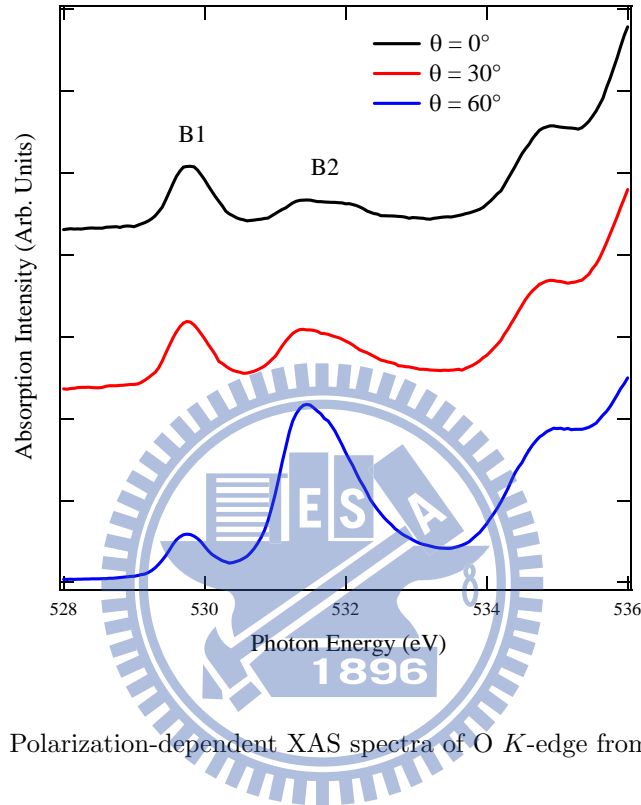
Figure 4.9: Polarization-dependent XAS spectra of O K-edge from LiCu$_2$O$_2$.

Figure 4.9 shows the polarization dependence of the O-K XAS. Due to the strong hybridization between the O $2p$ and Cu $3d$, the threshold structure observed near the O K-edge XAS gives the information of Cu $3d$. With the increase of θ the intensity of the lowest-energy absorption marked as B$_1$ decreases and the peak 2 eV above labelled as B$_2$ is enhanced. Such a evolution is also observed in the Cu L-edge XAS. Thus we suggest that peak B$_1$ is the contribution of the unoccupied O $2p$ hybridized with $3d$ states of xy symmetry on Cu^{2+} which form the upper Hubbard band (UHB). On the

other hand, B_2 is from the hybridization between unoccupied O $2p$ and Cu^+ $3d$ in which the ground state is a combination of $3d^{10}$ and $3d^9 4s^1$. The finding of Cu^+ exist $3d_{3z^2-r^2}$ hole above the Fermi level indicates that the $3d$ holes of Cu^+ could enhance the magnetic coupling between double layers of Cu^{2+} along the c direction.

In summery, we study the symmetry of the $3d$ holes of the edge-sharing low-dimensional quantum spin chain $LiCu_2O_2$. XAS results show that $3d$ holes exist not only on the Cu^{2+} sites with $3d^9$ electronic configuration but also on the Cu^+ sites which bridge layers of CuO_4 plaquettes. In the unoccupied states the nominal Cu^{2+} exhibits predominantly $3d_{xy}$ symmetry and the Cu^+ site exist $3d_{3z^2-r^2}$ holes.

4.3 *dd* **excitations**

Figure 4.10 displays the RIXS results of $LiCu2O_2$ at the Cu L_3 edge, labels A-F correspond to the excitation energies as marked in the XAS spectrum (a). The surface normal is [001] with a/b axis in the scattering plane the; angle between surface normal and the incident beam is $45°$. The polarization vector of incident beam is either parallel (π polarization) or perpendicular (σ polarization) to the scattering-plane. With σ polarization we detected the in-plane electronic structure and with π polarization we obtained information about electronic structure from both in-plane and out-plane. The details of the polarization dependence L-edge absorption have been well described in last section. The feature at around 1.78 eV can be assigned as a *dd*

excitation. This feature become stronger when the incident energy approach the maximin of Cu^{2+} transition and then gradually weakens as the energy increased. The polarization dependent *dd* excitation peak has the same tendency as absorption spectra, i.e., in-plane polarization (σ - polarization) has stronger *dd* excitation signal. In the out-of-plane polarized experiment, the strength of the *dd* excitation feature decreases due to the Cu^{2+} having the in-plane hole. The absence of two components but clear asymmetric *dd* excitation peaks indicate a weaker distortion in this compound. As the energy tune to the Cu^{+} transition, two possible absorption transition occurs, one is $2p^6 3d^9 4s^1 \rightarrow 2p^5 3d^{10} 4s^1$ the other $2p^6 3d^{10} \rightarrow 2p^5 3d^{10} 4s^1$. For $2p^6 3d^9 4s^1 \rightarrow 2p^5 3d^{10} 4s^1$ the relax state could be $2p^5 3d^{9*} 4s^1$ or $2p^6 3d^{10}$, the former one is the elastic scattering and the letter one can be consider as a charge fluctuation. For the other transition, the relaxation state could be either $2p^6 3d^{10}$ or $2p^6 3d^9 4s^1$. again one corresponding to the elastic scattering the other is the charge fluctuation. Thus we conclude that there is no *dd* excitation as the incident photon tuned to Cu^{+} transition. With the increasing of the incident energy, the center of mass of charge transfer peak continuously shifts to higher energy transfers finally mixed with the normal florescence signal. The different feature of the charge-transfer peak in polarization dependent measurement may primarily due to the large Cu^{+}-O distance along the *c* direction.
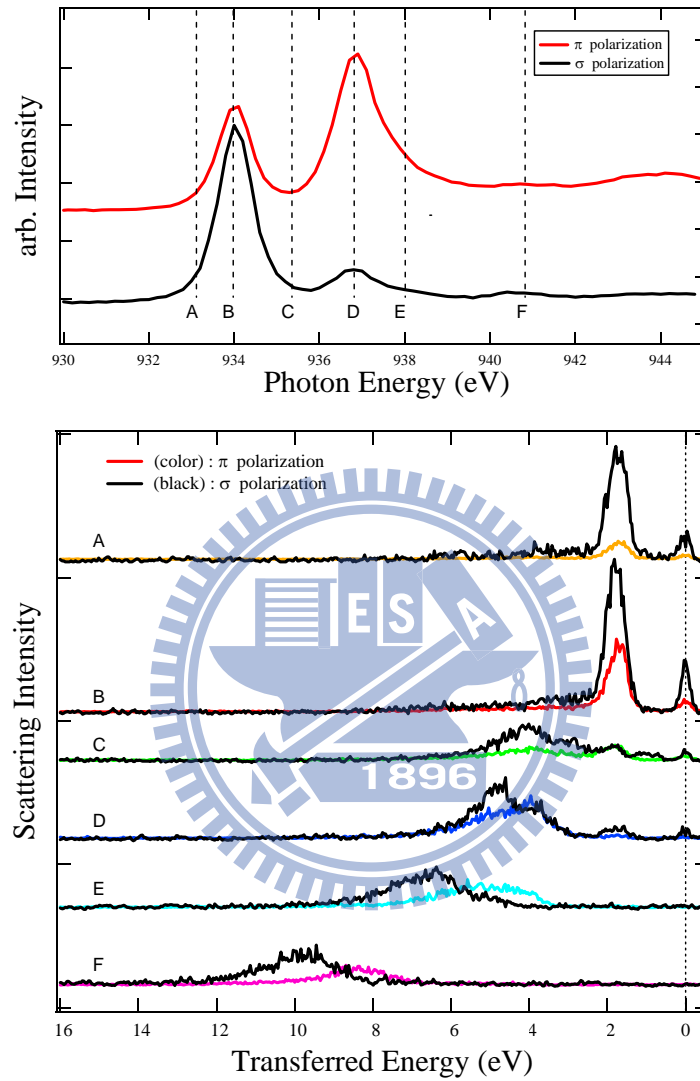
Figure 4.10: Top panel: XAS spectrum at Cu L_3-edge of LiCu$_2$O$_2$ with vertical dashed line indicating the excitation energies in RIXS. Bottom panel : The corresponding RIXS spectra. Black and color lines represent the linear polarization of incident x-rays normal to and in the scattering plane.

4.4   Multiferroic Transitions

We also measured resonant soft x-ray magnetic scattering on $LiCu_2O_2$ with the elliptically-polarized undulator beamline of the NSRRC, Taiwan. It has been proved that resonant soft x-ray magnetic scattering is an effective tool to probe the magnetic order of transition metals [25, 26, 27, 28, 29, 30] Our crystals were found to be twined with mixing of the a- and b-axis domains as observed in the literature [1, 5, 6], x-ray scattering measurements select domains of a well-defined crystallographic orientation. We prepare two samples one was cut to have a twined (100)/(010) surface for scattering measurements, the other is cleaved $LiCu_2O_2$ crystal, of which the surface quality is superior to that of a crystal with a twinned (100)/(010) surface.

Surface Normal
[100]/[010]

Surface Normal
[001]

1mm
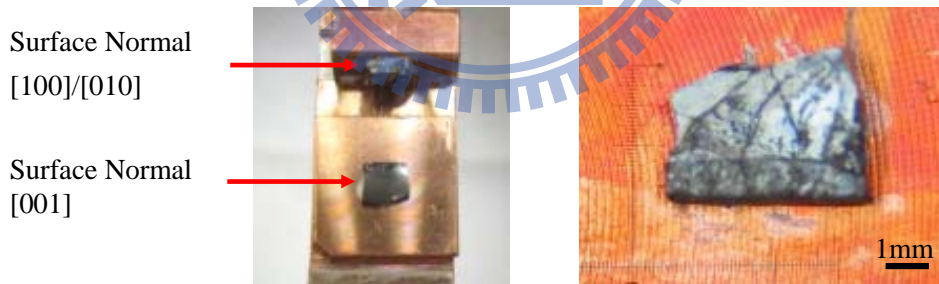
Figure 4.11: Picture of two LiCu2O$_2$ samples.

To understand the magnetic order of $LiCu_2O_2$, we first set the photon energy $\hbar w$ corresponding to the $2p_{3/2} \rightarrow 3d$ transition Cu^{2+} and measured the scattering intensity through momentum scans, i.e., the q scans, with

momentum transfer $\vec{q}$ along the [100] and [010] directions. The data were recorded at the sample temperature of 10 K with the polarization vector $\mathbf{E}$ in the scattering plane. The scattering intensity maximizes at $\vec{q} = (1/2, 0.174,0)$ in reciprocal lattice units. Note that only domain with the a axis normal to the crystal surface contribute to the x-ray magnetic scattering of such $\vec{q}$; our scattering measurements thus probe $LiCu_2O_2$ of a well defined crystallographic orientation, although the crystal is twined. The data indicate that the magnetic order of $LiCu_2O_2$ is incommensuretate with its lattice and the modulation vector is (1/2, 0.174, 0) at 10 K.

In addition to XAS, Fig. 4.12 shows the photon-energy dependence of scattering intensity $I(q, \hbar w)$ with the momentum transfer fixed at $\vec{q} = (1/2, 0.174,0)$. In the XAS measurement, the angle between incident beam and the surface normal is 30°. All data we detected by a homemade detector composed of a an electron multiplier and a CsI photon-to-electron convertor. The measured peaks of $I(q, \hbar w)$ appear to be shifted from those of XAS by an energy between 0.5 and 1.9 eV. In fact, there exists a self-absorption effect. One needs to correct the measured scattering intensity $I(q, \hbar w)$ for self-absorption; it is proportional to the scattering cross section multiplied by an x-ray absorption correction $A(q, \hbar w)$, i.e., $I(q, \hbar w) \propto |f_{mag}^{res}|^2 A(q, \hbar w)$. For a single crystal, $A(q, \hbar w)$ is proportion to the inverse of absorption coefficient μ [31]. The energy scan of magnetic scattering after such correction is also depicted in Fig 4.12. Clearly, the scattering intensity of the energy corresponding to XAS peaks of Cu^+ is much weaker than that corresponding
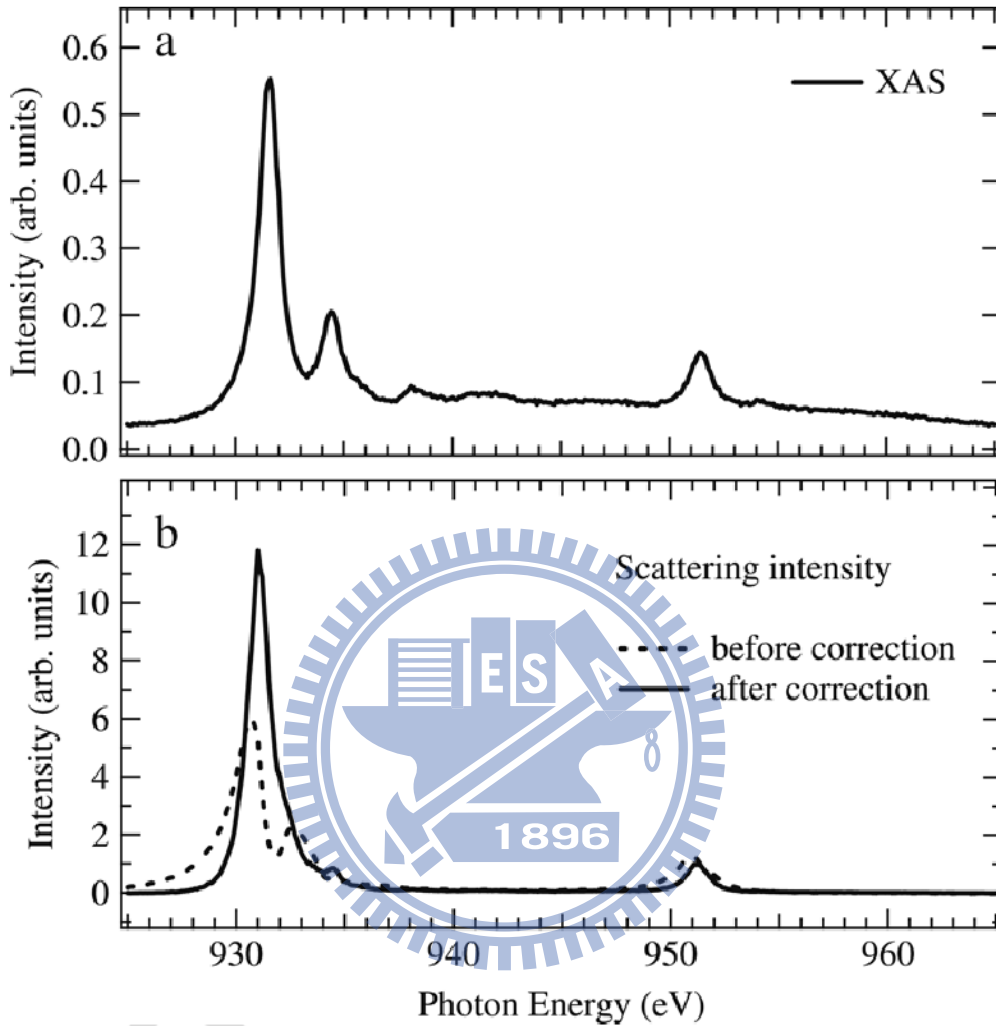
Figure 4.12: Energy-dependent spectra of (a) x-ray absorption and (b) scattering of $LiCu_2O_2$ around Cu $L_{2,3}$-edges. The absorption spectrum was obtained from the fluorescence-yield method; the scattering spectra were recorded by fixing the momentum transfer to be (0.5, 0.174, 0). Dashed and solid lines in (b) are scattering spectra before and after correction for self-absorption, respectively. The correction method is described in the text. All spectra were measured at 10 K.

to those of Cu^{2+} consistent with the expectation that magnetic moment of

Cu^+ is negligible because of the $3d^{10}$ configurations.

NMR and neutron measurements indicate that the Néel temperature T_N

of the spiral magnetic order in $LiCu_2O_2$ is between 22 and 24 K. Figure 4.13
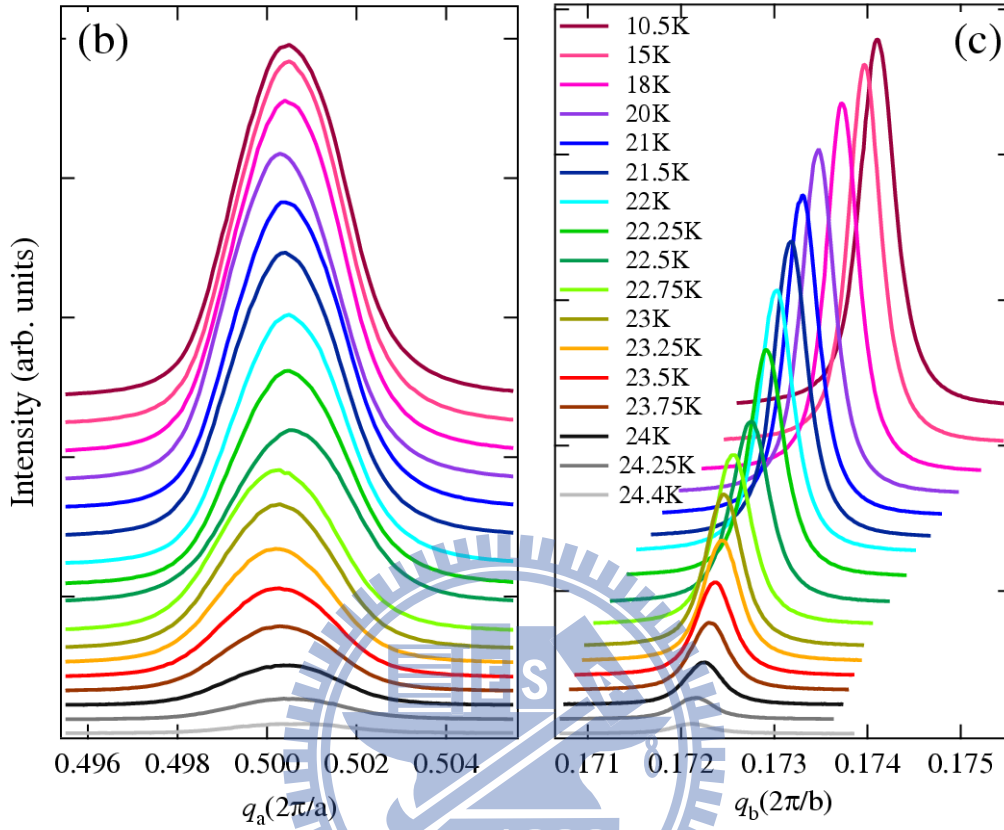
Figure 4.13: Momentum scans of resonant soft X-ray scattering of LiCu$_2$O$_2$ along the [100] and [010] directions at various temperatures below 25 K. The incident photon energy was set at 930 eV. q_a and q_b are the components of momentum transfer in the ab plane, i.e., $\mathbf{q} = (q_a, q_b, 0)$. All q_a scans were recorded with q_b fixed at the maximum of scattering intensity, and vice versa.

shows q scans along the [100] and [010] directions at various temperature below 25 K. To reduce the self-absorption effect, the incident photon energy was set at 930 eV. The q scans were fitted to a Lorentzian function with a linear background to determine the peak position and the half-width at half maxima (HWHM). We define the spin-spin correlation length as the inverse of HWHM, i.e., $\xi \equiv 1/$HWHM. The spin-correlation length ξ_b along b axis is 2110 Å. The observed in-plan correlation length ξ_a along the a axis direction

is notable large, ~ 690 Å. The observed correlation length along the spin chain is substantially larger than the inverse of HWHM in neutron measurements, because the width of q scan in neutron scattering is often limited by instrumental resolution. The ratio ξ_a/ξ_a is comparable with the ratio of the inter-chain exchange interaction to the nearest-neighbor coupling obtained from neutron measurements [1]. Because the inter-chain interactions of 1D spin-chain materials tend to suppress quantum spin fluctuations and restore semicalssical behavior, our observation of substantial inter-chain coupling explains why $LiCu_2O_2$ exhibits a classical-like magnetic feature of long-range incommensurate order, although it is a system of a quantum spin chain. Hence, $LiCu_2O_2$ has a 2D-like magnetic order in ab plane. One therefore can examine the magnetic properties at zero temperature through measuring the sort-range spin correlation above T_N.

As the temperature increases, the peak position in the q scan along the [100] direction remains unchanged, while that along the [010] move toward a smaller value. That is, the modulation vector is $(1/2, \zeta, 0)$ with ζ being 0.174 at 10 K, and starts to decrease and departure away from 0.174 when the temperature goes above 17 K. These results are consistent with that observed by neutron scattering [1]. In the classical regime, if $|J_2/J_1|$ is greater than 1/4, the propagation vectors is $\cos^{-1}(J_1/4J_2)$ in the the units of the reciprocal lattice constant and the pitch angle of spin spirals is $2\pi\zeta$. The measurement of $\zeta=0.174$ indicates that the pitch angle is 62.6° and $J_1/J_2 = 0.184$ at 10 K. The measure ratio J_1/J_2 is consistent with the results of inelastic neutron
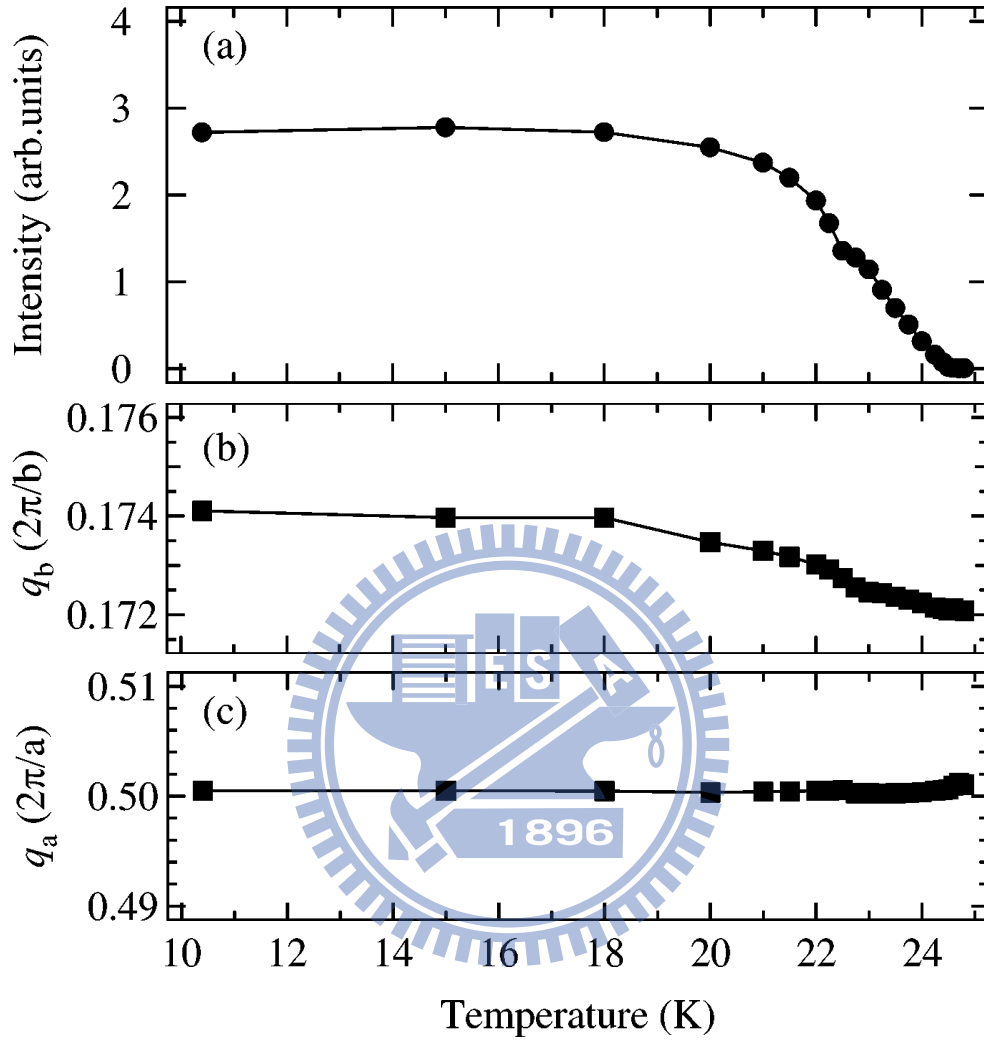
Figure 4.14: Temperature-dependent scattering intensity and components of momentum transfer deduced of data shown in Fig. 4.13. The scattering intensity plotted in (a) is the peak area of momentum scans; the components of momentum transfer q_a and q_b plotted in (b) and (c) are obtained from fitting momentum scans to a Lorentzian function with a linear background.

scattering [32] and LSDA+U claculation [33] calculation. The temperature dependence of ζ suggests that there is a competition between the nearest- and the next-nearest-neighbor exchange interaction J_1 and J_2. The change in modulation vector implies that such competition leads to an increase of

J_1/J_2 as the temperature approaches to the transition temperature, resulting in a decrease in the pitch angle of spin spirals. In addition, Fig. 4.14 depicts the temperature-dependent scattering intensity and the components q_a and q_b of the modulation vector. The decrease of scattering intensity with the increase of the temperature suggests that the onset temperature of magnetic order is about 24.5 K. Above this temperature, the long-range magnetic order collapses because thermal fluctuation overcomes the interlay coupling.

Figure 4.15: Illustration of the scattering geometry.

To achieve a measurement of the short-range spin correlation, we used a cleaved LiCu$_2$O$_2$ (001) crystal, of which the surface quality is superior to that of to a crystal with a twinned (100)/(010) surface, although XRD results indicate both crystals have comparable qualities bulk structure. Because our UHV scattering setup is a two-circle diffractometer, the (001) crystal surface limits our scattering measurements to modulation vectors expressed in the terms of $(\vec{q}_{ab}, q_c)$, in which $\vec{q}_{ab}$ and q_c are projections of $\vec{q}$ onto the ab plane and the c axis, respectively. The scattering geometry is illustrated in the
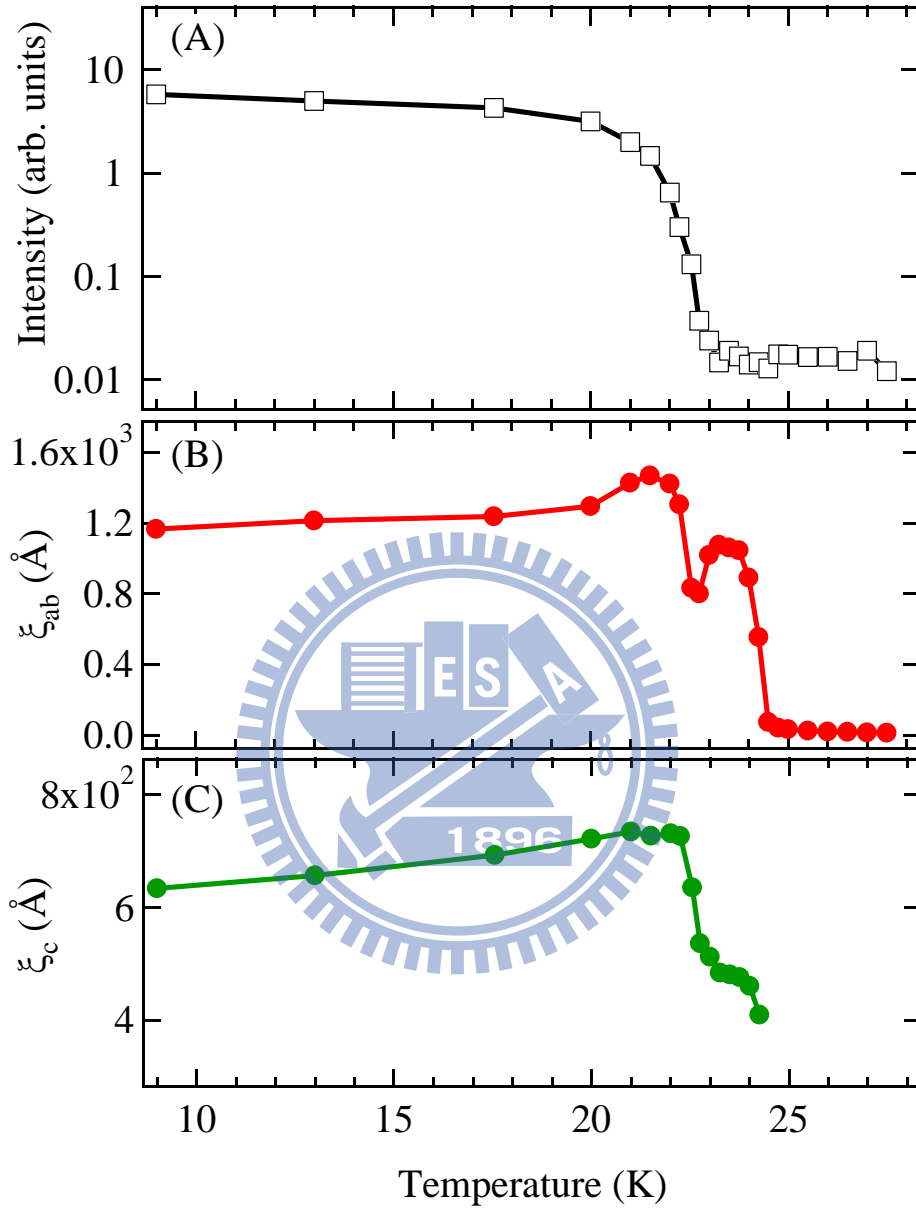
Figure 4.16: Temperature-dependent of resonant soft x-ray scattering on cleaved LiCu$_2$O$_2$ (001) with $\vec{q} = (0.5 \ q_b, \ q)$ and $q_b \sim 0.174$. The scattering intensity (a) and the correlation length ξ_c and ξ_{ab} defined as the inverse of HWHM q_c and q_{ab} scans are shown in (b) and (c), respectively.

Fig. 4.15. The scattering plane is defined by incoming beam and outgoing beam. Surface normal is (001) which layies in the scattering plane and the

a axis is at an angle ϕ off the scattering plane by $\sim 34.8°$, depending upon temperature.

Figure 4.16 plots the temperature dependence of scattering intensity and correlation lengths. The spin correlations along $\vec{q}_{ab}$ and the c axis are, respectively, denoted as ξ_{ab} and ξ_c. Our data indicate that both ξ_{ab} and ξ_c show two maxima at 21.4 K (T_{N1}) and 23.5 K (T_{N2}). These two transitions are consistent with two anomalies in specific heat and the temperature derivative of magnetic susceptibility [5]. As the temperature decreases across T_{N2}, the interlayer coupling starts to overcome thermal fluctuations and a short-range three-dimensional spiral order begins to develop and forms a precursor phase. With further cooling below T_{N1}, when an electric polarization is induced by spin order, a long-range order is established. That is, T_{N1} is the onset temperature of induce polarization, and T_{N2} is the transition temperature of the precursor of spin order.

Furthermore, we remarkable found that there exists a short-range order above T_{N2}. Figure 4.17 shows q_{ab} and scans q_c scans at selected temperature above T_{N1}. In addition to the modulation vector with $q_b = 0.174$ which corresponds to the correlation length showing TPW transitions as in Fig. 4.16(b), another broad component with $q_b \sim 0.172$ appears in the vicinity of T_{N2} i.e., the fitting curve 1 in Fig. 4.17(b). Fitting the $\vec{q}_{ab}$ scan with two Lorentizan components for temperature above 22.5 K, we found that the broader one does not vanish even at temperatures beyond T_{N2}. Momentum scans along the c direction reveal further that the scattering intensity dose
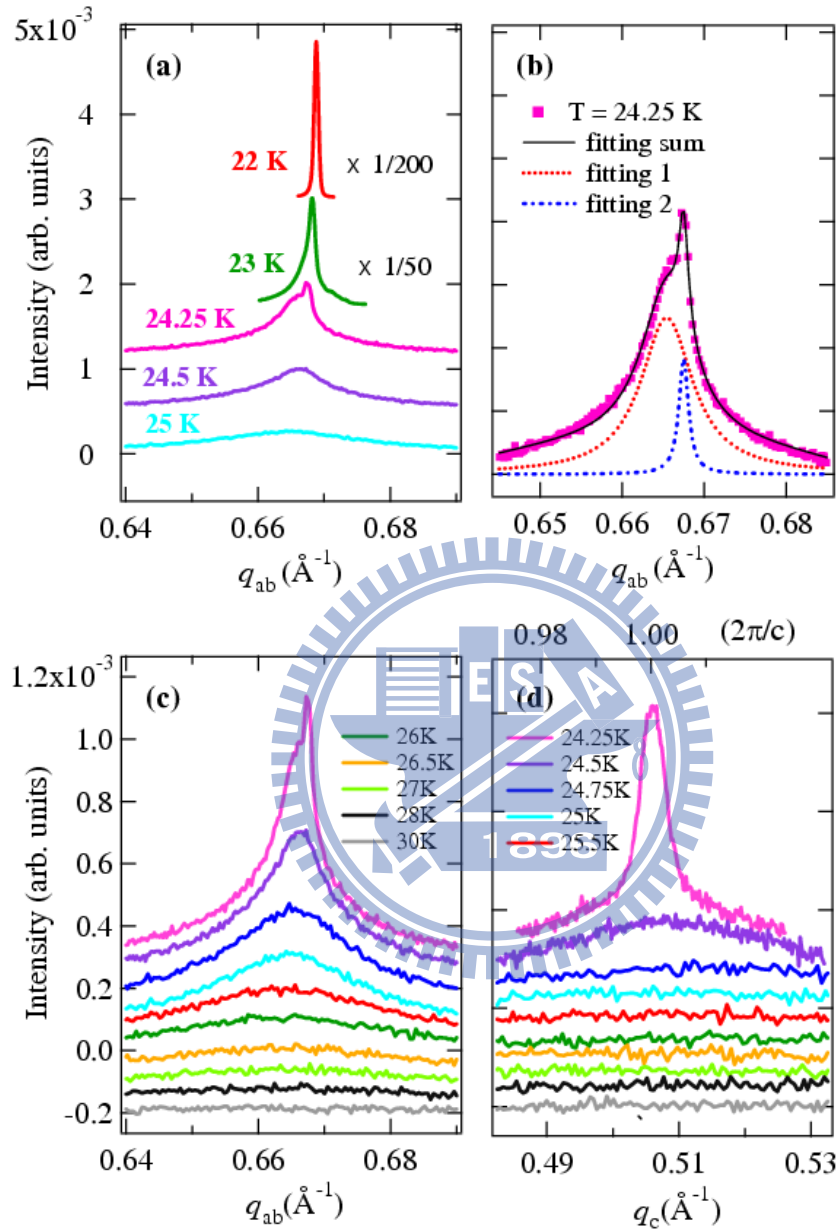
Figure 4.17: q_{ab} and q_c scans of resonant soft x-ray scattering on cleaved LiCu$_2$O$_2$ (001) at various temperatures above T_{N1} Curves 1 and 2 in (b) are Lorentzian components obtained from a nonlinear least square fitting. All curve are offset vertically for clarity.

not depend on q_c for temperatures above 24.5 K, whereas it shows a well

defined maximum in the q_{ab} scan, as plotted in Figs. 4.17(c) and (d). These

results indicates a short-range in-plane spin order above T_{N2}. Since **P** is only observed below T_{N1} [5] where the spin correlation is built in along c-axis, our our measurements imply that the spin coupling along the c-axis is essential for inducing electric polarization in $LiCu_2O_2$, corroborating the proposal of Moskvin *et al.* [12].

What is the original of the short-range spin-ordering when the temperature is above the T_{N2}. Since this is a quantum spin system but have classical magnetic long-range ordering. Quantum fluctuation effects may play an important role in the observation of the short-range magnetic spin ordering which beyond the classical magnetic ordering. Chakravarty *et al.,* [14, 15] in 1980 pointed out that the long-wavelength on the two-dimensional square-lattice low-temperature behavior can be suitably describe by the quantum nonlinear sigma model. The phase diagram of the g-T plane are sketched in Fig. 4.18, g is the coupling constant. The phase diagram of this model at $T=0$ consists of two regions separated by the quantum critical point $g_c \sim 4\pi/\Lambda$, where Λ being the momentum cutoff.

For $g < g_c$ the ground state is ordered (thick line) and for $g > g_c$ the quantum disorder behavior rules this range, full rotation symmetry of the ground state is restored and the spin are in the so-called spin-liquid state. At finite temperature, there are three regions in the phase diagram. Above the quantum critical point, in the quantum critical regime, the physics is controlled only by the temperature, and the correlation length varies linearly with T. In the quantum disorder phase separated by a crossover line from

the quantum critical phase, spin have short-range correlation the ground state has an excitation gap and the correlation length stays constant as $T \rightarrow 0$. Finally, the renormalized classical regime, which originated from the
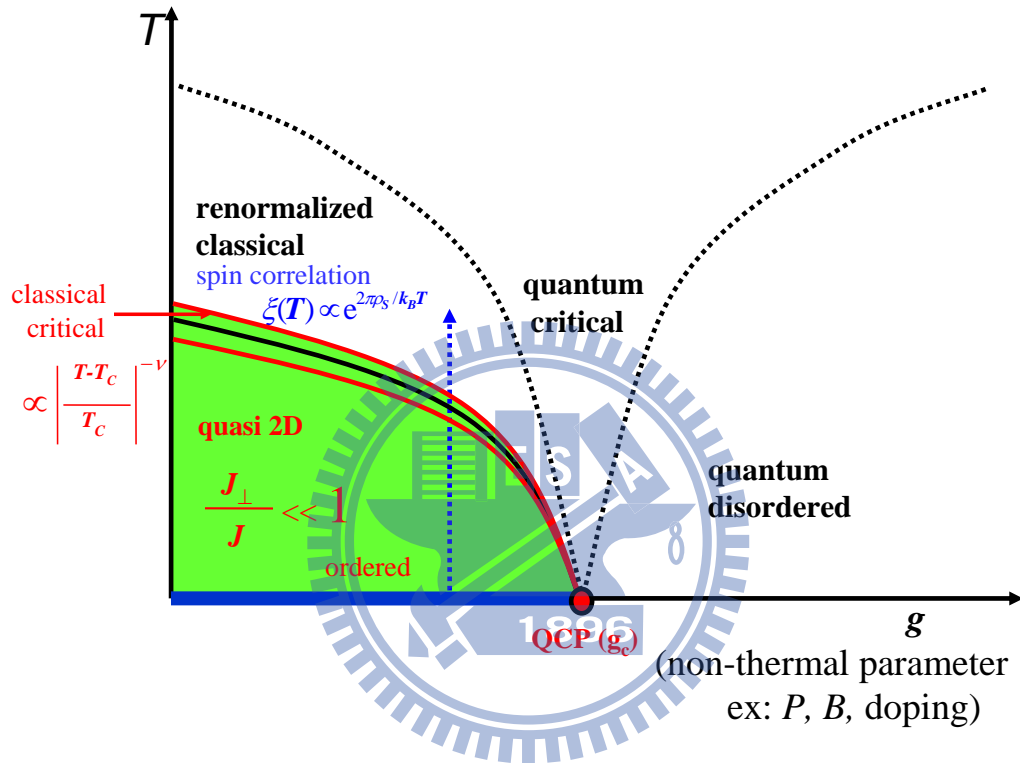
Figure 4.18: Phase diagram of a quantum sustem in a $g - T$ plane. The tick line depicts the $T = 0$ order state for $g < g_c$.

long-rang Nèel state at T=0 when thermal fluctuations are included, at finite temperature, lone-range order is lost but the spin correlation with correlation length diverges exponentially as for T $\rightarrow$ 0 [34].

To characterize the spin order in the ground state of $LiCu_2O_2$ we measured the detail temperature dependence of spin correlation length ξ_{ab} as depicted in Fig. 4.19. A plot of ξ_{ab} on a logarithmic scale versus reciprocal

temperature is nearly a straight line, indicating that ξ_{ab} exponentially with increasing temperature when T is above T_{N2}. We found that the in-plan correlation length conforms to an expression $\xi_{ab} = \xi_0 e^{2\pi\rho/k_B T}$, in which ρ and k_B are the spin stiffness and Boltzmann constant, respectively. For an average in-plane spin coupling J and ρ being $JS(S+1)$, the data of ξ_{ab} re satisfactorily fitted with this expression if J is 4.2 meV, which has the same order of magnitude as that of the nearest-neighbor coupling concluded from neutron scattering and first-principles calculations. This observed exponential decay unravels the renormalized classical nature of 2D-like spin interaction and implies that LiCu$_2$O$_2$ exhibits a long-range spin order in its ground state rather than being a gapped spin liquid.

In summary, measurements of soft x-ray magnetic scattering indicate that LiCu$_2$O$_2$ exhibits a long-range 2D-like magnetic order incommensurate with the lattice. The modulation vector of the spin spirals below the Néel temperature is (1/2, ζ_b, 0), with $\zeta_b \sim 0.174$ Such a magnetic structure is derived from the ordering of divalent Cu^{2+} ions rather than monovalent Cu$^+$. Temperature-dependent measurements suggest that the NNl temperature is about 24.5 K and the ground state is with a renormalized classical character although the system has the quantum nature of spin 1/2. In addition, the spin coupling along the c axis is found to be essential for inducing electron polarization.
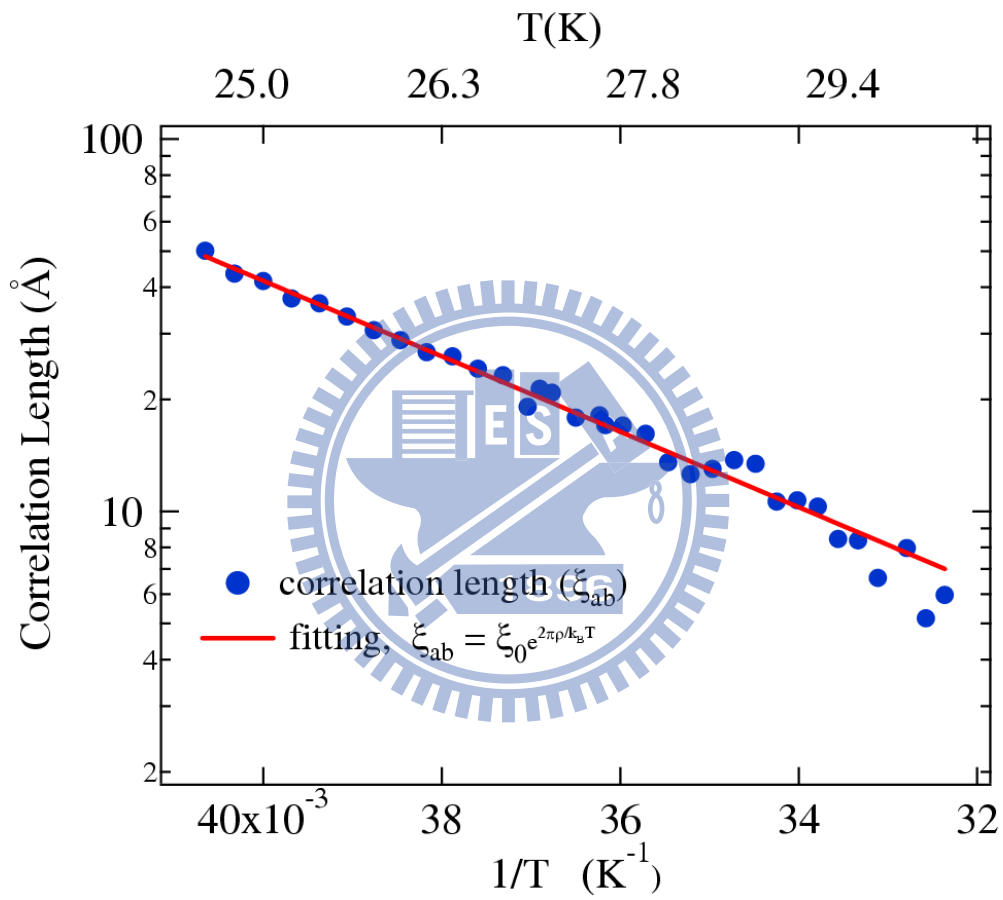
Figure 4.19: Temperature dependence of in-plane correlation length ξ_{ab} above the Néel temperature. The circles depict ξ_{ab} plotted on a logarithmic scale versus reciprocal temperature. The data are fitted with an expression $\xi_0 e^{2\pi\rho/k_B T}$ explained in the text.

Reference

[1] T. Masuda, A. Zheludev, A. Bush, M. Markina, and A. Vasiliev, Phys. Rev. Lett. **92**, 177201 (2004).

[2] A. A. Gippius, E. N. Morozava, A. S. Moskvin, A. V. Zalessky, A. A. Bush, M. Baentiz, H. Roser, S.-L. Drechsler, Phys. Rev. B **40**, 020406 (2004).

[3] S. Zvyagin, G. Cao, Y. Xin, S. Macall, T. Caldwell,W. Moulton, L-C. Brunel, A. Angerhofer, J. E. Crow, Phys. Rev. B **66**, 064424 (2002).

[4] L. Mihaly, B. Dora, A. Vanyolos, H. Berger and L. Forro, Phys. Rev. Lett. **97**, 067206 (2006).

[5] S. Seki, Y. Yamasaki, M. Soda, M. Matsuura, K. Hirota, and Y. Tokura, Phys. Rev. Lett. **100**, 127201 (2008).

[6] S. Park, Y. J. Choi, C. L. Zhang and S-W. Cheong, Phys. Rev. Lett. **98**, 057601 (2007).

[7] H. Katsure, N. Nagaosa, and A. V. Balatsky, Phys. Rev. Lett. **95**, 57205 (2005).

110

[8] H. Katsura, S. Onoda, J. H. Han, and N. Nagaosa, Phys. Rev. Lett. **101**, 187207 (2008).

[9] I. A. Sergienko and E. Dagotto, Phys. Rev. B. **73**, 094434 (2006).

[10] H. J. Xiang and M.-H. Whangbo, Phys. Rev. Lett. **99**, 257(2007).

[11] A. S. Moskvin and S.-L. Drechsler, arXiv:0710.0496v1.

[12] A. S. Moskvin, Yu. D. Panov, and S.-L. Drechsler, Phys. Rev. B **79**, 104112 (2009).

[13] S. Furakawa, M. Sato, Y. Saiga, and S nmoda, arXiv : 0802,3256v2.

[14] S. Chakravarty, B. I. Halperin, and D. R. Nelson, Phys. Rev. Lett. **60**, 1057 (1988).

[15] S. Chakravarty, B. I. Halperin, and D. R. Nelson, Phys. Rev. B **39**, 2344 (1989).

[16] C. T. Chen, F. Sette, Y. Ma, M. S. Hybertsen, E. B. Stechel, W. M. C. Foulkes, M. Schluter, S-W. Cheong, A. S. Cooper, L. W. Rupp, Jr., B. Batlogg, Y. L. Soo, Z. H. Ming, A. Krol. and Y. H. Kao, Phys. Rev. Lett. **66**, 104 (1991).

[17] C. T. Chen, L. H. Tjeng, J. Kwo, H. L. Kao, P. Rudolf, F. Sette, and R. M. Fleming, Phys. Rev. Lett. **68**, 2543 (1992).

[18] J. Ghijsen, L. H. Tjeng, J. van Ele, H. Eskes, J. Westerink, G. A. Sawatzky, and M. T. Czyzyk, Phys. Rev. B. **38**, 11322 (1988).

[19] J. Ghijsen, L. H. Tjeng, H. Eskes, G. A. Sawatzky, and R. L. Johnson, Phys. Rev. B. **42**, 2268 (1990).

[20] L. H. Tjeng, C. T. Chen, and S.-W. Cheong, Phys. Rev. B **45**, 8205 (1992).

[21] M. Grioni, J. F. van Acker, M. T. Czyžyk, and J. C. Fuggle, Phys. Rev. B **45**, 3309 (1992).

[22] M. Finazzi, G. Ghiringhelli, O. Tjernberg, Ph. Ohresser, and N. B. Brookes, Phys. Rev. B **61**, 4629 (2000).

[23] H. Eskes, L. H. Tjeng, and G. A. Sawatzky, Phys. Rev. B. **41** 288, (1990).

[24] M. A. van Veememdaal and G. A. Sawatzky, Phys. Rev. B **49**, 3473 (1994).

[25] J. P. Hannon, G. T. Trammell, M. Blume, and D. Gibbs, Phys. Rev. Lett. **61**, 1245 (1988).

[26] U. Staub, V. Scagnoli, A. M. Mulders, K. Katsumata, Z. Honda, H. Grimmer, M. Horisberger, and J. M. Tonnerre, Phys. Rev. B **71**, 214421 (2005).

[27] See e.g., J. Okamoto, D. J. Huang, C.-Y. Mou, K. S. Chao, H.-J. Lin, S. Park, S-W. Cheong, and C. T. Chen, Phys. Rev. Lett. **98**, 157202 (2007), and reference therein.

[28] S. B. Wilkins, P. D. Hatten, M. D. Roper, D. Prabhakaran, A. T. Boothroyd, Phys. Rev. Lett. **90**, 187201 (2003).

[29] S. B. Wilkins, N. Stojić,T. A. W. Beale, N. Binggeli,C. W. M. Castleton, P. Bencok, D. Prabhakaran,P. D. Hatten, and M. Altarelli, Phys. Rev. Lett. **71**, 245102 (2005).

[30] N. Stojić, N. Binggeli, M. Altarelli, Phys. Rev. B **72**, 104108 (2005).

[31] H. Stragier, J. O. Cross, J. J. Rehr, L. B. Soresen, C. E. Bouldin, and J. C. Woicil, Phys Rev. Lett. **69**, 3064 (1992).

[32] T. Masuda, A. Zheludev, B. Roessli, A. Bush, M. Markina, and A. Vasiliev, Phys. Rev. Lett. **94**, 0399706 (2005).

[33] V. V. Mazurenko, S. L. Skornyakov, A. V. Kozhevnikov, F. Mila, and V. I. Anisimov, Phys. Rev. B **75**, 224408 (2007).

[34] M. Greven, R. J. Birgeneau, Y. Endoh, M. A. Kastner, B. Keimer, M. Matsuda, G. Shirane, and T. R. Thurston, Phys. Rev. Lett. **72**, 1096 (1994).

Chapter 5

X-ray Spectroscopy of Cuprate CuO

5.1 Introduction

The induced inducing ferroelectricity in multiferroics by non-collinear spin spirals with broken inversion symmetry has attracted much attention in the past few years. A breakdown of the inversion symmetry of the magnetism allows the existence of ferroelectricity. Multiferroicity of most magnets with inversion symmetry broken can explained by two scenarios. One is based on the geometric frustration as well as the competition between the magnetic interaction. The other is based on the Dzyaloshinskii-Moriya interaction. The magnetism of such magnets typically occurs at low temperatures, and the magnetically induced ferroelectricy of these multiferroics tends to exist at temperatures lower than ~ 40 K, too low to be practically useful. How to increase the magnetic and ferroelectric ordering temperature is a crucial question.

Recently, Shimizu et al., showed a plot of typical examples of magnetic

interaction strength J in cuprates with various bond angles [1]. This observation indicates that compounds with large J exhibit high a Nèel temperature; with the decrease of the bond angle ϕ, J is monotonically suppressed and eventually becomes negative (ferromagnetic) around $\phi = 95°$. As a result, the ferromagnetic J competes with high-order superexchange interactions, leading to spiral magnetic order in cuprates with small ϕ. Kimura et al., [2] demonstrated that, because of its small Cu-O-Cu bond angle, CuO has a spiral magnetic order and both magnetic order and ferroelectric order can be simultaneously stabilized at high temperature.
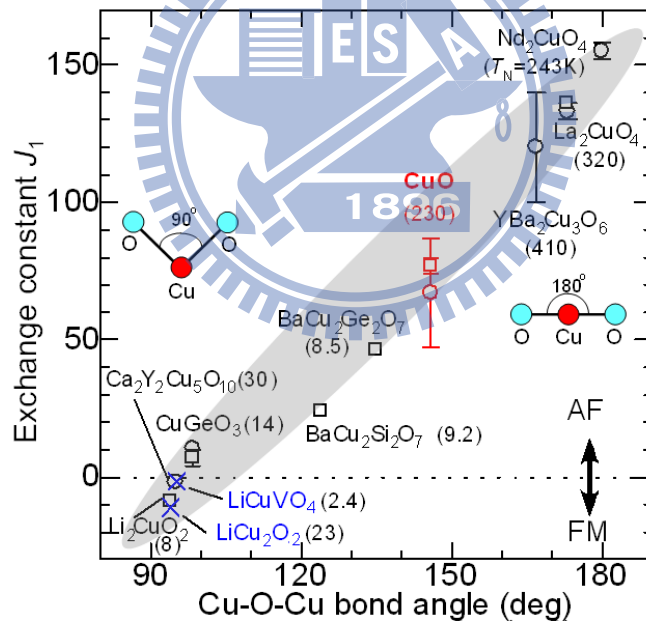
Figure 5.1: Principal superexchange interaction J as a function of Cu-O-Cu bond angle ϕ for various low-dimensional cuprates. Open circles and crosses represent the data obtained from neutron scattering. Open squares are the data obtained from susceptibility measurement. Blue crosses show ferroelectricity induced by spiral magnetic order. Figures in parentheses denote magnetic ordering temperatures of the respective compounds. The grey line is a guide to the eyes. This figure is taken from [2]

CuO is monoclinic with space group $C2/c$ which is unique among the transition-metal monoxides. The lattice parameters are a=4.68 Å, b=3.419 Å c=5.123 Å with β=99.76 ° [3]. The nearest and next nearest Cu-O bond length is 1.948 Å and 1.96 Å, each Cu atom is linked to four nearly coplanar O atoms at the corner of an almost rectangular parallelogram, forming a edge-sharing spin chain. Cu-O bonds perpendicular to the plane are 2.774Å. The parallelogram form two ribbons; one runs in the [110] direction and another in [$\bar{1}$10] direction. These ribbons stack alternately in the c direction. The local structure of CuO can be consider as an distorted octahedral with edge-sharing CuO_4 plaquettes run along [110] and [$\bar{1}$10] directions. As for the magnetic structure, CuO exhibits AFM ordering with the modulation vector along [10$\bar{1}$]. Along [10$\bar{1}$] and [101], there are two types of zigzag spin chains composed of corner-sharing CuO_4 plaquettes with Cu-O-Cu buckling angle of 146° and 109°, respectively. Many experimental results of CuO have been explained in the hypothesis of a quasi 1D antiferromagnet.

In CuO, Cu has a divalent configuration $3d^9$, one example quantum spin systems. CuO undergoes two successive magnetic transitions at $T_{N1} = $ 213 K and $T_{N1} = $ 230 K [4]. The magnetic structure of CuO below T_{N1} is commensurate with the lattice structure and the magnetic moments are collinearly and ferromagnetically aligned along [101] direction and form up-up-down-down antiferromagnetic ordering along [10$\bar{1}$]. Due to the competition between ferromagnetic and antifettomagnetic interactions CuO, exhibits an incommensurate spiral magnetic structure at the temperature between
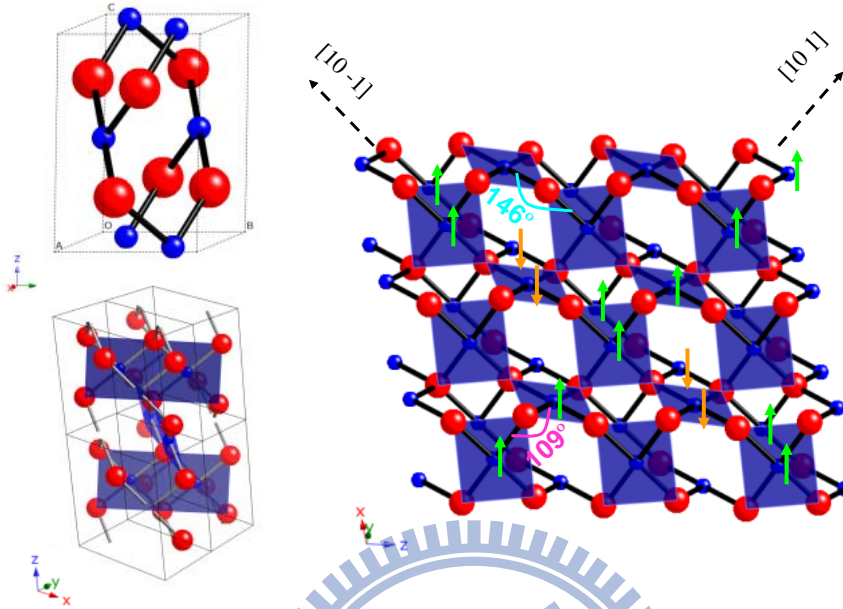
Figure 5.2: The monoclinic unit cell, two types of edge-sharing spin chain, and the magnetic structure of CuO. The blue and red balls are copper and oxygen ions, respectively.

T_{N1} and T_{N2}. Below 213 K, the super-exchange coupling constant J of CuO is 67±20 meV which is significantly large to have a high Nèel temperature. Many experimental data support the hypothesis that a quasi 1D antiferromagnetic Heisenber model is good a approximation for CuO [5, 6, 7, 8].

Because of the contracted in-plane (xy plane) Cu-Oxygen bond lengthes, CuO has $3d$ holes of x^2-y^2 symmetry in the ground state. The local symmetry of CuO can be described in terms of D_{4h} symmetry (tetragonally distorted octahedral), the energy level of $3d$ orbitals of cuprates in O_h and D_{4h} is shown in Fig. 5.3. The dd excitations can considered as the transfer of a $3d$ hole from the x^2-y^2 (b_{1g}) orbital to the z^2 (a_{1g}), zy (b_{2g}), $yz(e_g)$ or $zx(e_g)$ orbitals [9].
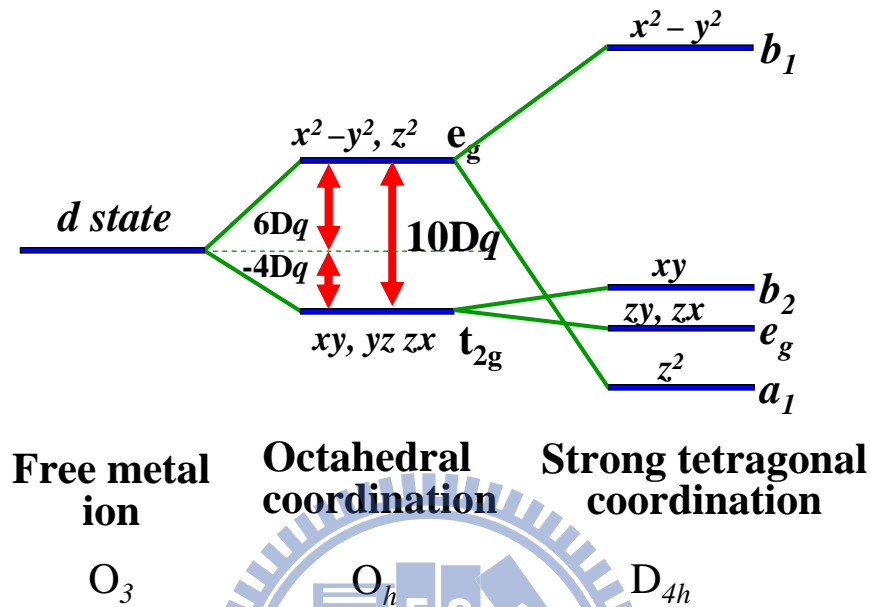
Figure 5.3: The energy level diagram of 3d states with octahedral and strong tetragonal coordinations in different symmetries.

5.2   *dd* excitations

5.2.1   Soft X-Ray Resonant Inelastic Scattering

The single crystal of CuO was grown by the floating zone technique under ~ 8 atm of pure oxygen environment, and characterized with powder X-ray diffraction. The crystal was cut and polished with the surface normal along the [10$\bar{1}$] direction. The incoming photon was linearly polarized with the polarization vector in the horizontal scattering plane. The scattering angle was set 90° to reduce the Thomson scattering. The experimental $L_{2,3}$-RIXS spectra of CuO at room temperature for several selected excitation energies

Figure 5.4: Energy-dependent RIXS spectra measured at the L_3-edge in CuO.

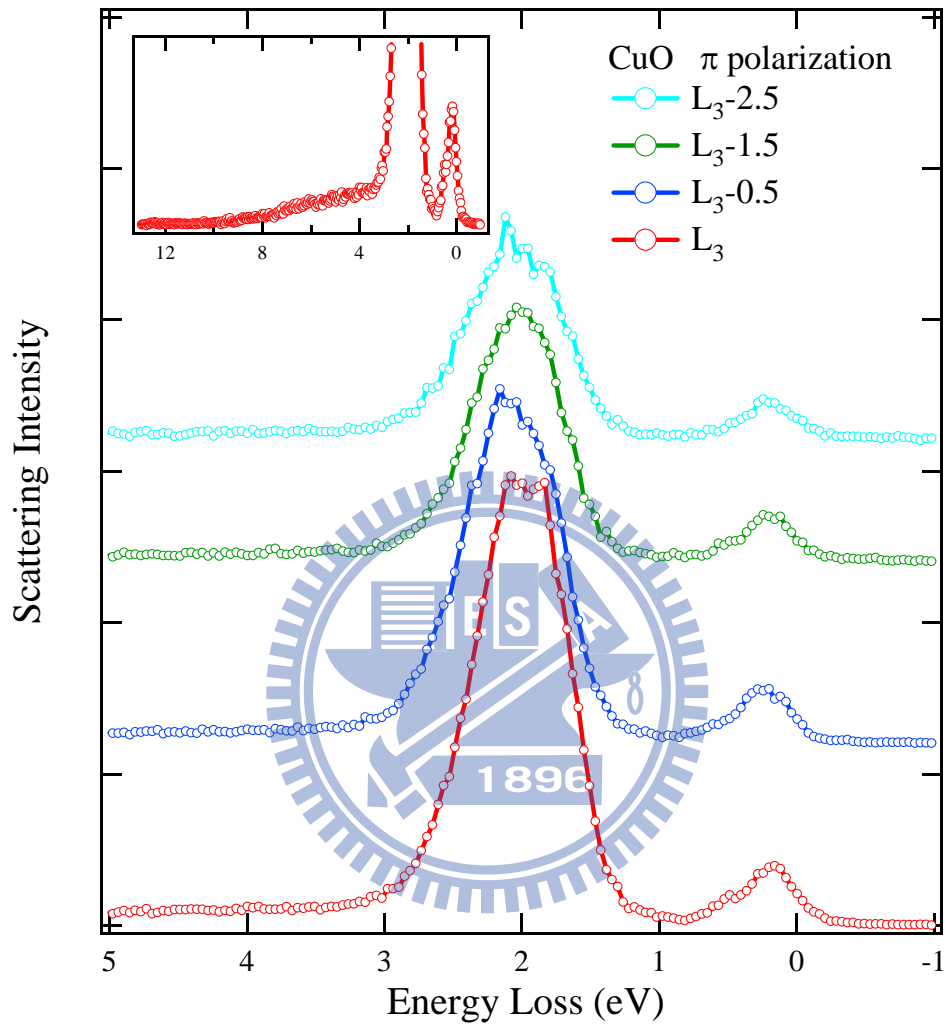are summarized in Fig. 5.4. All spectra were recorded with a photon counting mode. The combined energy resolution is about 240 meV as indicated by the full width at half maximum (FWHM) of the specular elastic peak. In order to increase the spatial resolution, the angle between the CCD surface normal

and the direction of scattered soft X-ray was 60°. We compared our results data of hard X-ray with the inelastic scattering taken at Taiwan beamline ID12 of SPring-8, Japan and the published results by Ghiringhelli et al., [10], and found that a 0.2 eV of energy shift in our CuO spectra. Figure 5.5 shows the comparison our data with energy correction with that from reference [10] recorded powder samples pressed onto an indium support. There is an excitation of 165 meV which is likely of magnetic nature, for example bi-magnons, i.e., collective magnetic excitations in strong mutual interaction. Same phenomena has been proposed by Brink et al., [11, 12, 13, 14] and first observed in the soft x-ray RIXS of undoped cuprate [15]. One can consider this as an nonmagnetic impurity introduced in the intermediate state in which the copper hole is transferred to a neighboring oxygen to form a well-screened intermediate state. This impurity is dynamically screened by the rest of the system, inducing spin reorientations.

The main peaks around 2eV arise from *dd* excitation related to the crystal field splitting. In the scattering process, the initial and final state has a Cu $3d$ hole of spin$-\frac{1}{2}$. In the intermediate sate, the $3d$ shell is completely filled, and the strong core-hole potential alters the superexchange process between the $3d$ valence electrons. When the incident photon energy is tuned to 934.5eV (L_3 edge peak), there are clearly two components. According to the energy diagram of strong tetragonal coordination, the lowest-energy dd transition is from a state with b_1 hole to a state with b_2, i.e., the $x^2 - y^2 \rightarrow xy$ excitation. The second lowest-energy excitation is a transition from b_1 to
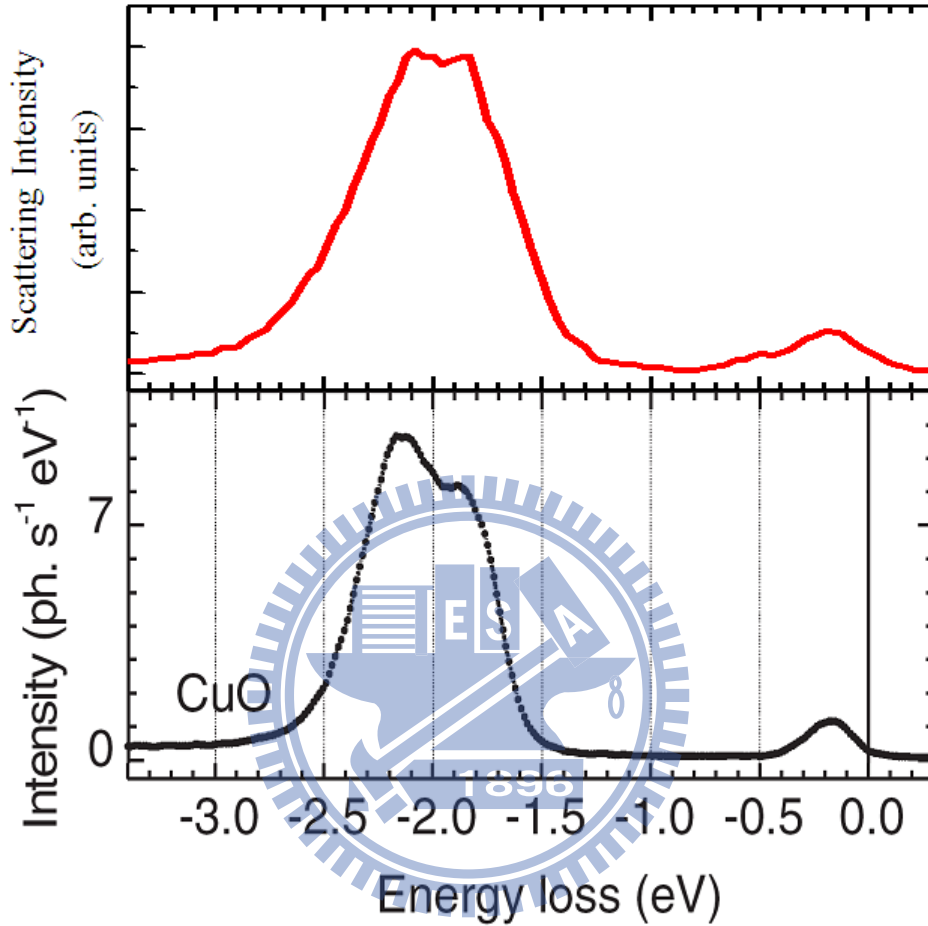
Figure 5.5: The comparison results of CuO. The upper panel is our soft x-ray result with incident energy at L_3-edge absorption peak. The lower panel is taken from ref. [10].

a_1. The in-plane bond length of CuO and $LiCu_2O_2$ are 1.95 and 1,97 Å, respectively. The apical O of $LiCu_2O_2$ is at 2.5 Å above the basal plane, while there is no for apical O in CuO. Thus the tetragonal distortion is much stronger in CuO than that in $LiCu_2O_2$, leading to a more extended energy scale. The tail in the high energy loss part comes from charge transfer excitations.

5.2.2 Non-Resonant Inelastic X-ray Scattering

To double check the *dd* excitation results obtained from soft x-ray RIXS, we measured non-resonant inelastic x-ray scattering. As mentioned in Chapter 2, the double differential cross section for non-resonant inelastic x-ray scattering is given by

$$
\begin{aligned}
\frac{d^2\sigma}{d\Omega d\omega_{q_f}} &= r_o^2 \frac{\omega_{q_f}}{\omega_{q_i}} \sum_{i,f} |(\hat{e}_{qf}^* \cdot \hat{e}_{qi}) \langle \varphi_f | \hat{e}^{-iq\cdot r} | \varphi_i \rangle|^2 \delta(\varepsilon_f - \varepsilon_i - \omega) \\
&= (\frac{d\sigma}{d\Omega})_{Th} S(\mathbf{q}, \omega)
\end{aligned}
$$

The exponential term in the matrix element can be expanded as $\exp^{iq\cdot r}$ $= 1 + i\ q\cdot r + (i\ q\cdot r)^2/2 + ...$. The first term in the expansion does not leads to vanishing cross section if the initial and final states are orthogonal. In the limit of small momentum transfer ($qa \ll 1$, where a is the electron orbital radius), the diploe allowed transitions dominate the excitation spectrum. It is evident that in this approximation the dynamic structure factor is governed by the same transition matrix elements as the cross section for the x-ray absorption process within the single particle approximation

$$
\sigma_{XAS}(\omega_i) \sim |\epsilon_i \cdot \langle \varphi_f | \mathbf{r} | \varphi_i \rangle|^2 \delta(\varepsilon_f - \varepsilon_i - \omega) \tag{5.1}
$$

$$
S(\mathbf{q}, \omega) = |\mathbf{q} \cdot \langle \varphi_\mathbf{f} | \mathbf{r} | \varphi_\mathbf{i} \rangle|^2 \delta(\varepsilon_\mathbf{f} - \varepsilon_\mathbf{i} - \omega)
$$

For high momentum transfers, the higher order terms in the expansion of the exponential are no longer negligible. The increase of the intensity of spectral features originates from monopole or quadrupolar transitions. One

can enhance the probability of higher order transitions by increasing the value of momentum transfer.

We measured non-resonant inelastic x-ray scattering (NIXS) of CuO with the Taiwan Beamline BL12XU at SPring-8 in Japan. With a combination of a Si(111) double-crystal monochromator, a high resolution monochromator Si(400) channel-cut crystal, and three 2-m bent Si(555) spherical analyzer, a total energy resolution of 350 meV was achieved. The analyzers were placed along an axis perpendicular to the horizontal scattering plane. The corresponding momentum resolution were ~ 2.1 mm^{-1} in the horizontal plane and ~ 8.4 mm^{-1} in the vertical plane. The transferred energy was varied by scanning the incident photon energy relative to the near backscattering analyzer. The scattered x-ray were monochromated at 9888.5 eV, collected by an analyzer system, and finally detected by a Si diode. NIXS can study various types of electronic excitations, including valence electron excitations, plasmon and exciton dispersion and other single-particle and collective excitations. Since the incident and scattered photons are high-energy x-ray, thus NIXS is truly a bulk sensitive probe.

The intensity of *dd* excitations as a function of the magnitude q is illustrated Fig. 5.6. All spectra were recorded at room temperature. Each spectrum was measured repeatedly and checked by the elastic peak. According to the expression $|\vec{q}| = \frac{4\pi}{\lambda}\sin(\frac{2\theta}{2})$, where One can measure NIXS of various q by changing the scattering angle or changing the incident photon energy; here we adopt the former method. The intensity as a function of q shows

a maxima around 6 Å^{-1} (Fig. 5.7). As mentioned above, for large wave vectors, the quadrupolar and higher multipole scattering come into play, and strong diploe-forbidden *dd* excitations are measured. The energy loss features
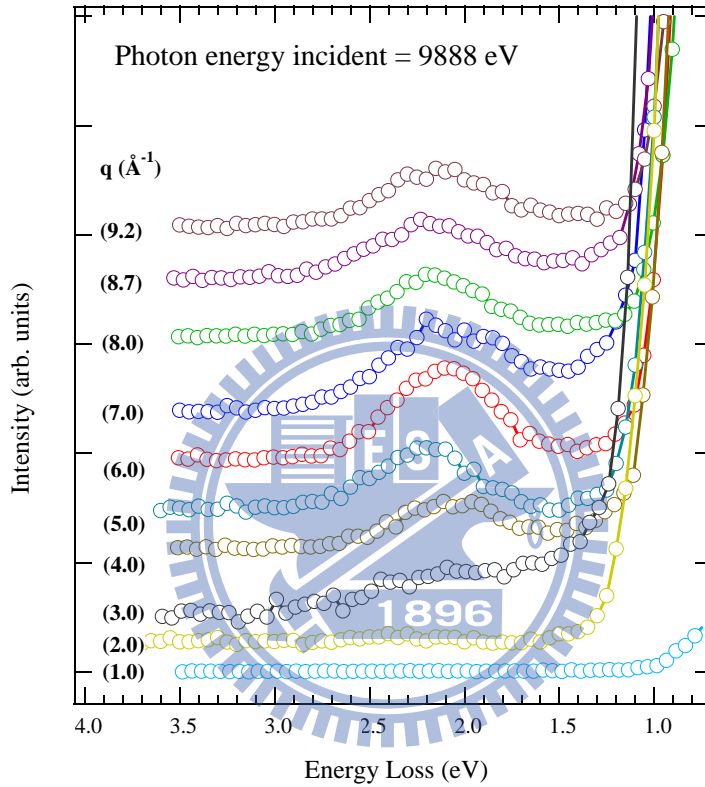

Figure 5.6: The *q* dependence of the *dd* excitation in CuO.

of NIXS agree well measurements of soft X-ray resonant inelastic scattering. In addition, the angular distribution of NIXS from CuO shows a similar trend as those found in the calculations and NIXS measurements of CoO and NiO [16, 17, 18], although CuO has a more distorted local symmetry. The dispersion feature of *dd* excitation as a function of momentum transfer *q* might duo to the competition of two different excitations.
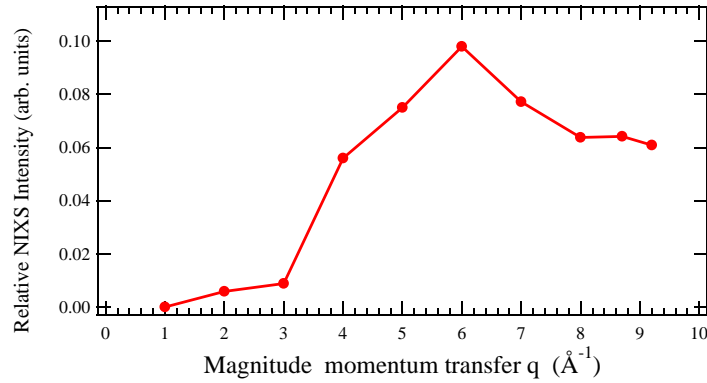
Figure 5.7: The intensity of *dd* excitation peak as a function of the magnitude of momentum transfer **q**.

Figure 5.8(b) and (c) show the comparison of NIXS and soft x-ray RIXS results of CuO. In NIXS measurements, the momentum transfer **q** between incident and scattered x-ray line in the a^*c^* plane, i.e., **q**=(q_a, *0*, q_c). Schismatically the experimental setup is displayed in Fig 5.8 (a). The spectra were collected at *q*= 8.7 Å. By rotating the sample orientation, we obtained the different projected transferred momenta along the high symmetric points. In NIXS measurements, the *dd* excitations were enhanced along different high symmetry points, but those two peaks was simultaneously observed in *L* edge soft x-ray RIXS. The is due to the NIXS is pure charge excitation, with the selection rule ΔS=0, However, for *L* edge RIXS, the transition is ruled by the dipole selection. Spin-orbit coupling, core hole effect, and mixed states of different spins are involved in the results of RIXS spectra at the *L* edge.

In the NIXS, we not only changed the magnitude of *q* to optimize the energy loss feature but also studied the angular dependence spectra. In
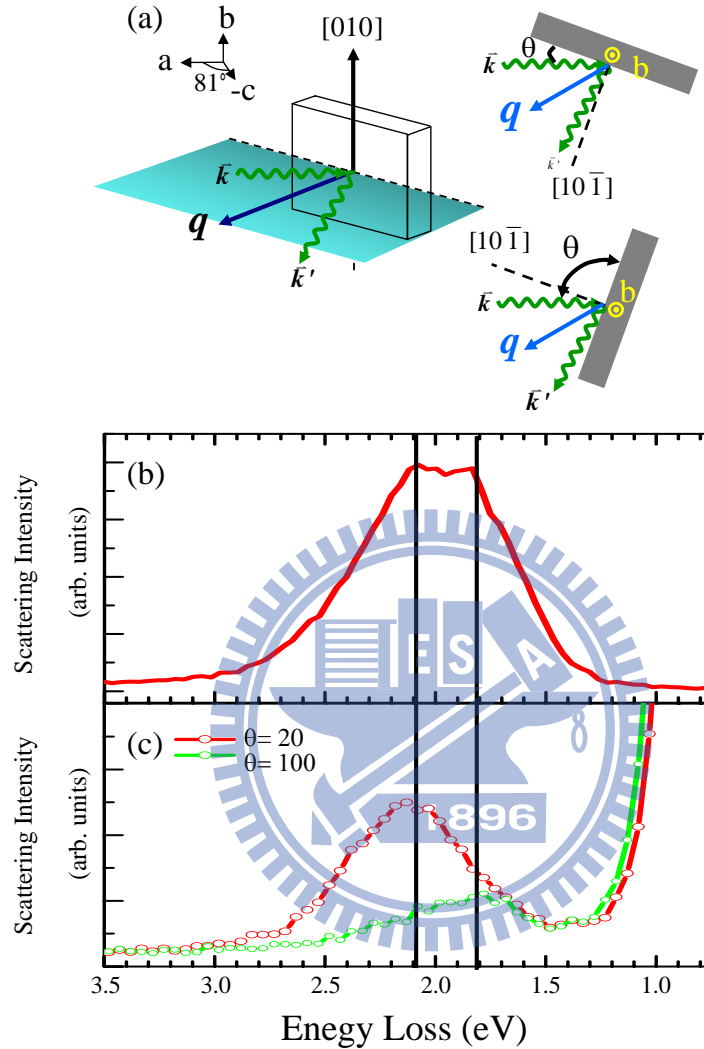
Figure 5.8: (a) The NIXS setup. (b) CuO soft x-ray RIXS result with incident energy at L_3 edge. (c) NIXS results of CuO along different high symmetry directions.

the angular dependence measurements, the transferred momentum q with respect to the crystal orientation gives something equivalent to polarization analysis. A typical angular dependence of NIXS spectra with q fixed at ~ 8.7 Å are presented in Fig. 5.9. The original NIXS data were normalized

by the elastic peak to correct for the self-absorption effect. The components of *dd* excitations could be separated if the momentum transfer selected to different directions. The NIXS results indicate a highly isotropic spectral weight of the atomic-scale excitation.
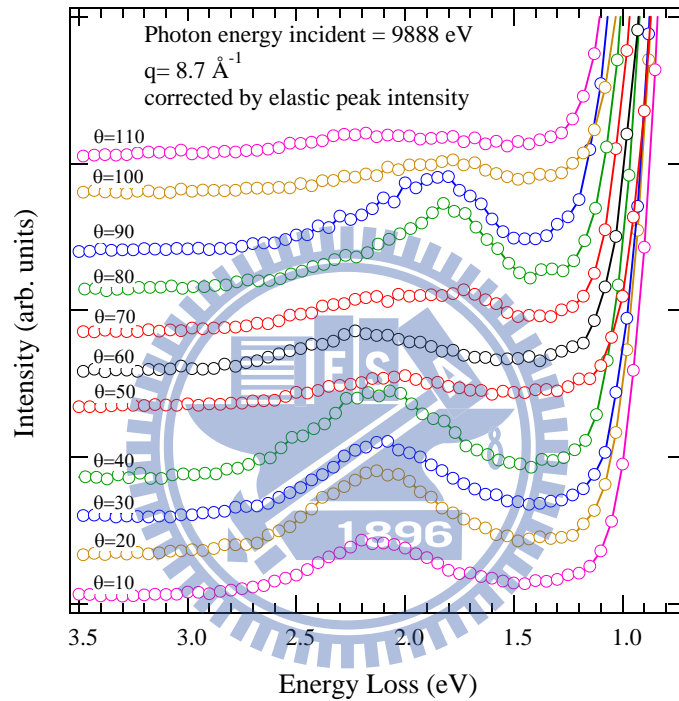
Figure 5.9: Orientation dependence of the *dd* excitations of CuO with $q=$ 8.7 Å^{-1}. θ is the angle between sample surface and the incident beam.

Figure 5.10 shows the polar plots of the *dd* excitations. For $\phi = 60°$, where the momentum transferred is along the $[10\bar{1}]$ direction (Cu-O-Cu 146° bonding direction), the intensity shows a relative minima. As the q direction points toward the a or c axes, the excitations is enhanced. Similar to results observed in NiO and CoO, the intensity of the *dd* excitations show a node

or minima along the bonding direction ([001]) and reach a local maxima as
the direction of the momentum transferred points between the bonding, i.e.,
along the [110] or [111] direction [16, 17].

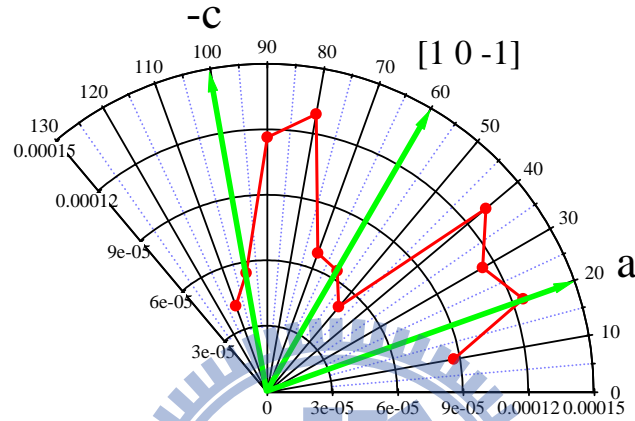Figure 5.10: Polar plot of the intensity of dd excitations.

5.3   Magnetic Transitions

Here we also present measurements of temperature-dependent resonant
soft x-ray magnetic scattering around the L_3 ($2p_{3/2} \longrightarrow 3d$) absorption
edge of Cu to reveal the magnetic transition in CuO single crystals [19].
The scattering measurements were performed in the elliptically polarized
undulator beam line at the NSRRC. The crystals were cut and polished to
set $[10\bar{1}]$ as the surface normal, following by a high-temperature annealing
to remove built-up strain during polishing. The modulation vector q is the
momentum transferred from the materials and lies in the scattering plane
defined by the a and c axis, i,e.,$q = (q_a,\ 0,\ q_c)$. To reduce self-absorption,

the photon energy was set to 923.5 eV, an energy just below the Cu L_3-edge absorption. The linearly polarized x-ray was set in the scattering plane. The scattering results indicate that CuO exhibits an AFM order below 230 K.
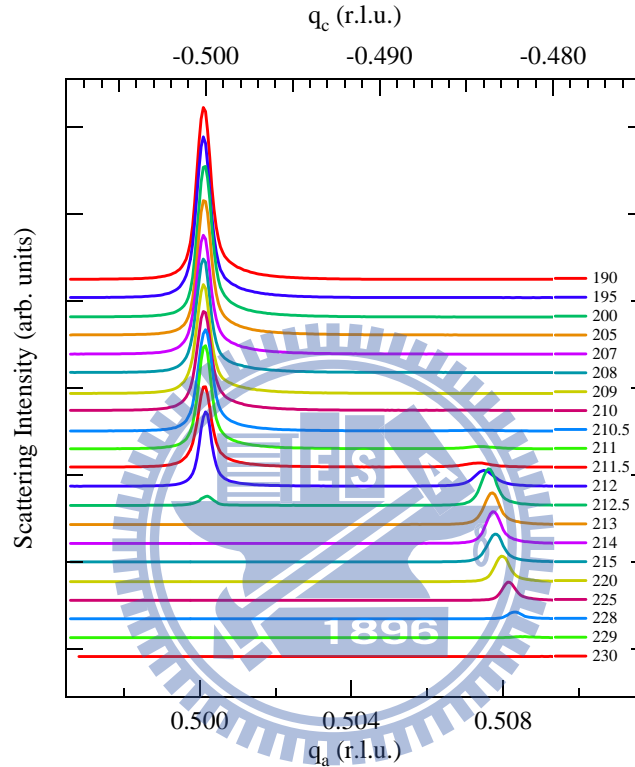
Figure 5.11: Temperature-dependent resonant soft x-ray magnetic scattering of CuO. The polarization of the incident beam is parallel to the scattering plane. Momentum-transfer scans at various temperatures as $q = (H, 0, L)$ sweep in the direction oriented along the modulation vector Q.

The scattering intensities at various temperatures are shown in Fig. 5.11. As the temperature decreases, an AFM order of CuO begins to develop at 230 K, in agreement with neutron results. For the temperatures between 230 and 213 K, the incommensurate scattering intensity increases monotonically; the q_a and q_c of the incommensurate ordering moves toward

0.5 and -0.5 respectively. The intensity of this magnetic peak decreases dra-
matically with further cooling. Below 213 K, another magnetic ordering
with modulation vector along $q=(\frac{1}{2}, 0, -\frac{1}{2})$ developed, indicating that the
magnetic ordering of Cu^{2+} is commensurate with the lattice structure. The
incommensurate-commensurate transition observed at 213 K is consistent
with that of previous neutron results. These results imply that there ex-
ists a temperature-dependent competition of spin coupling between nearest
and next nearest neighbors in the $[10\bar{0}]$. The scattering intensities plotted in
Fig. 5.12 demonstrate the coexistence of commensurate and incommensurate
AFM ordering, similar to the coexistence of commensurate and incommen-
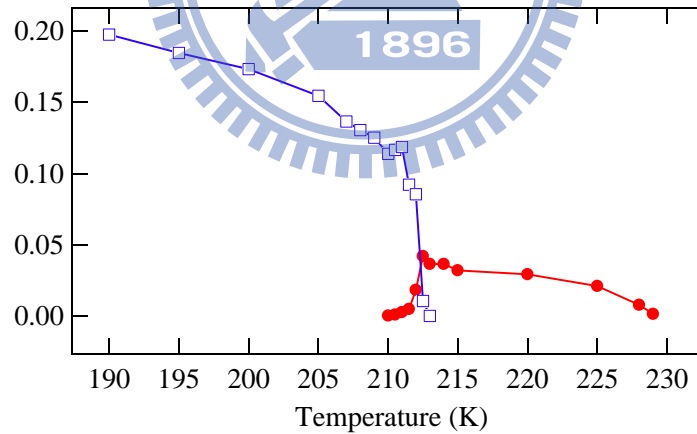surate AFM observed in other multiferroics [20].

Figure 5.12: Scattering intensity v.s. temperature. Blue (red) symbol shows the peak
height of CM (ICM) phase. Solid lines are for eye guide .

Reference

[1] T. Shimizu, T. Matsumoto, A. Goto, K. Yoshimra and K. Kosuge, J. Phys. Soc. Japan **72**, 2165-2168 (2003).

[2] T. Kimura, T. Sekio, H. Nakamura, T. Siegrist, and A. Ramire, Nature Mater, **7**, 291 (2008).

[3] S. Ȧsbrink and L. J. Norrby, Acta Crystallogr. Sect. B **26**, 8 (1970).

[4] B. X. Yang, T. R. Thurston, J. M. Tranquada, and G. Shirane, Phys. Rev. B **39**, 4343 (1989).

[5] J. Ghijsen, L. H. Tjeng, J. van Ele, H. Eskes, J. Westerink, G. A. Sawatzky, and M. T. Czyzyk, Phys. Rev. B. **38**, 11322 (1988).

[6] J. Ghijsen, L. H. Tjeng, H. Eskes, G. A. Sawatzky, and R. L. Johnson, Phys. Rev. B. **42**, 2268 (1990).

[7] L. H. Tjeng, C. T. Chen, and S-W. Cheong, Phys. Rev. B **45**, 8205 (1992).

[8] M. A. van Veenendaal and G. A. Sawatzky, Phys. Rev. B **49**, 3473 (1994).

[9] G. G.hiringhelli, N. B. Brookes, E. Annese, H. Berger, C. Dallera, M. Grioni, L. Perfetti, A. Tagliaferri, and L. Braicovich, Phys. Rev. Lett. **92**, 117406 (2004).

[10] G. Ghiringhelli,A. Piazzalunga, X. Wang, A. Bendounan, H. Berger. F. Bottegoni, N. Christensen, C. Dallera, M. Grioni, J.-C. Grivel, M. Moretti Sala, L. Patthey, J. Schlappa, T. Schmitt, V. Strocov and L. Braicovich, Eur. Phys. J. Special Topics **169**, 199 (2009).

[11] Filomena Forte, Luuk J. P. Ament, and Jeroen van den Brink, Phys Rev. Lett. **101**, 106406 (2008), and references therein.

[12] Filomena Forte, Luuk J. P. Ament, and Jeroen van den Brink, Phys Rev. B **77**, 134428 (2008).

[13] J. van den Brink, Europhy. Lett. **80**, 47003 (2007).

[14] J. van den Brink and M. Veenendaal, J. Phys. Chem. Solids **66**, 2145 (2005).

[15] L. Braicovich, L. J. Ament, V. Bisogno, F. F.orte, C. Aruta, G. Balestrino, N. B. Brookes, G. M. De Luca, P. G. Medagia, F. Miletto Granozio, M. Radovic, M. Salluzzo, J. van den Brink, and G. Ghringhelli, Phys. Rev. Lett. **102**, 167401 (2009).

[16] B. C. Larson, Wei. Ku, J.Z. Tischler, Chi-Cheng Lee, O. D. Restrepo, A. G. Eguiluz, P. Zschack, and K. D. Finkelstein, Phys. Rev. Lett. **99**, 026401 (2007).

[17] M. W. Haverkort, A. Tanaka, L. H. Tjeng, and G. A. Sawatzky, Phys. Rev. Lett. **99**, 257401 (2007).

[18] N. Hiraoka, H. Okamura, H. Ishii, I. Jarrige, K. D. Tsuei and Y. Q. Cai, Eur. Phys. J. B. **70**, 157-162 (2009).

[19] W. B. Wu, D. J. Huang, J. Okamoto, S. W. Huang, Y. Sekio, T. Kimura, and C. T. Chen, Phys. Rev. B **81**, 172409 (2010).

[20] See, e.g., J. Okamoto, D. J. Huang, C.-Y. Mou, K. S. Chao, H.-J. Lin, S. Park, S-W. Cheong, and C. T. Chen, Phys. Rev. Lett. **98**, 157202 (2007), and references therein.
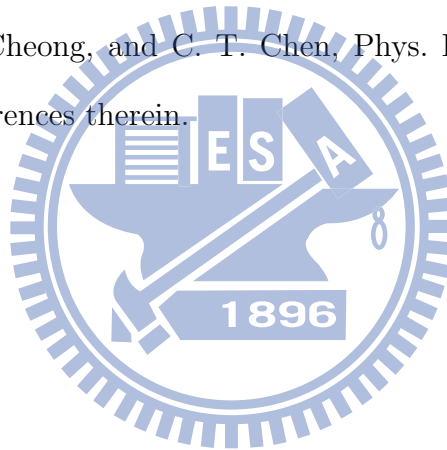
Chapter 6

Conclusion and Future work

The present thesis addresses multiferroic transitions and electronic structure such as low-energy excitation of of quantum magnets. Experimentally, we used advanced synchrotron-based soft X-ray spectroscopic techniques, such as polarization-dependent soft x-ray absorption spectroscopy, resonant soft x-ray magnetic scattering and resonant inelastic soft x-ray scattering, to investigate the magnetic transitions and low energy excitations of low-dimensional quantum spin systems—$LiCu_2O_2$ and CuO.

A newly developed soft x-ray beamline is particularly used to obtain RIXS spectral. For commissioning this new setup, we chose NiO as a test case of high resolution resonant inelastic soft x-ray scattering. The commissioning results showed that the the principle of energy compensation was successfully adopted in the soft x-ray regime and that the newly designed beamline prevails the performance traditional setups.

In XAS measurements, we showed that $3d$ holes exist not only on the Cu^{2+} sites with $3d^9$ electronic configuration but also on the Cu^+ sites which

bridge layers of CuO_4 plaquettes. The nominal Cu^{2+} exhibits predominantly $3d_{xy}$ symmetry in the unoccupied states. We also found that there exist $3d_{3z^2-r^2}$ holes residing on the Cu^+ site and the hybridization between O $2p$ and Cu $3d$ states above the Fermi level. The existence of $3d$ holes on the Cu^+ site might enhance the interlayer magnetic coupling along the c axis These findings indicate that the $3d$ holes of Cu^+ could play a role in the induction of electric polarization.

Based on the resonant soft x-ray magnetic scattering, the results show that $LiCu_2O_2$ exhibits a large inter-chain coupling which suppresses quantum fluctuations along spin chains. A quasi-2D short range magnetic order prevails at temperature above the magnetic transition indicate that the ground state of $LiCu_2O_2$ has semiclassical character and possesses long-range 2D-like incommensurate magnetic order rather than being a gapped spin liquid, although the system has the quantum nature of spin-$\frac{1}{2}$ chain. In addition, the spin coupling along the c axis is found to be essential for inducing electric polarization.

As for the RIXS experiments of CuO, we found that a more careful energy calibration is needed for our spectrometer. Polarization-dependent RIXS measurements provide us information about local dd excitations of $LiCu_2O_2$. The existence of ~ 1.8 eV excitation gives rise to measurement of 1.8 eV crystal field, and a charge transfer energy of 4 - 6 eV were also observed. The comparison of dd excitations from CuO and $LiCu_2O_2$ indicates that the $3d$ crystal field splitting is strongly dependent on the interatomic

distance.

In the NIXS measurements of CuO, two dd excitations were observed. The results of angular dependence show that with q fixed at 8.7 Å, transferred momentum along different directions are involved different with different dd excitations. Recently, calculations based on the first-principles energy resolved with the Wannier function and configuration-interaction clusters can reproduce the q-evolution of the intensities of dd excitations. The angular distribution of NIXS resulting from dd excitations is conceptually explained by a simple minded picture based on bonding direction.

Resonant inelastic soft x-ray scattering performed at the transition metal $3d$ edge is an important tool to study the low energy excitations of novel materials. Recently a series of RIXS measurement to study the local and collective excitations of magnetic or orbital character in transition metal oxide have been reported [1, 2, 3, 4]. A momentum-resolved low-energy excitation measurement with a energy solution down to few hundreds of meV are required in this kind of experiment. How to improve the energy resolution and the collection efficiency are the critical challenges of the second phase of the AGM-AGS beamline.

Reference

[1] L. Braicovich, L.J.P. Ament, V. Bisogni, F. Forte, C. Aruta, G. Balestrino, N. B. Brookes, G. M. De Luca, P. G. Medaglia, F. Miletto Granozio, M. Radovic, M. Salluzzo, J. van den Brink, and G. Ghiringhelli, Phys. Rev. Lett. **102**, 167401 (2009).

[2] G. Ghiringhelli, A. Piazzalunga, C. Dallera, T. Schmitt, V. Strocov J. Schlappa, L. Patthey, X. Wang, H. Berger, and M. Grioni, Phys. Rev. Lett. **102**, 027401 (2009).

[3] C. Ulrich, L.J.P.Ament, G. Ghiringhelli, L. Braicovich, M. Moretti Sala, N.Pezzotta, T.Schmitt, G. Khaliullin, J. van den Brink, H. Roth, T. Lorenz and B.Keimer, Phys. Rev. Lett. **103**, 107205 (2009).

[4] J. Schlappa, T. Schmitt, F.Vernay, V. N. Strocov, V. Ilakovac, B. Thielemann, H. M. RØnnow, S. Vanishri, A. Piazzalunga, X. Wang, L. Braicovich, G. Ghiringhelli, C. Marin, J.Mesot, B. Delley, and L. Pattey, Phys. Rev. Lett. **103**, 047401 (2009).

[5] Luunk J. P. Ament, Giacomo, Ghiringhelli, Macro Moretti Sala, Lucio Braicovich and Jeroen van den Brink, Phys. Rev Lett. **103**, 117003

(2009).

[6] L. Braicovich, J. van den Brink, V. Bisogni, M. Moretti. Sala, L. J. P. Ament, N. B. Brookes, G. M. De Luca, M.Salluzzo, T. Schmitt, V. N. Strocov, and G. Ghiringhelli, Phys. Rev. Lett. **104**, 077002 (2010).

[7] Luuk J. P. Ament, Michel van Veenendaal, Thomas P. Devereaux, John P. Hill, and Jeroen van den Brink. (unpublished).